DCT 227

Testing and Analysis of the Route 141 Newport Viaduct: Fatigue Evaluation

By

HARRY W. SHENTON, III
MICHAEL CHAJES
DANIEL KUCZ
JAMES QUIGLEY
JOSE SOTO FUENTES

Center for Innovation Bridge Engineering
University of Delaware

June 2012

Delaware Center for Transportation
University of Delaware
355 DuPont Hall
Newark, Delaware 19716
(302) 831-1446

The Delaware Center for Transportation is a university-wide multi-disciplinary research unit reporting to the Chair of the Department of Civil and Environmental Engineering, and is co-sponsored by the University of Delaware and the Delaware Department of Transportation.

DCT Staff

Ardeshir Faghri
Director

Jerome Lewis
Associate Director

Ellen Pletz
Assistant to the Director

Earl "Rusty" Lee
T^2 Program Coordinator

Matheu Carter
T^2 Engineer

Sandra Wolfe
Event Coordinator

DCT Policy Council

Natalie Barnhart, Co-Chair
Chief Engineer, Delaware Department of Transportation

Babatunde Ogunnaike, Co-Chair
Dean, College of Engineering

Delaware General Assembly Member
Chair, Senate Highways & Transportation Committee

Delaware General Assembly Member
Chair, House of Representatives Transportation/Land Use & Infrastructure Committee

Ajay Prasad
Professor, Department of Mechanical Engineering

Harry Shenton
Chair, Civil and Environmental Engineering

Michael Strange
Director of Planning, Delaware Department of Transportation

Ralph Reeb
Planning Division, Delaware Department of Transportation

Stephen Kingsberry
Executive Director, Delaware Transit Corporation

Shannon Marchman
Representative of the Director of the Delaware Development Office

James Johnson
Executive Director, Delaware River & Bay Authority

Holly Rybinski
Project Manager-Transportation, AECOM

Delaware Center for Transportation
University of Delaware
Newark, DE 19716
(302) 831-1446

Testing and Analysis of the Route 141 Newport Viaduct: Fatigue Evaluation

Harry W. Shenton III, Michael J. Chajes, Daniel Kucz, James Quigley, Jose Soto Fuentes

June 2012

Table of Contents

List of Tables

List of Figures

1 Introduction

1.1 Background

Distortion induced fatigue cracking is a problem found in certain older steel bridges in the United States. It is typically attributed to deformations that take place in some direction other than the primary load direction of the member, and is often related to the connection of secondary members to primary members. It is something that was not accounted for or anticipated in the original design, but often requires remedial action once the cracking is discovered.

Bridge number 1-501, also known as the Newport Viaduct, is a 19-span steel trapezoidal box girder bridge that carries State Route 141 over State Route 4, in Newport, Delaware. It was constructed in 1978. During a 2006 inspection of the inside of the box girders (the first internal inspection ever conducted on the viaduct), cracks were discovered in the web gap region where the diaphragm connection plate is welded to the girder web. More than 600 individual cracks or crack locations were identified; cracks were found in all 19 spans. The cracks were generally hairline in nature with lengths ranging from 1/8 in. to 4 in., and were present on both sides of the connection plates (north and south) and girder webs (east and west). Visual inspection indicated that 37 of the cracks had propagated into the base metal of the girder web. As a result the bridge was classified as structurally deficient and placed on the Delaware Department of Transportation (DelDOT) list of priority bridges (DelDOT, 2007).

AECOM, a national engineering and consulting firm, was hired to develop a repair and retrofit plan for the viaduct. The University of Delaware Center for Innovative Bridge Engineering was contracted to provide support to AECOM and DelDOT in the investigation of the cause of the cracks and development of the repair plans. This report summarizes the work and the findings of the University of Delaware Center for Innovative Bridge Engineering.

1.2 Description of the viaduct

A map with the location of the bridge is shown in Figure 1.1. The main structure has 19 spans which consist of multiple welded steel tub girders with a composite concrete deck. Of the 19 spans, 15 are continuously supported and 4 are simply supported. The spans are numbered 1 through 19 starting from the south. In addition to the main structure, there are ramps on the east and west sides of the bridge linking Route 141 to local roads.

Figure 1.1 Arial view of viaduct

Traffic travels in both northbound and southbound directions, each with its own structure. There is an open joint between the northbound and southbound structures, resulting in the two independent structures. Each structure carries two 12 ft. wide travel lanes and a 12 ft. wide right side shoulder. A narrow (2ft.) left shoulder makes up the remainder of the roadway surface. Each span has between 2 and 4 girders and a concrete composite deck. The depth of the girders is uniform at 4 ft. but the bottom flange widths vary from span to span. Span configurations are listed in Table 1.1.

Table 1.1 Newport Viaduct Span Configuration

Span #	Span Configuration	Span Length	# Girders and width
1	Four-span continuous	90'-0"	3-box (4' deep, 6'-6" wide bottom flange)
2		110'-0"	
3		130'-0"	
4		109'-1"	
5	Three-span continuous	99'-1"	3-box (4' deep, bottom flange varies from 6'-6" to 8'-6" wide)
6		100'-0"	
7		99'-1"	
8	Simple	101'-9"	4-box (4' deep, 4 girders w/ 9'-0" bott flange, 4 girders w/ 5'-0" bott flange)
9	Three-span continuous	97'-1"	2-box (4' deep, bottom flange varies from 9'-6" to 8'-0" wide)
10		100'-0"	
11		99'-1"	
12	Five-span continuous	118'-0"	2-box (4' deep, 8'-0" wide bottom flange)
13		118'-0"	
14		118'-0"	

15		118'-0"	
16		118'-0"	
17	Simple	83'-10 5/8" (tangent from pier 16)	2-box (4' deep, 8'-0" ± 1/16" wide bottom flange)
18	Simple	84'-2 15/16" (tangent from pier 16)	2-box (4' deep, 8'-0" ± 1/8" wide bottom flange)
19	Simple	84'-7 1/2" (tangent from pier 16)	2-box (4' deep, 8'-0" ± 1/8" wide bottom flange)

A typical cross section of a girder is shown in Figure 1.2. The steel girders are welded plates forming a trapezoidal cross section. The girder webs are angled at a 4:1 slope and have a depth of 4 ft., as such, the distance between the top flanges of the girders vary with the bottom flange width. The thickness of the web and flanges varies with span and location.

The nominal thickness of the concrete deck is 9 in., but this varies with location. Between girders, a constant thickness of 9 in. is specified. Otherwise the depth varies between a low of 6 in. on the outside edge, to a maximum of almost 16 in. over some of the haunches. To achieve composite action with the deck, shear studs are welded to the top flanges of the box girders. They are specified to be 0.875 in. diameter shear studs with a 1.375 in. diameter head configured in rows of three. The length of the shear studs varies depending on the flange location, but they are specified to extend a minimum of 2 in. beyond the bottom layer of deck re-bar not surpassing the top layer.

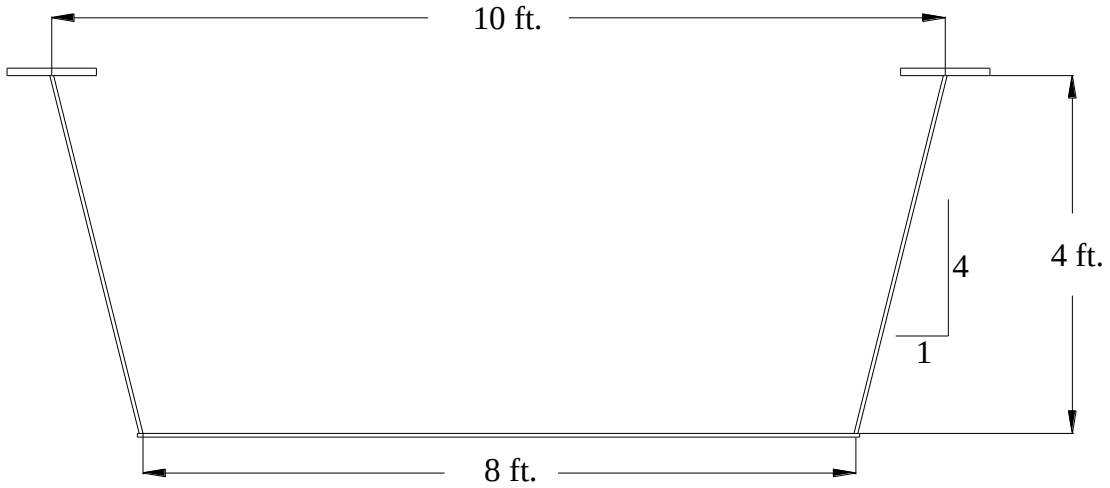

Figure 1.2 Typical girder cross-section (girder depth is 4 ft for all spans, bottom flange widths vary)

Internal diaphragms are spaced longitudinally throughout the girders to provide stability and to increase the torsional stiffness of the structure. Two types of internal diaphragms are used for this purpose, “Type E” and “Type F”. The Type F diaphragm is a steel 7 in. x 4 in. x 3/8 in. angle bolted to connection plates just below the top flanges on both sides of the girder. Layout and dimensions of the Type F

diaphragm are shown in Figure 1.3. The connection plates are 3/8" thick and are welded to the girder web a minimum of 2 ½ in. below the bottom of the top flange to just beyond the depth of the angle. The Type E diaphragm is a Type F diaphragm with the addition of two 3 in. x 3 in. x 3/8 in. steel angles oriented diagonally to form an x-type brace, and longer connection plates. The angles are connected at their ends to the respective plates and angles, but are not connected to each other where they cross. The connection plates for the Type E diaphragms are also 3/8 in. thick steel plates that are welded to the webs. The Type E connection plates extend from below the top flange to above the bottom flange. Details specify that a minimum distance of 2 1/2 in. must be maintained between the top or bottom of the connection plate and the nearby flange. The cross frame angles are bolted to the bottoms of the connection plates and to the 7 in. x 4 in. x 3/8 in. horizontal angle with two bolts at each connection. Layout and dimensions of the Type E diaphragm are shown in Figure 1.4. A photograph of the Type E diaphragm is shown in Figure 1.5. A typical girder has the Type E and Type F diaphragms alternated, spaced at approximately 24 ft throughout the span.

Increased stiffness is provided at the negative moment regions of the continuous spans. This comes from additional steel members added to the interior of the girder. On top of the bottom flange, five 5 x 10.5 structural tees are welded at even intervals between the girder webs. These run longitudinally in the negative moment region from 3 in. inside of one splice plate to 3 in. inside the next splice plate. Above and perpendicular to the WT's, C 20.7 structural channels are welded to each side of the girder web. The bottom flanges of the channels rest on the top flange of the WT's and they are welded where there is contact. These are spaced at approximately 6 ft.-6 in. typically resulting in 4 lateral channels on either side of each pier.

The steel properties in the trapezoidal boxes vary by location along the length of the spans and by component. A572 Grade 50 steel (fy = 50ksi) is specified in many of the negative moment regions, and A36 steel (fy = 36 ksi) is specified in the positive moment regions. The concrete deck superstructure was specified to have a 28-day compressive strength of 4,500 psi (f'c = 4.5 ksi).

1.3 Fatigue cracking

Construction of the viaduct was completed in 1978. The first ever interior inspection of the girders was conducted in the fall of 2006. The conclusion of the 2006 Interior Box Inspection Report (DMJM Harris, 2006) was an overall good condition of the structure existed with the exception of cracked welds between the Type E diaphragm connection plates and the box girder webs. In total, 655 cracks were found; the cracks were hairline in width with lengths varying from 1/8 in. to 4 in. and occurred only at Type E diaphragm locations. As a result of the extensive and widespread cracking, recommendations were made to monitor the current cracked locations with particular attention to cracks that appear to have propagated into the girder webs.

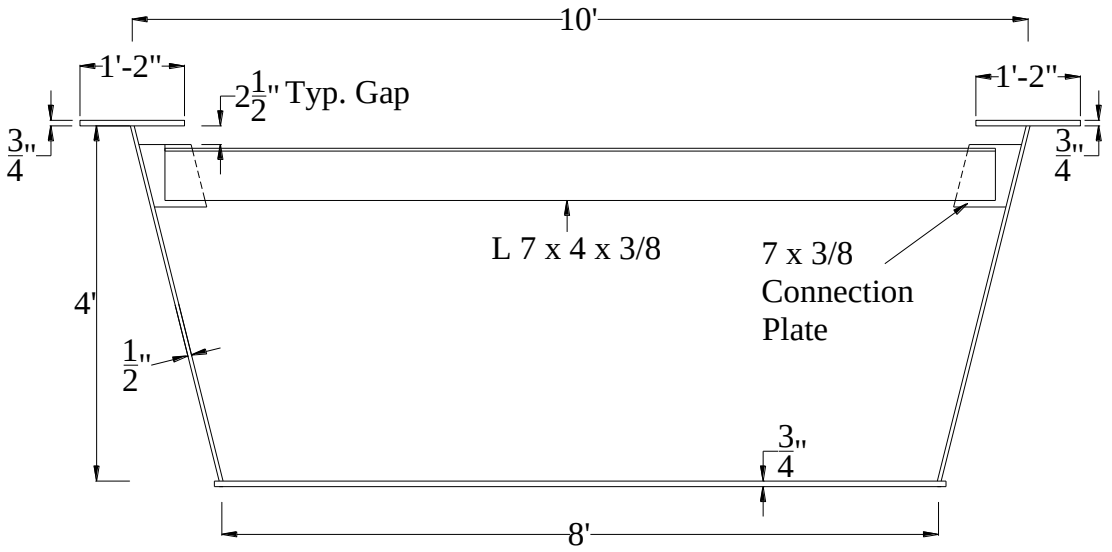

Figure 1.3 Type F diaphragm

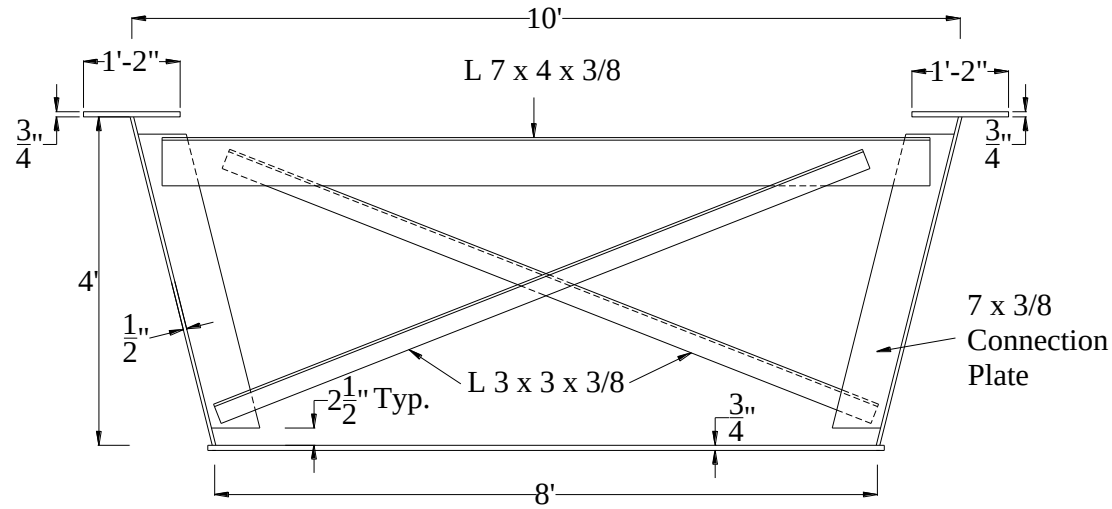

Figure 1.4 Type E diaphragm

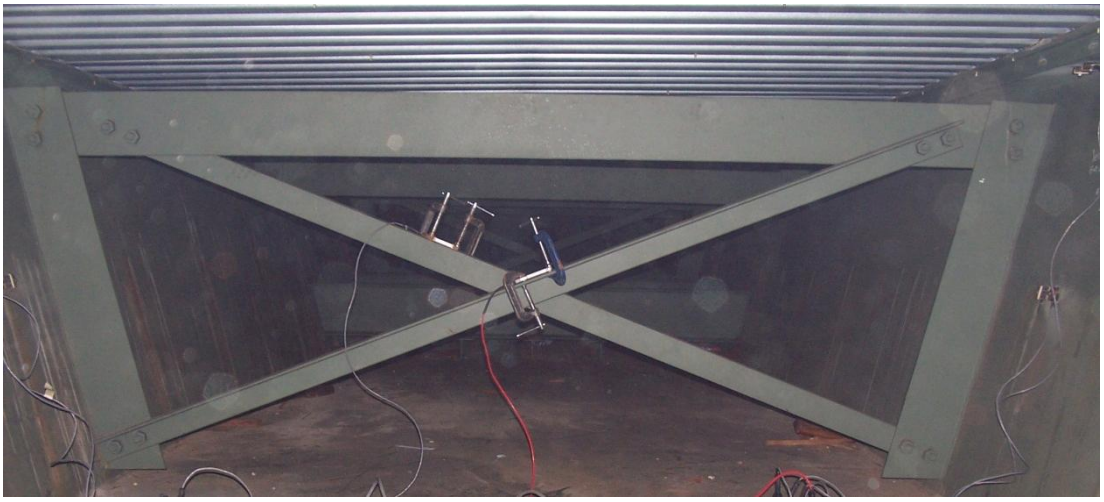

Figure 1.5 Photograph of a Type E diaphragm

Since the 2006 Interior Box Inspection Report, 52 crack locations were identified as requiring retrofit. Of these, 10 locations were selected as candidates for core sampling in which more extensive metallurgical examination would be carried out (DMJM Harris, 2006).

Fatigue cracking in the structure is present at the weld between the Type E diaphragm connection plates and the girder webs. The connection plates are fillet welded to the girder webs along their entire length, with the weld extending underneath the connection plate end termination. Cracking is present at both the top and bottom of the connection plate termination and on both sides of the connection plate (north and south). Typically, the cracks follow the edge of the fillet weld on the underside of the stiffener and extend vertically along the interface of the connection plate fillet weld. Along the underside of the connection plate, the fatigue cracks are generally located at the connection plate end near the weld root. As they propagate, the cracks cross through the weld material to the weld toe interface. In some cases, the cracks have propagated outward from the interface of the connection plate fillet weld and extend into the girder web material (Figure 1.6, Figure 1.7).

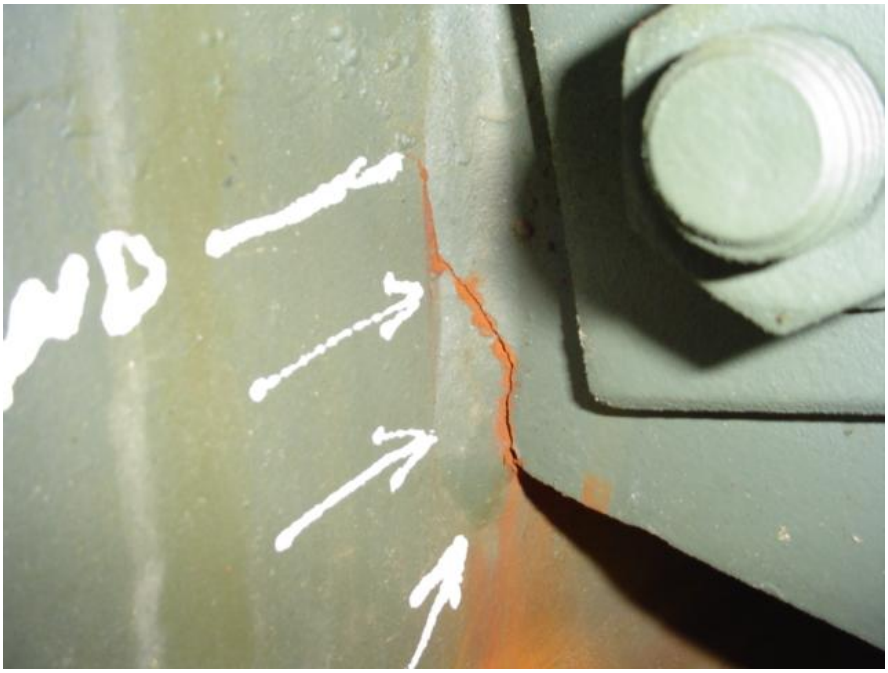

Figure 1.6 Typical crack at weld toe of connection plate (DMJM Harris, 2006)

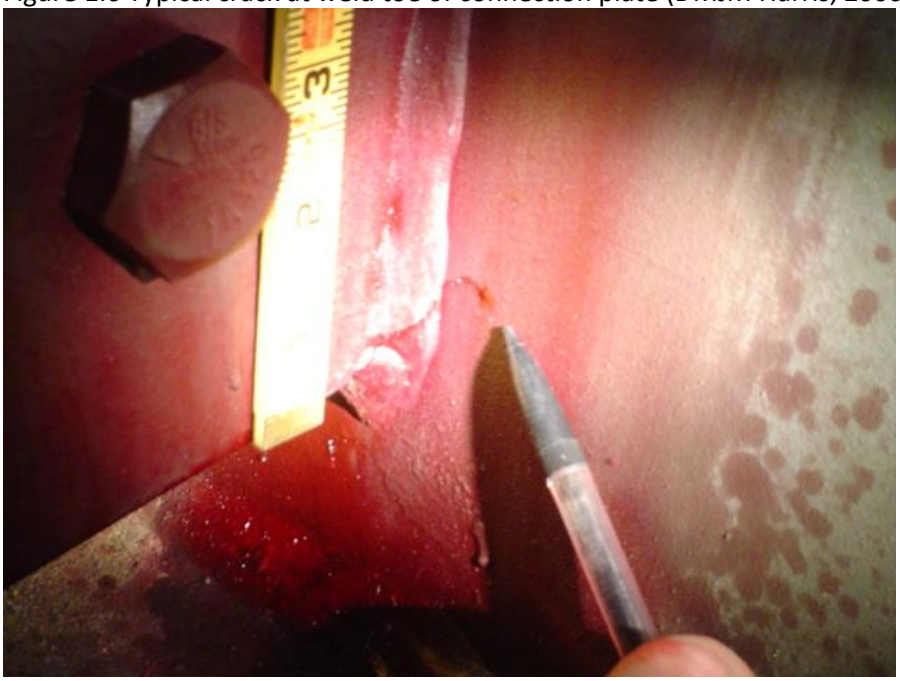

Figure 1.7 Typical crack showing propagation into base material of the girder web (DMJM Harris, 2006)

Six cracks were removed from the Newport Viaduct as core samples, and were taken to Lehigh University for examination. The cracks were determined to be a result of fatigue initiation. The cracks initiated in the weld metal and propagated towards the web through the weld. Evidence of repeated crack initiation suggests that the crack propagation was due to out-of-plane web distortions. There was no visual evidence of weld defects, signifying that the crack initiated at normal defects within the weld toes. As is expected with this type of fatigue stress, the cracks started in the longitudinal direction and

either turned to run transverse along the web, or were expected to do so if propagation had continued (Kaufmann, 2008).

1.4 Objectives of the project

The objectives of the project were to conduct field tests of sections of the viaduct and develop detailed finite element models that would be used to conduct a fatigue evaluation of the viaduct, and to assist in developing a repair and retrofit strategy for the viaduct. The specific objectives were:

1. Conduct diagnostic load tests of sections of the viaduct to measure the strains induced by loads of known weight. The data from the tests would be used to calibrate finite element models of the viaduct.
2. Conduct in-service monitoring due to the site specific traffic of one or more crack prone details to estimate the true effective stress range at the detail.
3. Develop global finite element models of two different sections of the bridge; calibrate the models using the results of the controlled load tests.
4. Develop a detailed 3D finite element model of the connection and analyze it for various load condition.
5. Use the global and local finite element models to estimate effective stress in the crack location and conduct a fatigue evaluation and remaining life study of the fatigue prone details.
6. Use the global finite element model to study various retrofit options and provide recommendations on the effectiveness of each.

1.5 Project timeline

Work on the project began in the fall of 2007 and continued through the spring of 2011. The actual work by the consultant began sometime after UD commenced working on the project, and AECOM completed their tasks before the UD work was completed. However, the results of the UD study were used by the consultant in developing their final retrofit plans.

The results are documented in three separate Master's thesis' from the University of Delaware, these are:

> "Analysis of distortion-induced fatigue cracking of a trapezoidal steel box girder bridge including retrofit investigation," by James R. Quigley, Spring 2009
>
> "Analysis of distortion-induced fatigue cracking in a steel trapezoidal box girder bridge," by Daniel A. Kucz, Spring 2009
>
> "Fatigue life analysis of a steel trapezoidal box girder bridge using measured strains," by Jose Soto Fuentes, Spring 2011

All of the details of the work reported herein is included in the above mentioned thesis'.

The remainder of the report is organized as follows:

- Chapter 2 – describes the field tests that were conducted. This includes the diagnostics tests of spans 10 and 15, and the in-service monitoring that was conducted on span 10.
- Chapter 3 – describes the global finite element models that were developed of spans 10 and 15, and the local finite element models of the connections.
- Chapter 4 – the fatigue evaluation is reported in this chapter.
- Chapter 5 – retrofit options are presented and the results of the retrofitted finite element models are described.
- Chapter 6 – conclusions and recommendations

2 Field Testing

2.1 Introduction

Two controlled load tests were conducted on the viaduct for the purpose of gathering data to calibrate the finite element models of the bridge. Span 10 was tested on December 17, 2008, and Span 15 was tested on December 18, 2008. In-service monitoring was also conducted on Span 10 for the purpose of measuring the actual effective stress near the connection due to the site specific traffic. The in-service monitoring commenced on November 17, 2010 and continued around the clock, for 23 days. Presented below is a summary of these tests and the results.

2.2 Controlled Load Tests of Spans 10 and 15

Test Setup – Span 10

The Bridge Diagnostics Inc. (BDI), Structural Testing System (STS) was used to conduct the controlled load tests. The system consists of strain transducers, 4-channel data acquisition junction boxes, and a main power supply/control system. The BDI strain transducers have a gage length of three inches, and are either clamped to a member using C-clamps, or when that is not possible, bonded to the surface using a quick setting 2-part adhesive. Once the sensors are mounted they are connected to the junction boxes, which in turn are daisy-chained with trunk cables back to the main power supply/control system. The STS is operated from a laptop computer that is connected to the control system.

A total of 23 strain transducers were mounted near three Type E cross frames in span 10. The overall layout of the test is shown in Figure 2.1. On the interior (east) girder, transducers were placed near the Type E diaphragms in the positive moment region, numbered XF2 and XF3 from the south (Section A and Section B, respectively). On the exterior (west) girder, transducers were places near XF2 only (Section C). The sensors were deployed in this fashion to capture the overall structural behavior longitudinally and transversely of the viaduct.

Strains due to bending were measured by installing transducers on the bottom flange, mid-height, and top flange of the girder on both webs (east and west) at each section (A,B,C). To avoid local out-of-plane effects induced by the Type E diaphragms, the sensors were offset a distance of 1 ft. to the north of the cross frame. Axial strains in the Type E diaphragm cross frame members were measured by clamping the transducers directly to one leg of the members (note that the sensors were placed on the outstanding leg of the angle, i.e., the one that was not bolted to the connection plate). For the gages installed on the box girder with adhesive, the surface was prepared by grinding through the protective paint layer to the structural steel. The sensor designations (numbers) and their locations are listed in Table 2.1. A typical cross section showing the layout of the strain sensors is shown in Figure 2.2. Figure 2.3 shows general views of the transducers after installation.

Test Setup Span 15

The span 15 setup was very similar to the span 10 setup. A total of 23 strain gages were mounted near three Type E cross frame locations in span 15. The overall layout of the test is shown in Figure 2.4. The sensor numbers and their locations are listed in Table 2.5

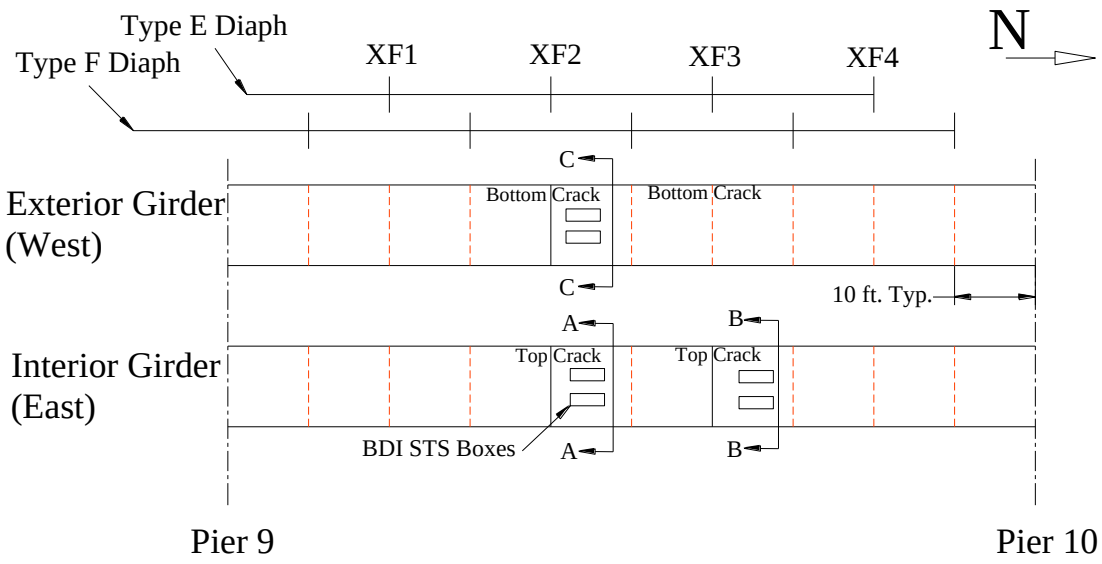

Figure 2.1 Global layout of instrumentation locations in Span 10 (southbound) at Sections A, B, and C

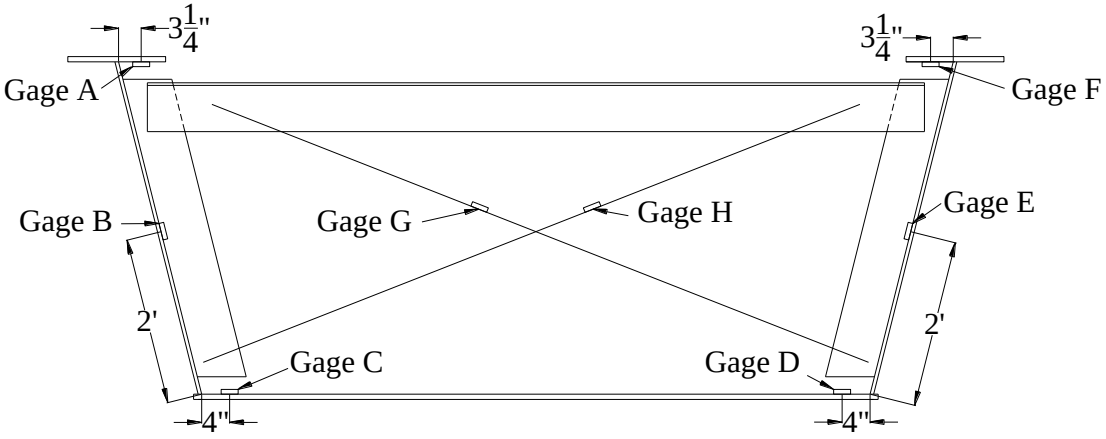

Figure 2.2 Typical cross section sketch of gage locations, Spans 10 and 15 (gages A through F are located 1 ft north of the cross frame).

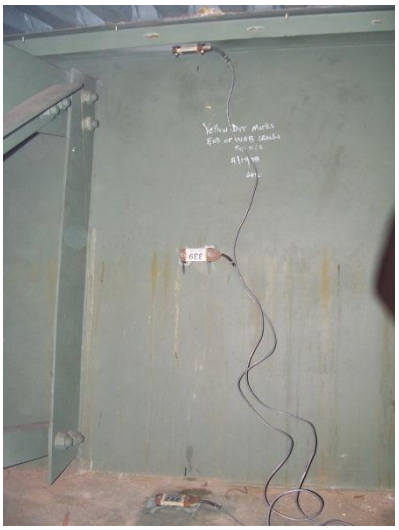

Transducers mounted to flanges and web

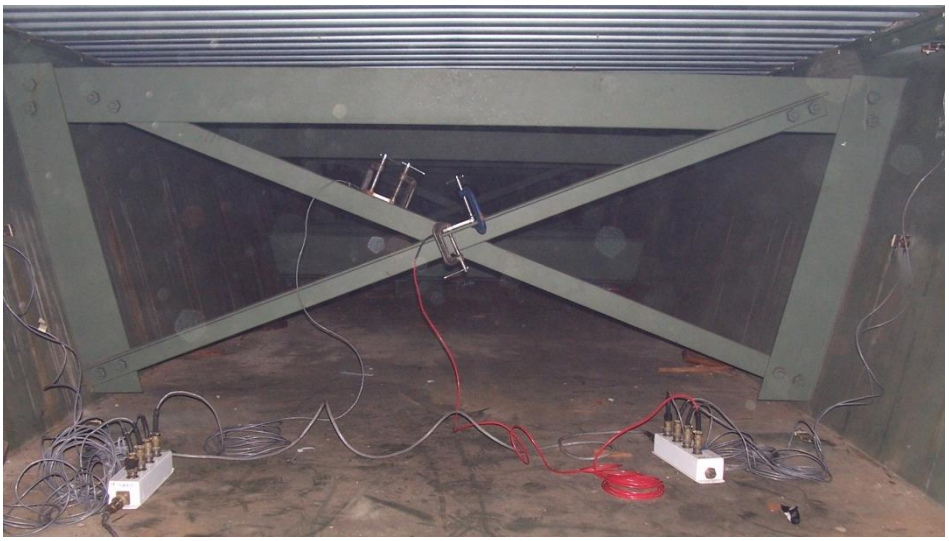

Transducers mounted to cross frames

Figure 2.3 General view of Strain Transducers after Installation

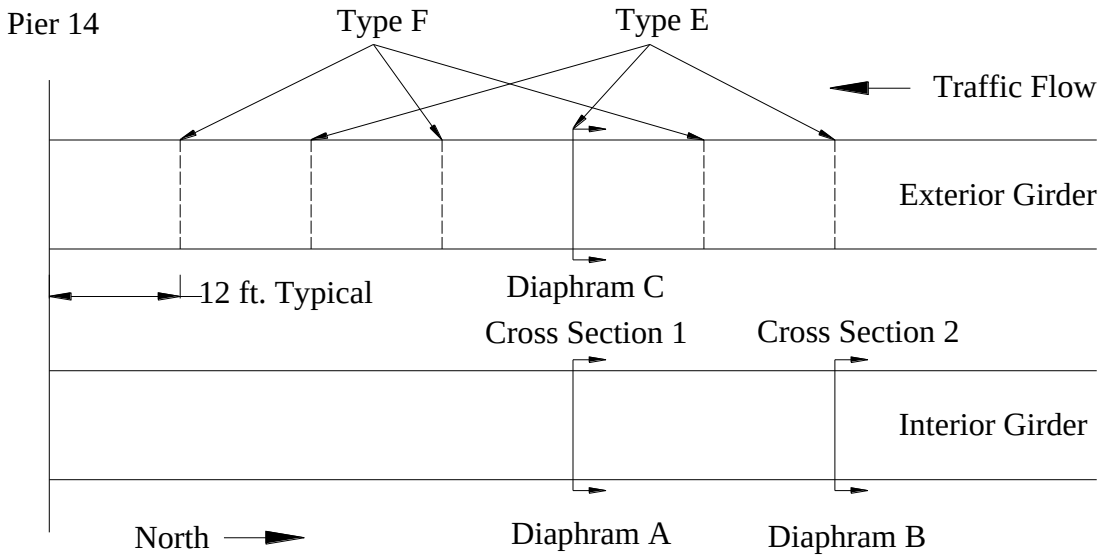

Figure 2.4 Global layout of instrumentation locations in Span 15 (southbound) at Sections A, B, and C

Table 2.1 Sensor locations for test – Span 10

Location (Looking South)	Sensor		
	Diaphragm A	Diaphragm B	Diaphragm C
A: Top Flange Left	302	344	298
B: Left Web	535	314	293
C: Bottom Flange Left	356	355	303
D: Bottom Flange Right	292	295	317
E: Right Web	339	337	346
F: Top Flange Right	299	306	348
G: Cross frame 1	338	-	294
H: Cross frame 2	1477	1475	318

Table 2.2 Sensor locations for test – Span 15

Location (Looking South)	Sensor		
	Diaphragm A	Diaphragm B	Diaphragm C
A: Top Flange Left	295	302	344
B: Left Web	317	348	298
C: Bottom Flange Left	293	337	356
D: Bottom Flange Right	314	292	355
E: Right Web	338	306	339
F: Top Flange Right	299	535	303
G: Cross frame 1	-	1475	346

H: Cross frame 2	318	1477	294

Test Vehicles and Passes

DelDOT provided two 3-axle, 10-wheel fully loaded dump trucks for the live loads for the tests. The truck loads were field measured using InterComp PT300 portable wheel scales which have an accuracy of +/- 10 lbs. The gross vehicle weights were 53.49 kips and 52.97 kips for trucks #314 and #2886, respectively. For Truck #314, the centerline distance from the front axle to the middle axle was 15 ft. 5 in. For Truck #2886, this distance was 13 ft. 11 in. For both trucks, the distance from the middle axle to the rear axle was 4 ft. 6 in. A detailed drawing of the truck wheel weights and axle spacings is shown in Figure 2.5.

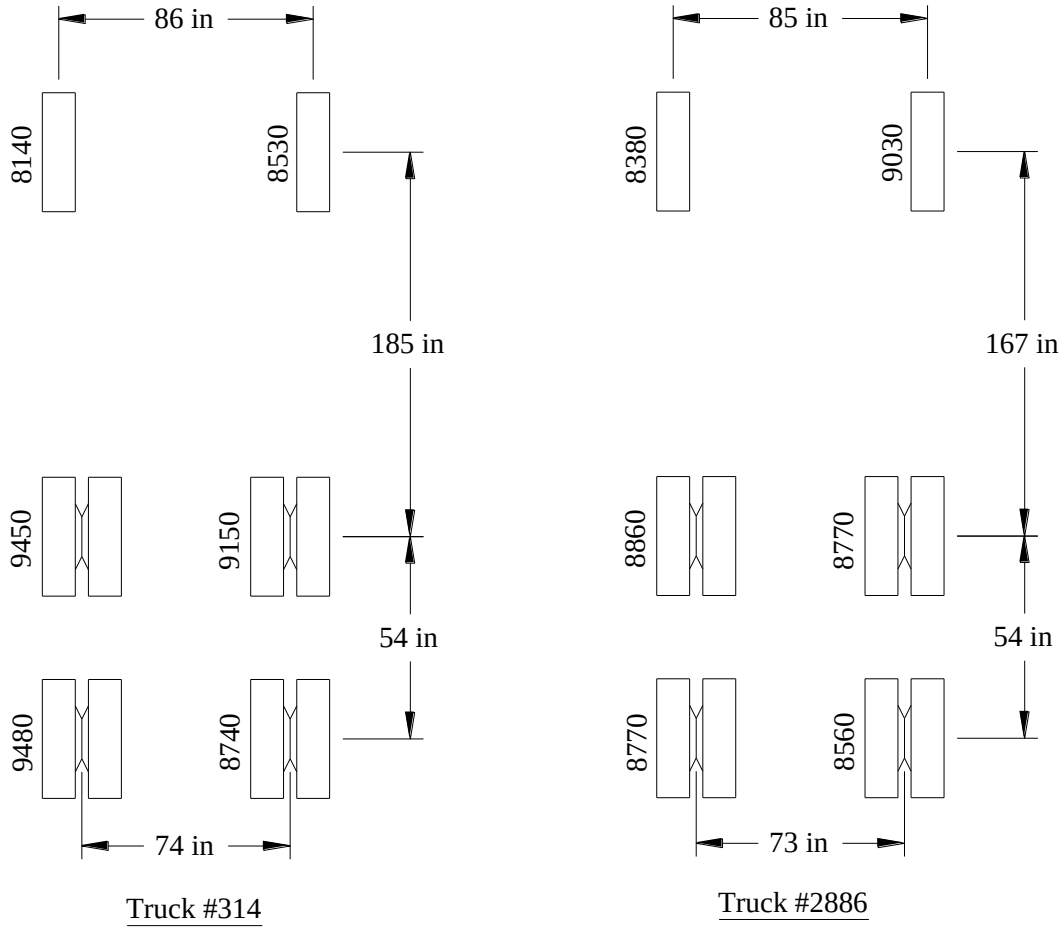

Figure 2.5 Wheel weights (in lbs) and axle configurations for trucks used in load test

During the tests the local traffic on the bridge was stopped. In all load cases, the trucks traveled in the southbound direction. For the Span 10 test the trucks were staged just north of Span 11 until measurements were started. After balancing the strain transducers, the trucks proceeded at a crawl speed of approximately 5-10 mph across the structure. Strain readings were taken at a rate of 20 samples-per-second. After the truck exited Span 9 (the last span of the three span continuous section), the recording was stopped. A similar procedure was used for Span 15, with the vehicles staging just north of Span 16 and recording continued until the vehicle was off of the continuous span, i.e., off of Span 12.

A total of eight truck passes were made, varying the transverse positions of the trucks on the roadway. For each lane that could accommodate a truck (Right Shoulder, Right Lane, and Left Lane), two passes were made, one for each truck (#314, #2886) for a total of six single truck passes. The last two load passes consisted of side-by-side trucks passes with the vehicles in the Right Shoulder/Right Lane and the Right Lane/Left Lane, respectively. The truck runs are listed in Table 2.3

Table 2.3 Truck passes Spans 10 and 15

Pass	Truck ID	Truck Location
1	314	Right shoulder
2	2886	Right shoulder
3	314	Right lane
4	2886	Right lane
5	314	Left lane
6	2886	Left lane
7	314 & 2886	Right shoulder/right lane respectively
8	314 & 2886	Right lane/left lane respectively

Results Span 10

Presented in Table 2.4 are the maximum and minimum recorded stresses for each sensor location, for each truck pass. Table 2.5 lists the corresponding stress ranges (maximum stress minus the minimum stress) for each sensor location. These results are based on the measured strains, using a Modulus of Elasticity for steel of 29,000 ksi. Presented in Figure 2.5 are typical time history plots of the recorded stress in the bottom flange gages for truck pass 1. Presented in Figure 2.6 are typical plots of the recorded stress in the west web of the exterior girder and cross frames for truck pass 1. These plots illustrate the characteristic behavior of the three-span continuous bridge for the sensor readings on the center span, with the girder experiencing first negative bending, then positive bending, and finally negative bending again. The maximum positive bending occurs at gage 317, which is consistent with the truck being in the right shoulder of the bridge.

The absolute maximum stress recorded during the test was 1.87 ksi at gage 295 (bottom flange, west side, section B) in truck pass 8. The absolute minimum stress recorded was -0.61 ksi in gage 294 (cross frame and truck pass 8). The absolute maximum stress range was 2.42 ksi in gage 295 for truck pass 8. For the cross frames, the maximum stress range recorded was 0.70 ksi in gage 294. Other results of the

test showed that the neutral axis of the girder was located in the concrete deck, just above the steel girder top flange. Many more results of the test conducted on span 10 can be found in Kucz (2009).

Results Span 15

Presented in Table 2.6 are the maximum and minimum recorded stresses for each sensor location, for each truck pass. Table 2.7 lists the corresponding stress ranges for each sensor location. These results again are based on the measured strains, using a Modulus of Elasticity for steel of 29,000 ksi.

The absolute maximum stress recorded during the test was 2.68 ksi at gage 355 (bottom flange, west side, section C) in truck pass 7. The absolute minimum stress recorded was -0.75 ksi at gage 337 (bottom flange, east side, section B) in truck pass 8. The absolute maximum stress range was 3.43 ksi in gage 355 for truck pass 7. For the cross frames, the maximum stress range recorded was 0.68 ksi in gage 318 and truck pass 7.

Presented in Figure 2.7 is a plot of the bottom flange gages in Sections A and C for truck pass 1. Similar to the Span 10 results, this plot shows a similar behavior for the 5-span continuous section. Since span 15 is the second span of the 5, the sensor first reads compression when the vehicle is in span 16, it then goes into tension when the load is within span 15, and then back into compression when it has moved onto span 14. A small tensile stress is evident when it is in span 13 and the instrumented section feels very little of the load when it is in the last span, span 12. The transverse distribution of stress is also apparent from the plot. For pass 1 the vehicle is in the right shoulder, thus the west girder carries a majority of the load, thus the stresses are highest in that girder. Figures 2.8 and 2.9 show the stresses in the cross frames at all sections for truck pass 1. One member experiences compression while the other experiences tension. Thus, in addition to the overall bending that it experiences, the box girder is being skewed from its undeformed configuration, which causes the tension in one brace and compression in the other. The behavior was typical for both spans and all sections. Many more results of the test conducted on span 15 can be found in Quigley (2009).

Table 2.4 Maximum and minimum stresses (ksi) for all strain transducers and test runs, Span 10 (negative denotes compression)

	Gage located on:	Gage ID	Run 1		Run 2		Run 3		Run 4		Run 5		Run 6		Run 7		Run 8	
			Max	Min	Max	Min	Max	Min	Max	Min	Max	Min	Max	Min	Max	Min	Max	Min
Section A	top flange	299	0.03	-0.07	0.02	-0.06	0.04	-0.05	0.02	-0.05	0.14	-0.08	0.17	-0.10	0.07	-0.11	0.08	-0.12
	mid-web	339	0.04	-0.01	0.05	-0.04	0.14	-0.07	0.14	-0.05	0.33	-0.05	0.35	-0.05	0.33	-0.08	0.41	-0.09
	bottom flange	292	0.37	-0.23	0.38	-0.22	0.84	-0.37	0.80	-0.23	1.03	-0.27	1.03	-0.28	1.41	-0.47	1.70	-0.48
	cross frame	B1477	0.07	-0.13	0.07	-0.14	0.07	-0.22	0.04	-0.19	0.11	-0.10	0.08	-0.03	0.07	-0.31	0.04	-0.14
	top flange	302	0.02	-0.03	0.01	-0.02	0.02	-0.01	0.02	-0.02	0.13	-0.02	0.11	0.00	0.02	-0.03	0.13	-0.02
	mid-web	535	0.04	-0.08	0.04	-0.08	0.04	-0.14	0.03	-0.12	0.08	-0.07	0.08	-0.07	0.06	-0.18	0.03	-0.16
	bottom flange	356	0.18	-0.21	0.21	-0.21	0.55	-0.45	0.40	-0.26	1.22	-0.36	1.16	-0.36	0.74	-0.49	1.51	-0.56
	cross frame	338	0.11	-0.04	0.10	-0.05	0.17	-0.03	0.17	-0.03	0.03	-0.08	0.03	-0.06	0.27	-0.04	0.11	-0.02
Section B	top flange	306	0.04	-0.04	0.03	-0.05	0.03	-0.07	0.03	-0.05	0.12	-0.06	0.17	-0.08	0.08	-0.12	0.07	-0.10
	mid-web	337	0.04	-0.06	0.03	-0.07	0.05	-0.22	0.03	-0.21	0.09	-0.29	0.10	-0.31	0.07	-0.38	0.09	-0.46
	bottom flange	295	0.40	-0.21	0.44	-0.23	1.01	-0.39	0.85	-0.24	1.16	-0.34	1.16	-0.32	1.55	-0.48	1.87	-0.55
	cross frame	B1475	0.05	-0.09	0.04	-0.10	0.03	-0.14	0.03	-0.12	0.07	-0.04	0.04	-0.03	0.05	-0.19	0.01	-0.08
	mid-web	344	0.02	-0.03	0.02	-0.04	0.03	0.00	0.03	-0.01	0.12	-0.02	0.09	-0.02	0.02	-0.03	0.13	0.00
	top flange	314	0.03	-0.08	0.03	-0.09	0.08	-0.11	0.03	-0.08	0.42	-0.13	0.36	-0.11	0.06	-0.10	0.36	-0.15
	bottom flange	355	0.15	-0.18	0.18	-0.19	0.53	-0.40	0.35	-0.24	1.37	-0.39	1.22	-0.39	0.65	-0.43	1.55	-0.57
Section C	cross frame	294	0.37	-0.08	0.38	-0.09	0.04	-0.38	0.03	-0.36	0.10	-0.31	0.09	-0.30	0.11	-0.16	0.10	-0.61
	mid-web	293	0.58	-0.12	0.58	-0.12	0.92	-0.24	0.91	-0.14	0.39	-0.16	0.38	-0.16	1.19	-0.25	1.20	-0.28
	top flange	298	0.16	-0.03	0.16	-0.03	0.23	-0.02	0.24	-0.02	0.02	-0.03	0.00	-0.05	0.18	-0.02	0.20	-0.03
	bottom flange	303	0.86	-0.33	0.93	-0.31	1.22	-0.45	1.20	-0.30	0.45	-0.27	0.47	-0.25	1.76	-0.58	1.59	-0.50
	top flange	348	0.20	-0.04	0.21	-0.05	0.02	-0.04	0.04	-0.04	0.02	-0.04	0.02	-0.04	0.16	-0.10	0.04	-0.08
	mid-web	346	0.66	-0.11	0.69	-0.11	0.43	-0.17	0.39	-0.12	0.15	-0.10	0.13	-0.10	0.91	-0.19	0.52	-0.20
	bottom flange	317	1.23	-0.33	1.32	-0.31	0.57	-0.38	0.49	-0.27	0.14	-0.19	0.12	-0.17	1.53	-0.51	0.61	-0.38
	cross frame	318	0.05	-0.11	0.06	-0.09	0.11	-0.03	0.13	-0.02	0.09	-0.03	0.07	-0.03	0.04	-0.05	0.19	-0.03

Table 2.5 Stress range (ksi) for all strain transducers and test runs, Span 10

	Gage located on:	Gage ID	Run 1	Run 2	Run 3	Run 4	Run 5	Run 6	Run 7	Run 8
Section A	top flange	299	0.10	0.08	0.08	0.07	0.22	0.27	0.19	0.20
	mid-web	339	0.05	0.09	0.21	0.19	0.39	0.40	0.40	0.49
	bottom flange	292	0.60	0.60	1.21	1.04	1.31	1.31	1.88	2.18
	cross frame	B1477	0.20	0.21	0.29	0.24	0.21	0.11	0.38	0.18
	top flange	302	0.05	0.03	0.03	0.03	0.15	0.11	0.05	0.15
	mid-web	535	0.12	0.11	0.18	0.15	0.15	0.15	0.25	0.20
	bottom flange	356	0.40	0.42	1.01	0.65	1.58	1.52	1.23	2.08
	cross frame	338	0.15	0.15	0.20	0.20	0.11	0.09	0.31	0.13
Section B	top flange	306	0.08	0.08	0.10	0.08	0.18	0.25	0.20	0.17
	mid-web	337	0.10	0.10	0.28	0.24	0.38	0.41	0.45	0.55
	bottom flange	295	0.62	0.67	1.40	1.09	1.49	1.48	2.03	2.42
	cross frame	B1475	0.14	0.14	0.17	0.15	0.11	0.07	0.24	0.10
	mid-web	344	0.05	0.05	0.03	0.03	0.14	0.10	0.05	0.14
	top flange	314	0.11	0.13	0.19	0.11	0.55	0.47	0.16	0.50
	bottom flange	355	0.33	0.37	0.93	0.59	1.75	1.62	1.08	2.13
Section C	cross frame	294	0.45	0.47	0.42	0.38	0.42	0.38	0.27	0.70
	mid-web	293	0.70	0.70	1.16	1.05	0.55	0.55	1.44	1.48
	top flange	298	0.19	0.19	0.25	0.25	0.05	0.05	0.20	0.24
	bottom flange	303	1.19	1.24	1.66	1.49	0.72	0.72	2.33	2.08
	top flange	348	0.24	0.26	0.06	0.08	0.06	0.06	0.26	0.12
	mid-web	346	0.77	0.80	0.61	0.52	0.25	0.23	1.10	0.71
	bottom flange	317	1.56	1.63	0.95	0.76	0.33	0.30	2.04	0.99
	cross frame	318	0.15	0.15	0.14	0.15	0.12	0.10	0.09	0.22

Table 2.6 Maximum and minimum stresses (ksi) for all strain transducers and test runs, Span 15 (negative denotes compression)

	Gage located on:	Gage ID	Run 1		Run 2		Run 3		Run 4		Run 5		Run 6		Run 7		Run 8	
			Max	Min	Max	Min	Max	Min	Max	Min	Max	Min	Max	Min	Max	Min	Max	Min
Section A	A: Top Flange Left	295	0.02	-0.02	0.03	-0.02	0.02	-0.01	0.04	-0.01	0.17	-0.01	0.14	-0.01	0.03	-0.02	0.16	-0.01
	B: Left Web	317	0.09	-0.12	0.06	-0.11	0.17	-0.16	0.14	-0.11	0.89	-0.23	0.81	-0.20	0.23	-0.18	0.87	-0.29
	C: Bottom Flange Left	293	0.33	-0.30	0.30	-0.20	0.65	-0.38	0.63	-0.33	1.70	-0.44	1.68	-0.41	0.99	-0.52	2.16	-0.68
	D: Bottom Flange Right	314	0.53	-0.28	0.52	-0.23	1.16	-0.29	1.00	-0.27	1.00	-0.25	1.14	-0.25	1.68	-0.45	2.03	-0.45
	E: Right Web	338	0.08	-0.10	0.08	-0.06	0.30	-0.14	0.26	-0.10	0.62	-0.18	0.64	-0.17	0.49	-0.17	0.88	-0.28
	F: Top Flange Right	299	0.05	-0.09	0.05	-0.09	0.05	-0.10	0.05	-0.10	0.05	-0.10	0.10	-0.12	0.07	-0.19	0.07	-0.20
	H: Cross frame 2	318	0.19	-0.47	0.70	-0.23	0.04	-0.57	0.09	-0.70	0.81	-0.21	0.40	-0.49	0.09	-1.52	0.23	-0.16
Section B	A: Top Flange Left	302	0.02	-0.29	0.02	-0.27	0.02	-0.39	0.02	-0.34	0.11	-0.08	0.08	-0.06	0.03	-0.56	0.10	-0.19
	B: Left Web	348	0.07	-0.03	0.03	-0.03	0.16	-0.03	0.10	-0.03	0.93	-0.02	0.81	-0.02	0.14	-0.05	0.80	-0.03
	C: Bottom Flange Left	337	0.34	-0.15	0.31	-0.13	0.68	-0.16	0.64	-0.16	1.73	-0.25	1.65	-0.25	0.98	-0.26	2.12	-0.38
	D: Bottom Flange Right	292	0.54	-0.30	0.52	-0.32	1.23	-0.41	1.10	-0.36	1.08	-0.46	1.21	-0.46	1.87	-0.71	2.16	-0.75
	E: Right Web	306	0.08	-0.28	0.06	-0.32	0.25	-0.33	0.21	-0.30	0.42	-0.30	0.44	-0.33	0.43	-0.61	0.62	-0.54
	F: Top Flange Right	535	0.04	-0.09	0.05	-0.09	0.05	-0.11	0.05	-0.11	0.05	-0.13	0.12	-0.13	0.08	-0.18	0.06	-0.22
	G: Cross frame 1	1475	0.25	-0.06	0.25	-0.06	0.36	-0.03	0.33	-0.03	0.09	-0.23	0.07	-0.16	0.55	-0.08	0.12	-0.06
	H: Cross frame 2	1477	0.08	-0.21	0.08	-0.20	0.03	-0.30	0.03	-0.27	0.18	-0.07	0.14	-0.06	0.08	-0.43	0.04	-0.17
Section C	A: Top Flange Left	344	0.12	-0.02	0.12	-0.02	0.19	-0.02	0.22	-0.02	0.02	-0.05	0.02	-0.05	0.19	-0.02	0.19	-0.04
	B: Left Web	298	0.45	-0.13	0.42	-0.15	1.05	-0.18	0.98	-0.16	0.46	-0.19	0.49	-0.19	1.26	-0.24	1.37	-0.28
	C: Bottom Flange Left	356	1.19	-0.37	1.15	-0.29	1.56	-0.38	1.44	-0.36	0.63	-0.30	0.71	-0.30	2.49	-0.64	2.07	-0.62
	D: Bottom Flange Right	355	2.11	-0.49	1.99	-0.39	1.13	-0.44	1.23	-0.43	0.50	-0.32	0.58	-0.34	2.68	-0.74	1.58	-0.69
	E: Right Web	339	0.93	-0.19	0.91	-0.16	0.48	-0.17	0.50	-0.15	0.18	-0.12	0.22	-0.13	1.10	-0.28	0.63	-0.28
	F: Top Flange Right	303	0.25	-0.02	0.25	0.00	0.04	-0.01	0.06	-0.01	0.03	-0.02	0.03	-0.02	0.26	-0.03	0.05	-0.04
	G: Cross frame 1	346	0.05	-0.03	0.09	0.00	0.15	-0.01	0.15	0.01	0.14	-0.02	0.15	-0.01	0.03	-0.02	0.30	-0.02
	H: Cross frame 2	294	0.34	-0.03	0.36	0.02	0.03	-0.15	0.03	-0.12	0.05	-0.15	0.07	-0.13	0.09	-0.03	0.05	-0.24

Table 2.7 Stress range (ksi) for all strain transducers and test runs, Span 15

	Gage located on:	Gage ID	Run 1	Run 2	Run 3	Run 4	Run 5	Run 6	Run 7	Run 8
Section A	A: Top Flange Left	295	0.03	0.05	0.03	0.05	0.18	0.15	0.05	0.16
	B: Left Web	317	0.21	0.16	0.33	0.25	1.12	1.00	0.41	1.15
	C: Bottom Flange Left	293	0.63	0.50	1.03	0.96	2.14	2.09	1.51	2.84
	D: Bottom Flange Right	314	0.81	0.75	1.44	1.27	1.25	1.40	2.13	2.48
	E: Right Web	338	0.18	0.15	0.44	0.37	0.81	0.81	0.66	1.15
	F: Top Flange Right	299	0.13	0.13	0.15	0.15	0.15	0.22	0.25	0.27
	H: Cross frame 2	318	0.39	0.38	0.44	0.39	0.34	0.22	0.68	0.24
Section B	A: Top Flange Left	302	0.05	0.05	0.05	0.05	0.13	0.10	0.08	0.13
	B: Left Web	348	0.22	0.16	0.32	0.26	1.18	1.06	0.40	1.18
	C: Bottom Flange Left	337	0.64	0.62	1.09	1.00	2.19	2.10	1.69	2.86
	D: Bottom Flange Right	292	0.82	0.84	1.56	1.39	1.37	1.54	2.48	2.70
	E: Right Web	306	0.17	0.15	0.35	0.32	0.55	0.57	0.60	0.84
	F: Top Flange Right	535	0.13	0.13	0.15	0.13	0.15	0.21	0.26	0.26
	G: Cross frame 1	1475	0.31	0.31	0.39	0.36	0.32	0.22	0.63	0.18
	H: Cross frame 2	1477	0.29	0.28	0.33	0.31	0.25	0.20	0.52	0.21
Section C	A: Top Flange Left	344	0.14	0.14	0.21	0.24	0.07	0.07	0.21	0.23
	B: Left Web	298	0.58	0.56	1.22	1.14	0.65	0.68	1.49	1.65
	C: Bottom Flange Left	356	1.56	1.44	1.94	1.80	0.93	1.01	3.13	2.69
	D: Bottom Flange Right	355	2.60	2.38	1.58	1.65	0.83	0.93	3.43	2.27
	E: Right Web	339	1.12	1.07	0.65	0.65	0.30	0.35	1.39	0.91
	F: Top Flange Right	303	0.27	0.25	0.05	0.07	0.05	0.05	0.29	0.08
	G: Cross frame 1	346	0.09	0.09	0.16	0.14	0.16	0.16	0.05	0.32
	H: Cross frame 2	294	0.37	0.33	0.18	0.15	0.20	0.20	0.12	0.28

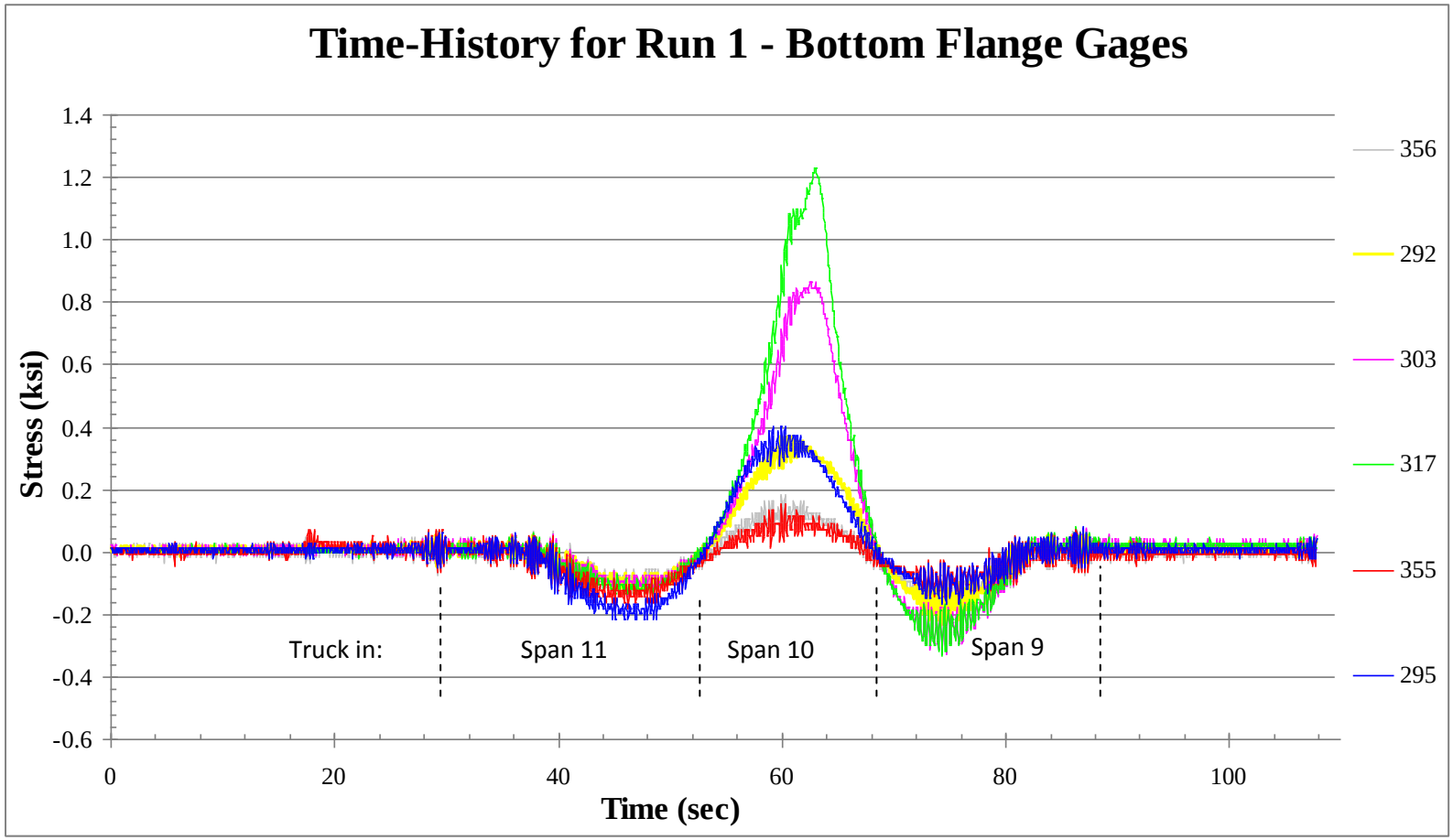

Figure 2.6 Time-history plot of the bottom flange gages for pass 1 at all Sections (A, B, C)

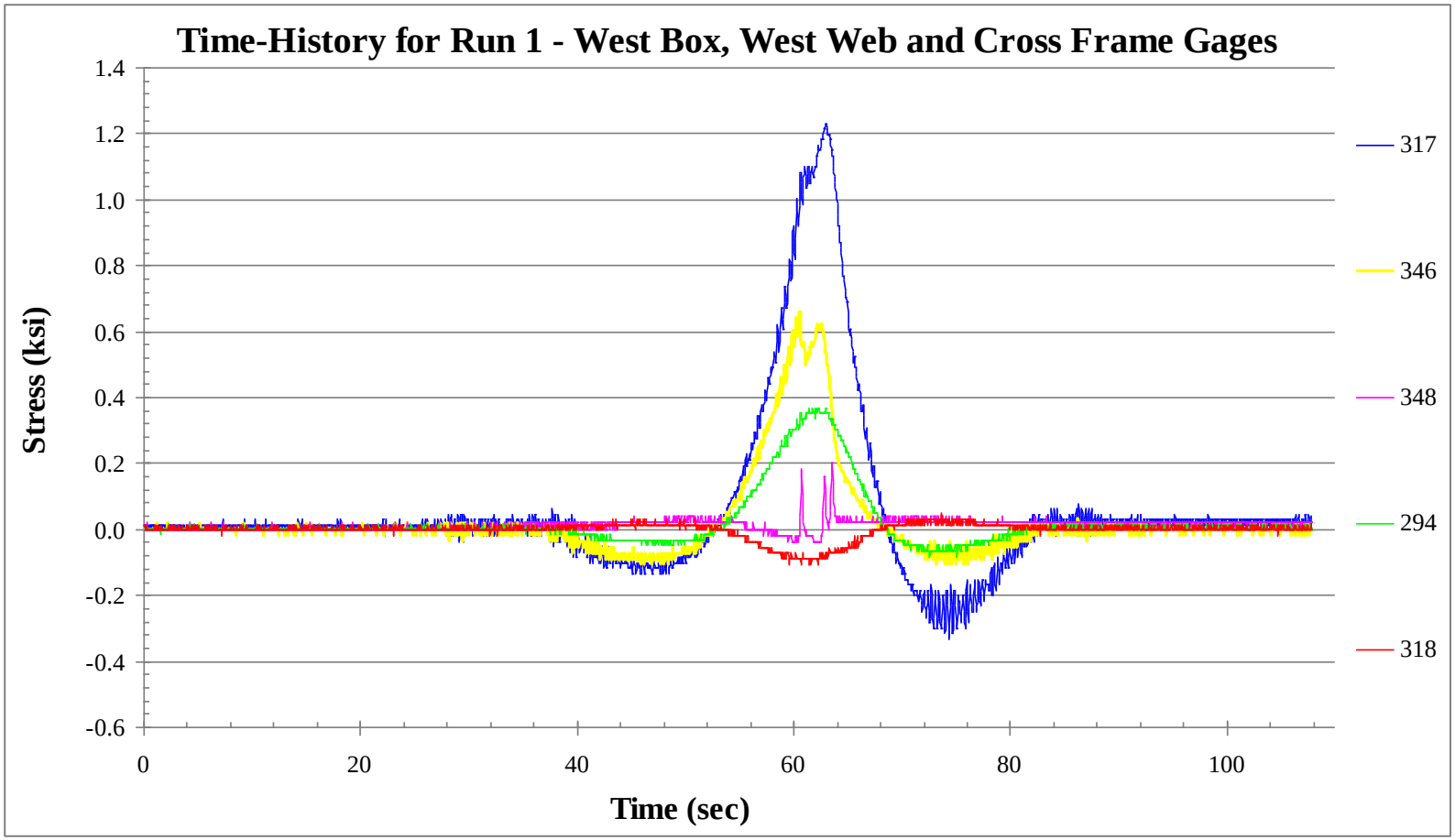

Figure 2.7 Time-history plot of the gages on the west girder, west web and west girder cross frames for pass 1 (Section C)

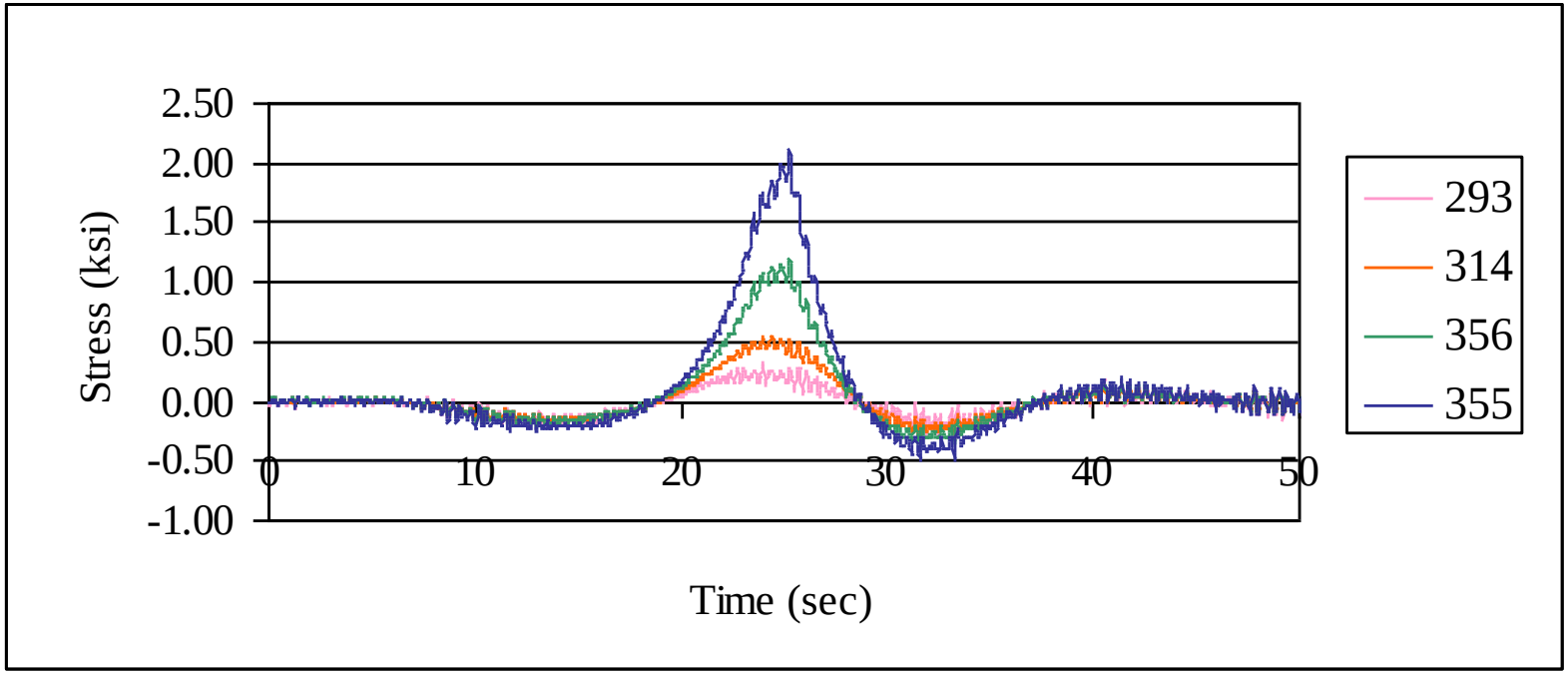

Figure 2.8 Time-history plot of bottom flange gages, Sections A and C, Span 15, truck pass 1

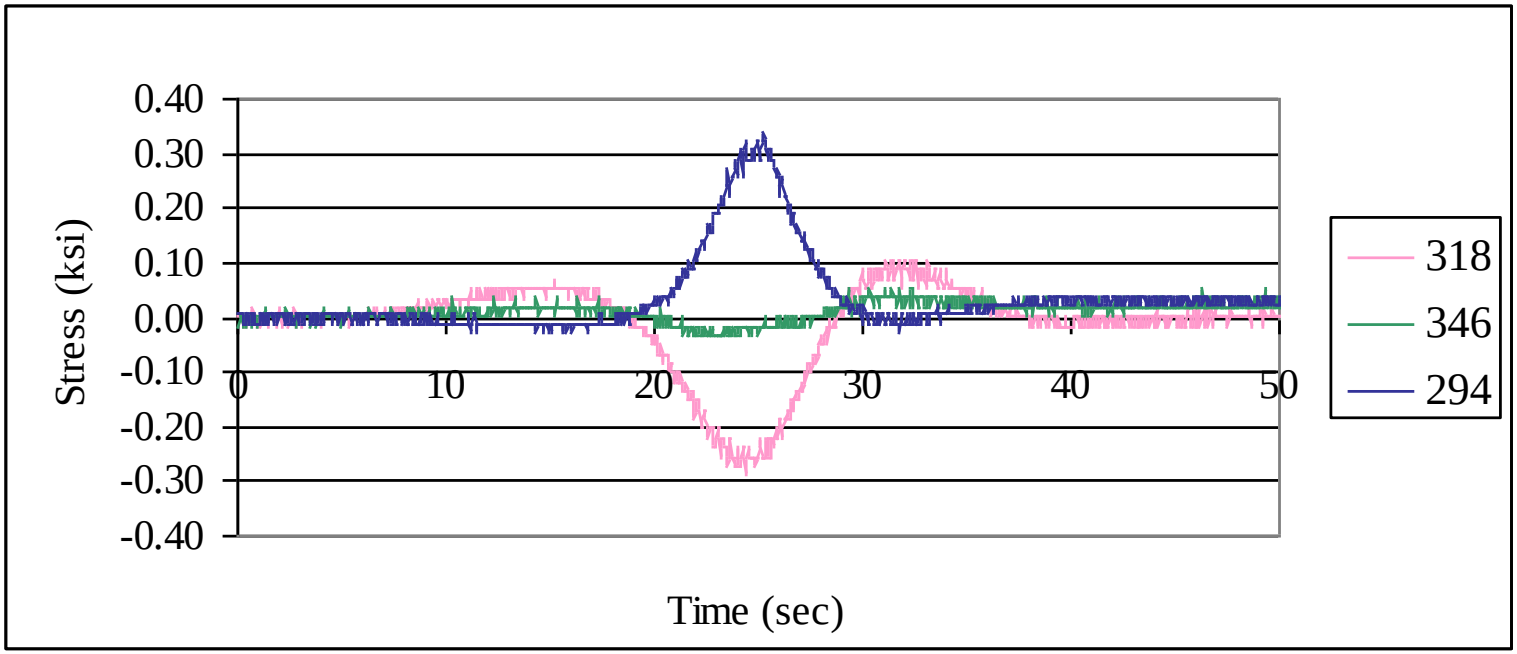

Figure 2.9 Time-history plot of cross frame gages, Sections A and C, Span 15, truck pass 1

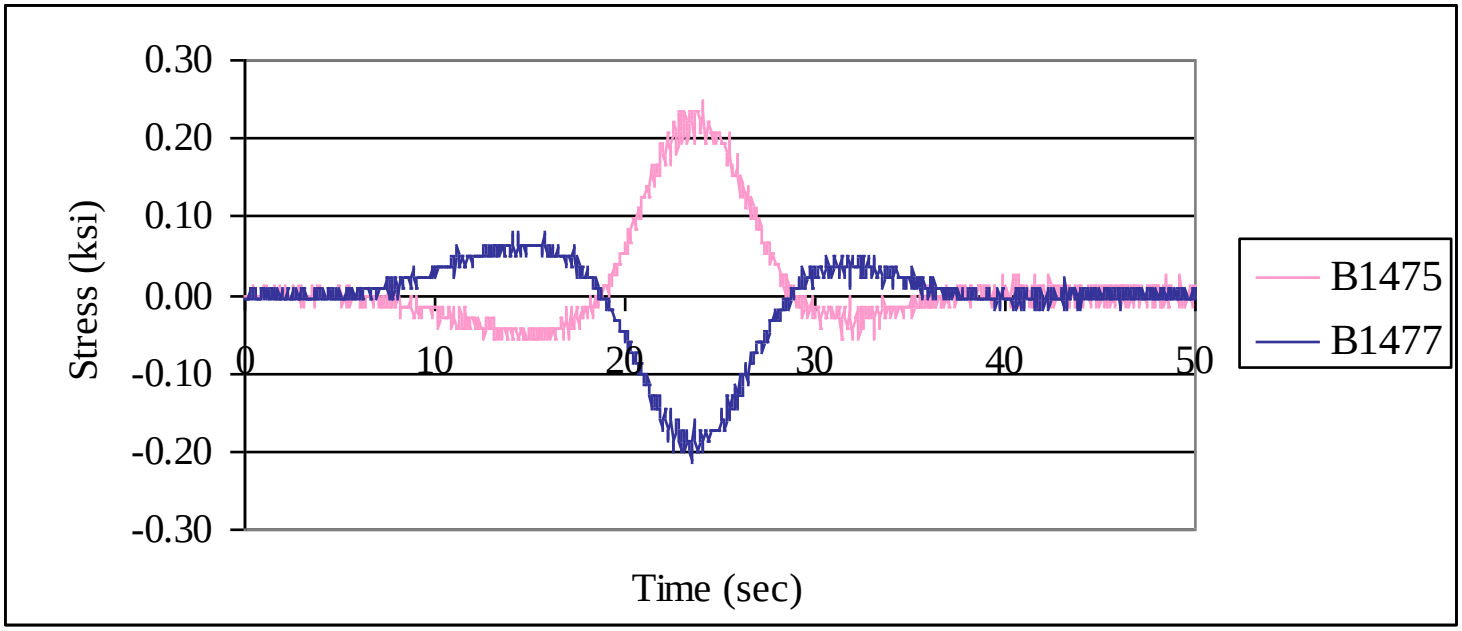

Figure 2.10 Time-history plot of cross frame gages, Section B, Span 15, truck pass 1

2.3 In-Service Monitoring of Span 10

In-service monitoring of the exterior (west) girder in Span 10 was conducted to gather data for the fatigue life evaluation. On November 17, 2010 a monitoring system consisting of 8 strain gages, data logger and power source was installed in locations of interest near one Type E diaphragm on Span 10. Strains were recorded for a period of 23 days and the monitoring system was retrieved on December 16, 2010. The purpose of the monitoring was to directly measure the magnitude and number of loading cycles caused by the site specific traffic, in various members and locations of the cross section. The data obtained was used in conjunction with the finite element models discussed in Chapter 3 to determine the effective stress at the weld toe of the Type E diaphragm connection. A comprehensive description of the instrumentation plan, equipment used, test setup and data obtained is presented in the next sections.

Test Setup

The instrumentation plan (Figure 2.11) was designed with several goals in mind. First, it was desired to record stresses at the web gap region. Because the web gap is a very confined space, and the stress gradients within it are expected to be very high, it was not possible to use the 3" BDI transducer in this area. Instead, small weldable resistive foil strain gages were chosen for this purpose and were installed in both the top web gap region and the bottom web gap region. The foil strain gages, which had a gage length of 0.72", were centered 1" from the end of the connection plate and oriented to measure the strain in the web gage in a direction parallel to the connection plate, i.e., perpendicular to the flange. This placed the end of the sensor at the base of the weld toe. Figure 2.12 shows a photograph of one of the weldable strain gages installed in the web gap region.

Next, it was desired to measure cross frame forces. To accomplish this, BDI strain transducers were clamped to the bolted angle legs of the cross frame members. Next, it was desired to determine the number of loading cycles the bridge was subject to. For this purpose, BDI transducers were bonded to the bottom flange and mid-web of the box girder. Lastly, BDI transducers were installed adjacent to connection plate at the beginning of the web gap. These gages were used to gain information on the stress distribution surrounding the web gap region and compare it to the results of the finite element models. Figure 2.13 shows the BDI transducers on the web.

The sensors were installed on the second Type E diaphragm from Pier 10, in the southbound exterior (west) box girder of Span 10 (Figure 2.2). Assuming most trucks travel in the right lane, this location was chosen with the intent of primarily capturing their effects. Emphasis was placed on recording the effects of truck traffic since research suggests that a vehicle weighing less than 20 kips "has a very low probability of causing fatigue damage" (Alampalli, 2006).

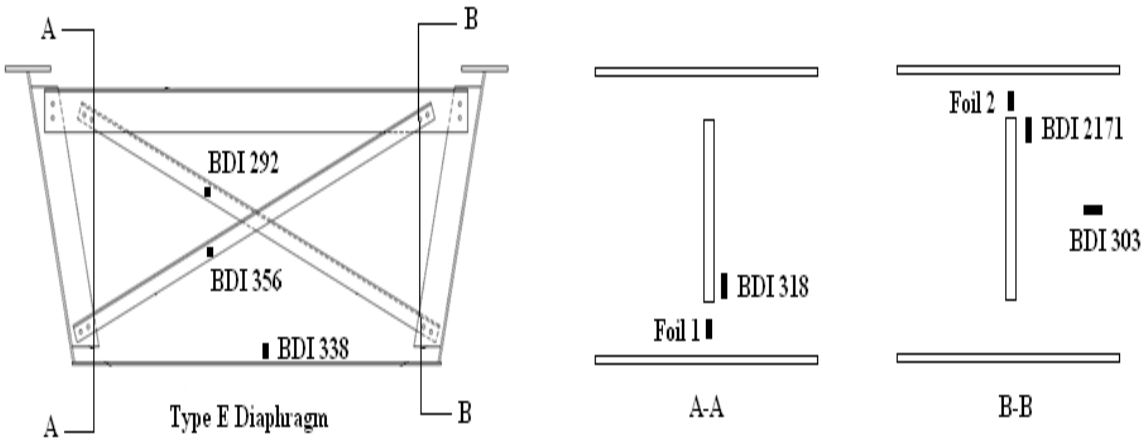

Figure 2.11 Layout of gage locations for in-service monitoring on Span 10

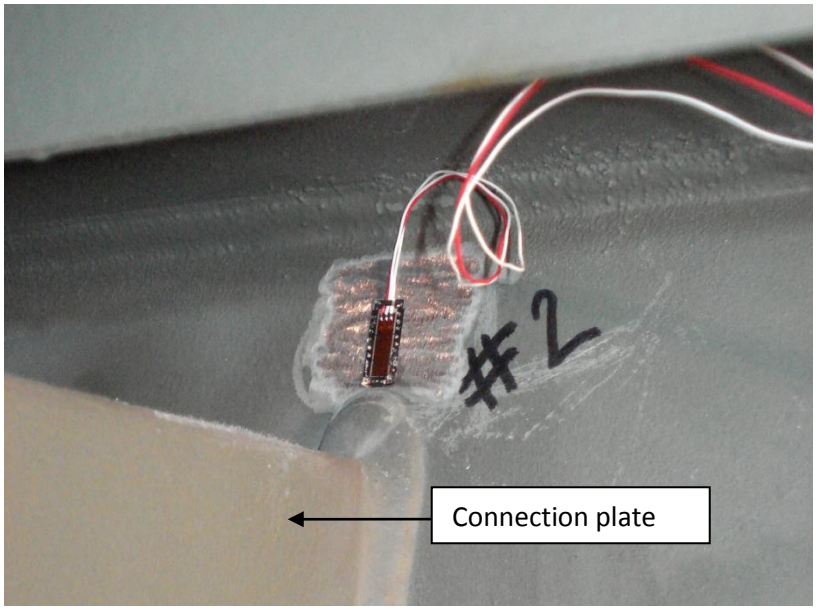

Figure 2.12 Weldable strain gage mounted in web gap

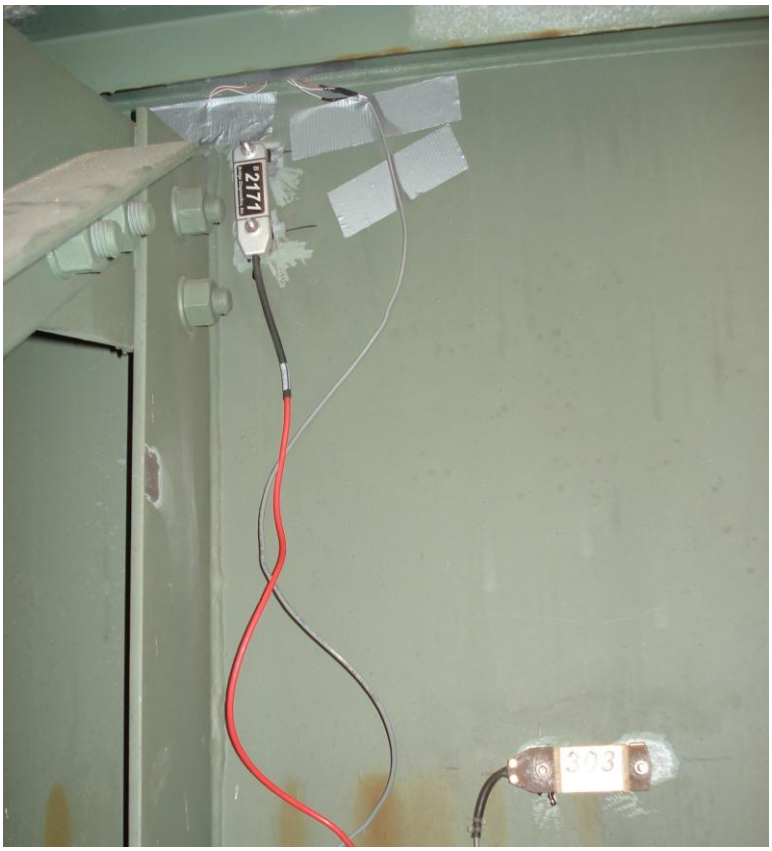

Figure 2.13 Strain transducers mounted to web

Data was recorded using a Campbell Scientific CR5000 data logger. The CR5000 data logger has a maximum sample rate of 5,000 samples/second (for one channel) and a 16-bit A/D convertor. The CR5000 was powered by a pair of heavy duty 12 volt batteries. Remote access to the CR5000 was provided by a Raven XTV cellular modem. To conserve battery power the CR5000 was programmed to turn the modem on at 11:00 am each day and turn off the modem at 1:00 pm each day, thereby providing a 2 hour window within which to communicate with the logger for system check-out and data downloads. Programming of the CR5000 datalogger was done using Campbell Scientific's Real Time Data Acquisition (RTDAQ) software package. RTDAQ was also used to communicate with the logger via the modem and to download the data remotely. A full mock-up of the instrumentation system, including dummy sensors, was assembled in the laboratory prior to the test, to ensure that the battery power would be sufficient to last at least 21 days in the field and that the cellular modem system was operating properly. The system was retrieved after 29 days in the field and it was still running, albeit with a significant drop in voltage.

Strain readings were taken at a rate of 100 samples-per-second, which was determined to be sufficient given the span length of the bridge and the expected maximum speed of vehicles crossing. The data was processed "on the fly" by the logger and stored in several different output "tables," to reduce the amount of data that needed to be stored and downloaded. The data was processed using the Rainflow algorithm, which is a procedure for determining an equivalent number of constant amplitude cycles of a randomly varying signal. The rainflow output table was recorded every 10 minutes. Another output

table was used to capture the maximum and minimum strain values recorded by each strain gage every 60 seconds. While significantly lower than the 100Hz scan rate, this output table will show extreme events at the Newport Viaduct on 60 second intervals. Finally, an output table was created to record battery voltage every 30 minutes. Finally, although storing all of the raw time history strain data would have been prohibitive, a few hours of raw data was collected and stored during the early morning hours of one day so that sample time histories of the response due to the site specific traffic could be reviewed.

Test Results

Presented in Tables 2.8 and 2.9 is the Rainflow histogram data for all of the strain gages. The plan was to have the strain ranges equal for both the BDI transducers and the foil strain gages, however, because of an error in programming the CR5000 the bin ranges were not the same, thus the data are presented in separate tables. The first column is the bin number, the second column the bin strain range, the third column is the mid-range stress (assuming a Modulus of Elasticity for steel equal to 29,000 ksi). For each sensor the number of equivalent cycles recorded in that stress range is noted.

For all sensors the number of cycles decrease with increasing stress range, and the largest number of cycles corresponds to the lowest stress range. The greatest number of cycles was recorded with BDI sensor 318, which was located on the web next to the connection plate, but the vast majority of these occurred in the lowest bin. For the foil gage sensors the largest number of cycles was recorded for foil gage #1, which was located in the bottom web gap. The total number of cycles experienced by the gage in the top web gap was less than 2% of that of the bottom web gap. Sample histograms, of the data for foil gage #1, are shown in Figures 2.13 and 2.14.

Sample time history data was also recorded: time histories of a heavy vehicle crossing the bridge are shown in Figures 2.15 through 2.18.

Further details of the in-service monitoring can be found in Soto Fuentes (2011).

Table 2.8 Rainflow histogram data for BDI strain transducers

Bin	Range (με)	σ (ksi)	BDI 303 MW	BDI 292 XF #1	BDI 2171 TWG	BDI 338 BF	BDI 356 XF#2	BDI 318 BWG
1	5-9.5	0.21	18333	553042	919105	22012	187501	1332271
2	9.5-19	0.41	0	125691	377071	10579	36252	599404
3	19-28.5	0.69	0	16470	45253	2129	5294	75955
4	28.5-38	0.96	0	4818	13882	224	2027	21017
5	38-47.5	1.24	0	2088	6325	1	637	9617
6	47.5-57	1.52	0	1348	3088	0	84	4478
7	57-66.5	1.79	0	665	2070	0	2	2504
8	66.5-76	2.07	0	239	1508	0	0	1531
9	76-85.5	2.34	0	73	841	0	0	987
10	85.5-95	2.62	0	6	448	0	0	805
11	95-104.5	2.89	0	1	333	0	0	555
12	104.5-114	3.17	0	0	232	0	0	331
13	114-123.5	3.44	0	0	156	0	0	200
14	123.5-133	3.72	0	0	80	0	0	130
15	133-142.5	3.99	0	0	41	0	0	71
16	142.5-152	4.27	0	0	10	0	0	28
17	152-161.5	4.55	0	0	1	0	0	10
18	161.5-171	4.82	0	0	2	1	0	4
19	171-180.5	5.10	0	0	1	0	0	1
20	180.5-190	5.37	0	0	0	0	0	0

Table 2.9 Rainflow histogram data for foil strain gages

Bin	με	σ (ksi)	FG #1 Bottom	FG #2 Top
2	5-10	0.22	1242117	19389
3	10-15	0.36	202413	3315
4	15-20	0.51	59385	1075
5	20-25	0.65	22449	344
6	25-30	0.80	9701	117
7	30-35	0.94	4790	30
8	35-40	1.09	2558	8
9	40-45	1.23	1436	0
10	45-50	1.38	805	0
11	50-55	1.52	406	0
12	55-60	1.67	239	0
13	60-65	1.81	134	0
14	65-70	1.96	79	0
15	70-75	2.10	49	0
16	75-80	2.25	35	0
17	80-85	2.39	22	0
18	85-90	2.54	13	0
19	90-95	2.68	10	0
20	95-100	2.83	9	0
21	100-105	2.97	7	0
22	105-110	3.12	3	0
23	110-115	3.26	3	0
24	115-120	3.41	1	0
25	120-125	3.55	3	0
26	125-130	3.70	0	0
27	130-135	3.84	2	0
28	135-140	3.99	0	0
29	140-145	4.13	3	0
30	145-150	4.28	1	0
31	150-155	4.42	0	0
32	155-160	4.57	0	0
33	160-165	4.71	0	0
34	165-170	4.86	0	0
35	170-175	5.00	0	0
36	175-180	5.15	0	0
37	180-185	5.29	0	0
38	185-190	5.44	2	0

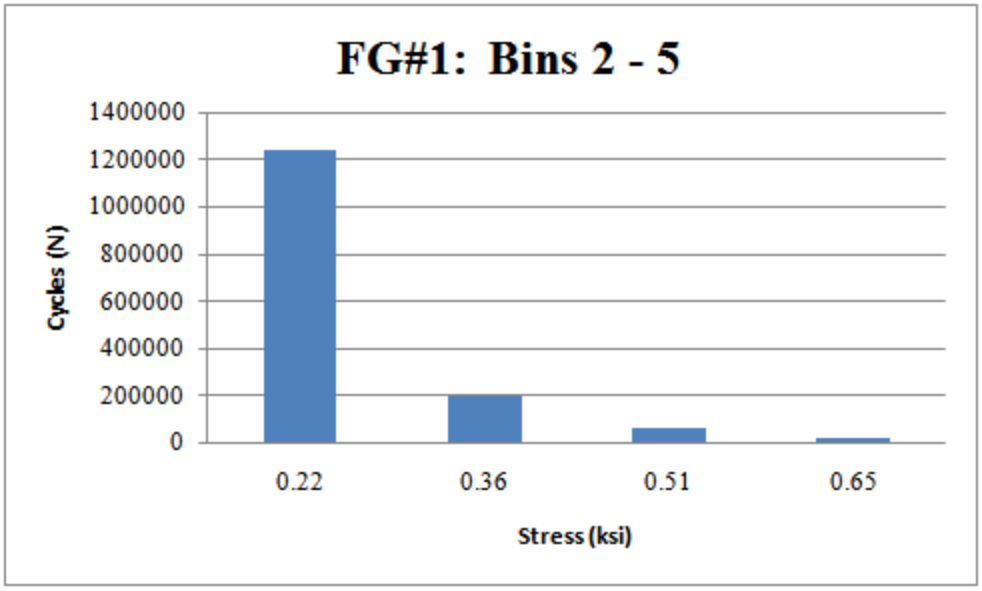

Figure 2.14 Rainflow histogram for foil gage #1, bins 2-5.

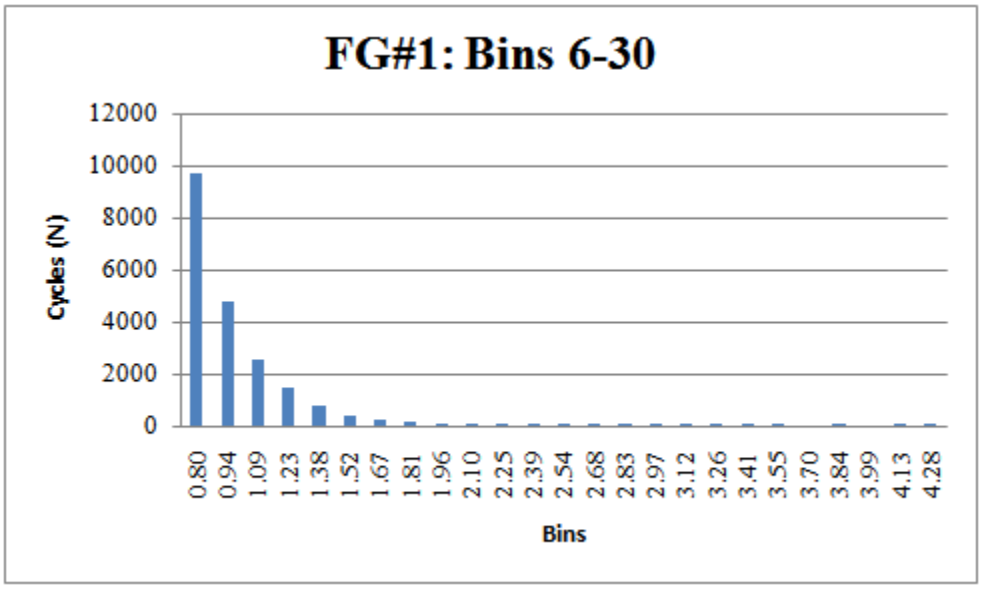

Figure 2.15 Rainflow histogram for foil gage #1, bins 6-30.

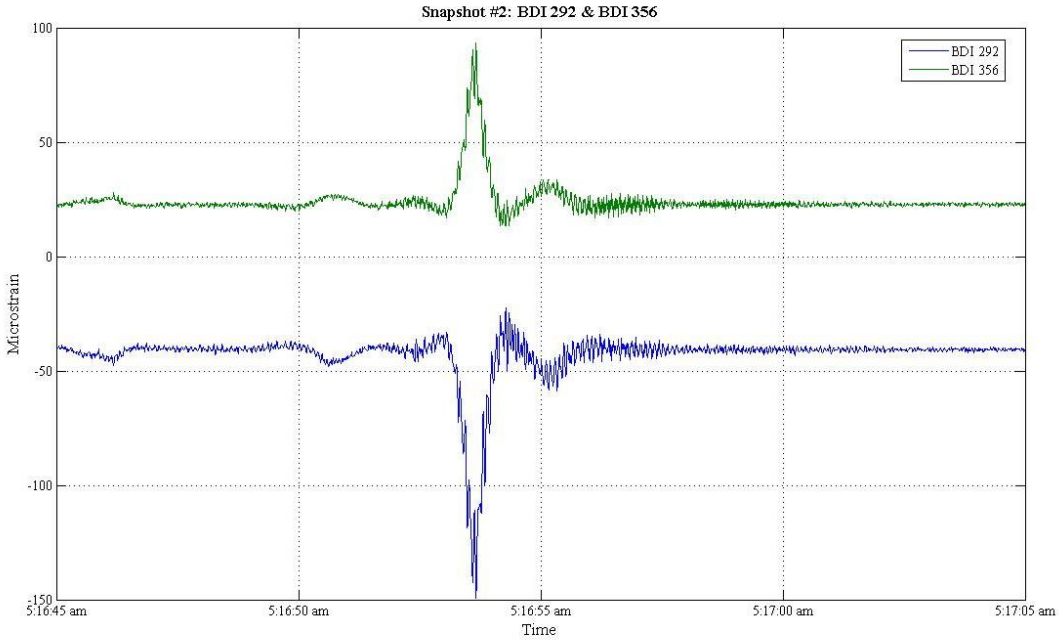

Figure 2.16 Snapshot event #2 cross frame gages.

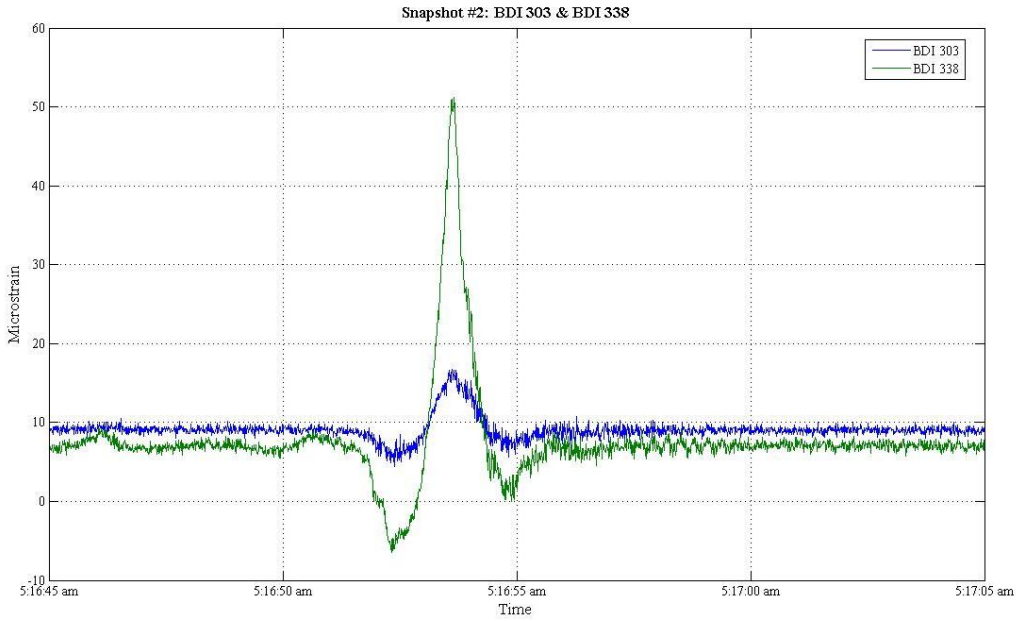

Figure 2.17 Snapshot event #2 mid-web and bottom flange gages.

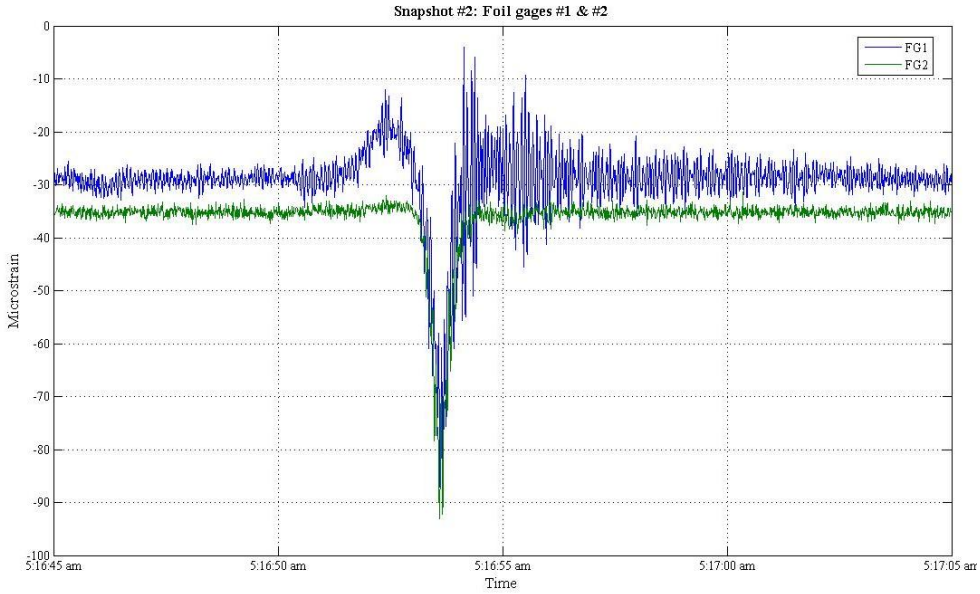

Figure 2.18 Snapshot event #2 web gap foil gages #1 & #2.

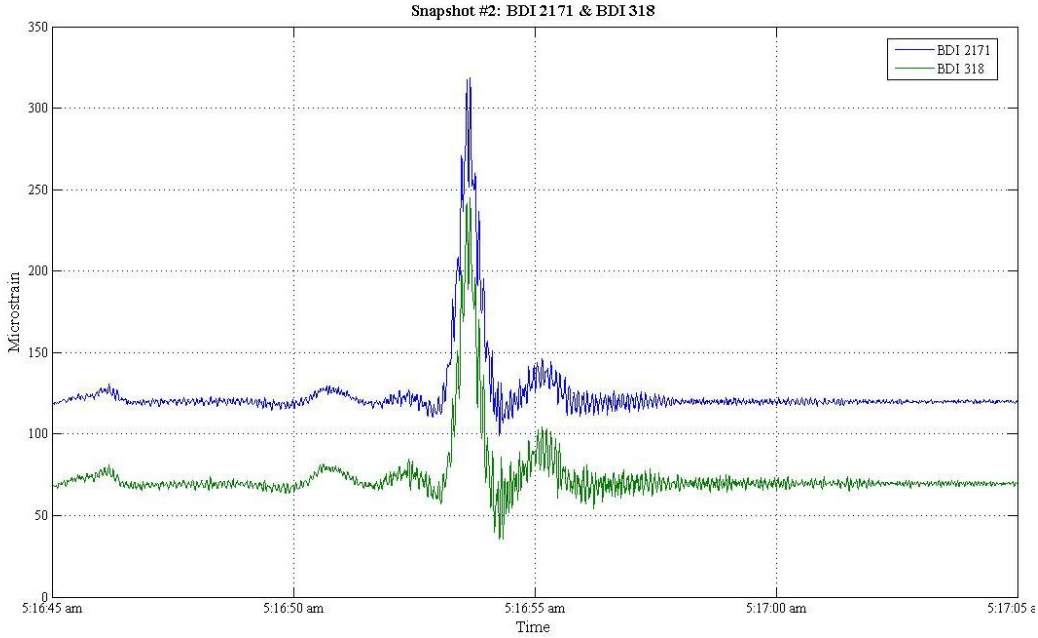

Figure 2.19 Snapshot event #2 BDI gages adjacent to connection plate.

3 Finite Element Modeling

3.1 Introduction

A series of global and local Finite Elements (FE) models of the bridge were developed to be used for the fatigue evaluation, and for evaluation of potential retrofit and repair strategies. A global model was developed of spans 9 through 11, and also one of spans 12 through 16. These models were large, complex, high-fidelity models, designed to capture the overall deformation and stresses induced in the bridge by the heavy traffic. They were sufficient to resolve the stresses and deformations down to a spatial resolution of about a few inches. Note, however, that the global models were created to represent the original undamaged (uncracked) sections of the viaduct, i.e., no attempt was made to include the actual cracks in the connections. To that extent the models were developed to represent the original condition of the bridge when it was first placed in service.

To capture the detailed stresses occurring in the connection region, where the cracks have formed, a local, detailed 3D model of the crack region was also developed. This was used to investigate the response in detail by the crack zone. The global models were calibrated using the field test results. The models were then used to investigate the fatigue life of the connections and to investigate potential repair strategies. Presented in this chapter are the FE models and the results of the calibration. The application of the models for the fatigue life evaluation and retrofit investigation are presented in Chapters 4 and 5.

3.2 Global bridge models

Description of the models

Global models were created for spans 9 to 11 (referred to here as the “Span-10”, or “S10” model) and spans 12 to 16 (referred to here as the “Span-15” or “S15” model). Both were created using a very similar approach and to the same degree of accuracy and resolution. A detailed description is presented for model S10, a similar approach was used for the S15 model. Where there are differences or unique features to the S15 model these are discussed.

The FE models were developed thru a three step process. In the first step, the geometry of the spans was created in AutoCAD 2004. The AutoCAD model was then imported into FEMAP (v. 9.31) and meshed. After meshing, the FEMAP preprocessor model was converted to an ABAQUS input file. The ABAQUS solver was then used to process the input file, calculate the finite element results, and post-process the results.

With the exception of the diaphragm cross frame members, 3-and-4-sided reduced integration shell elements (S3R and S4R in ABAQUS) were used for the entire model, which included the two adjacent

girders, deck, and parapets. The piers were not modeled but were represented using appropriate girder support conditions. The cross frame members were modeled as 3D beam elements (B31 in ABAQUS). There were a total of 160,135 elements and 165,733 nodes in the S10 model. Figure 3.1 shows the completed S10 model. Figure 3.2 shows the completed S10 model without the deck.

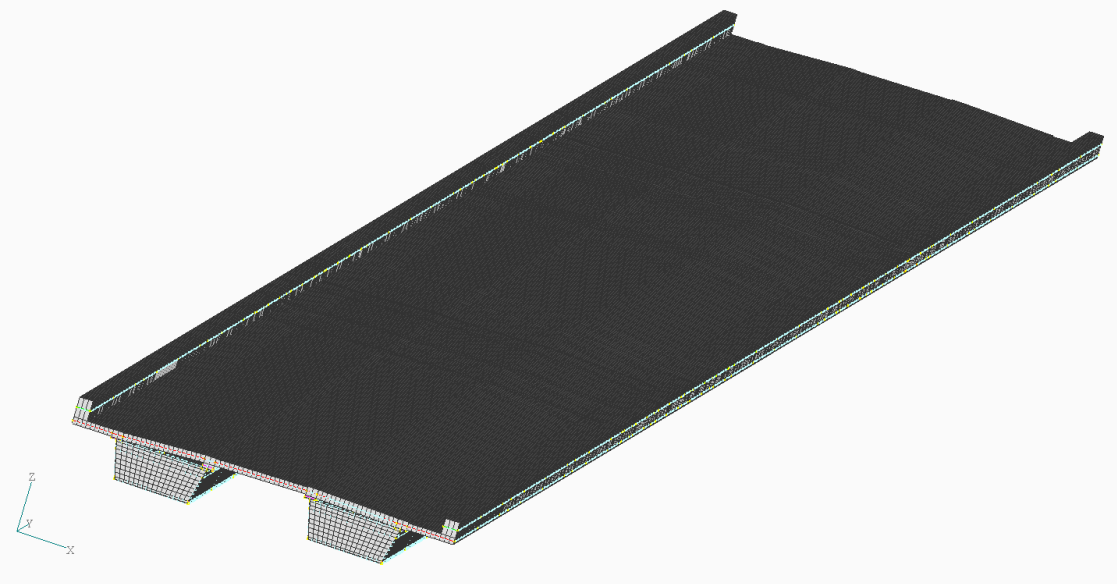

Figure 3.1 General view of the S10 (Span 9-11) finite element model

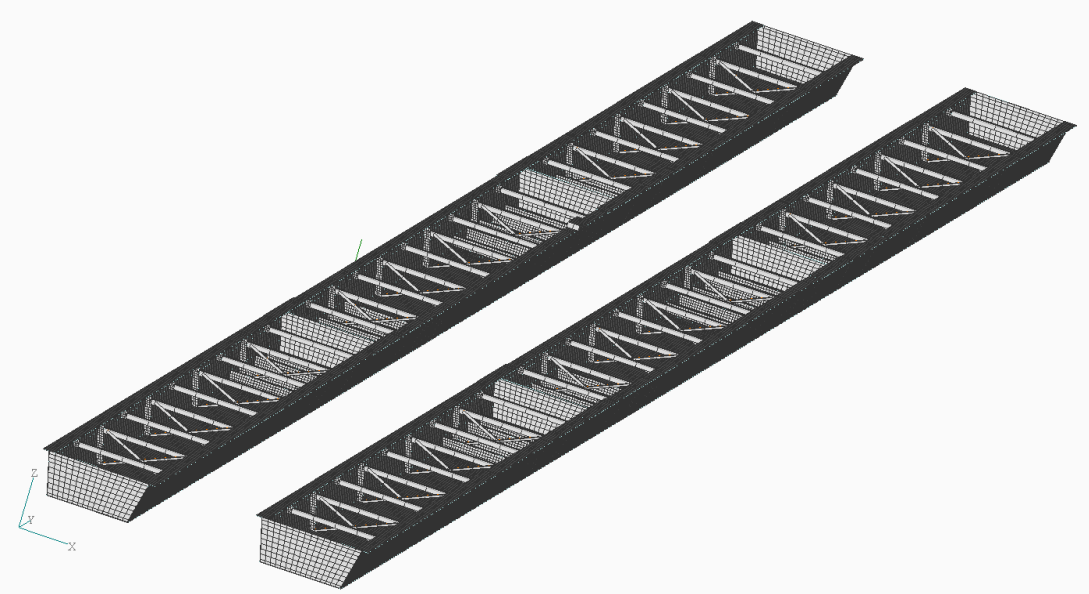

Figure 3.2 View of interior of box girders including interior components

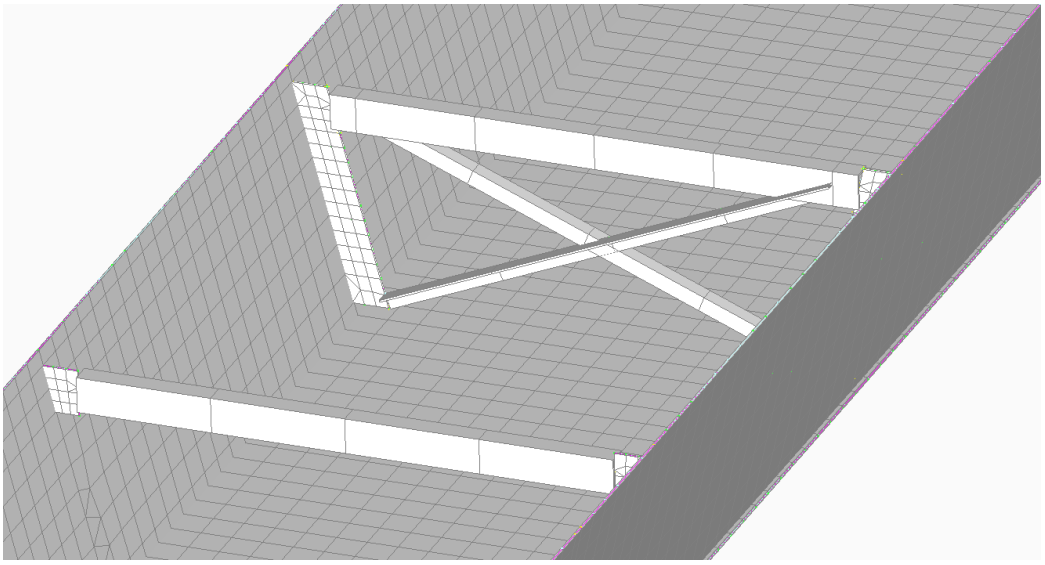

Figure 3.3 View of type E and type F diaphragm FE mesh in interior of boxes

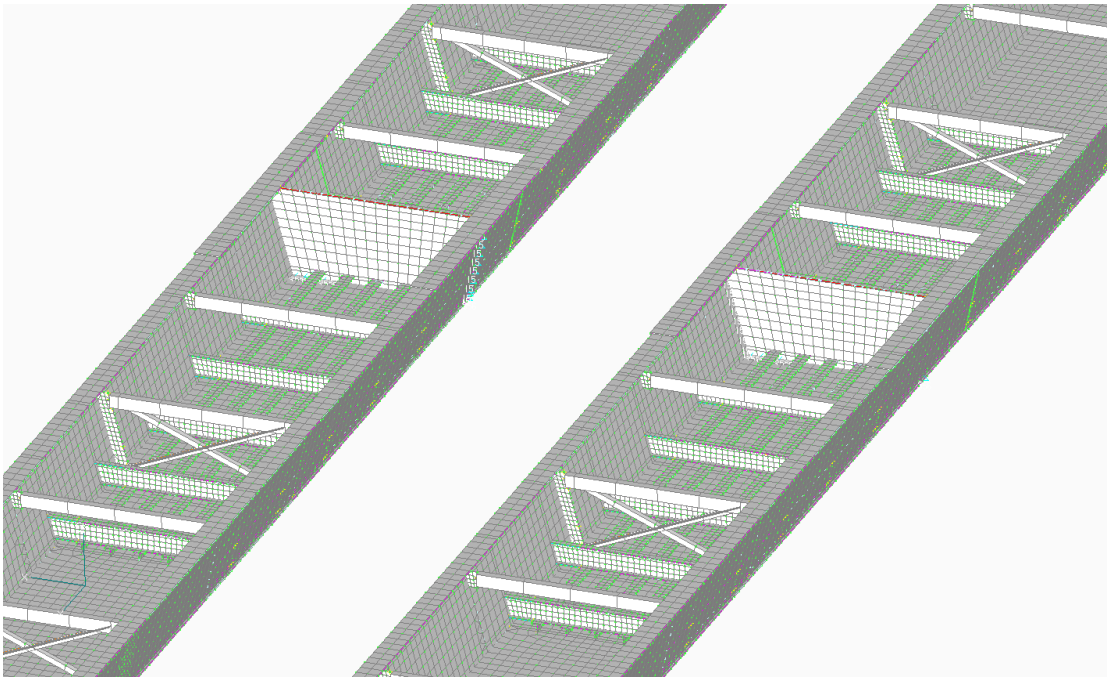

Figure 3.4 View of negative moment region FE mesh in interior of boxes

All of the Type E and Type F diaphragms were modeled in the bridge, as shown in Figure 3.3. The negative moment region, which contained WT sections running longitudinally on the bottom flange and channel sections welded transversely, was modeled with shell elements, as shown in Figure 3.4.

To approximate the effects of the bearings, nodal constraints were defined at the locations of the bearings in the field. The bearings in the field are located near the edge of the boxes, just below the girder webs, and have a typical width of 1.5 to 2.0 ft. To account for this width, 4 or 5 nodes were constrained at each bearing location, depending on the width of the particular bearing. From span 9-11, the bearings were specified as expansion-fixed-expansion-expansion. In the model, the expansion bearings were approximated by allowing longitudinal translation (translation in the y-axis direction in Figure 3.2) and rotation about the x-axis (Figure 3.2) with all other degrees of freedom constrained. The fixed bearings allowed only rotation about the x-axis.

At the piers, full plate diaphragms on the exterior of the boxes connect adjacent girder webs. These exterior diaphragms, which resist the transverse displacement and rotation of the girders relative to each other, were not directly modeled. To approximate the effects of the exterior diaphragms the web nodes at the piers were constrained to restrict transverse translation and rotation (x-axis translation and y-axis rotation in Figure 3.2, respectively). The full plate interior diaphragms at the piers were included in the interior of the box (plate stiffeners were not modeled).

Efforts were made throughout the modeling process to limit the variations between the actual bridge in the field and the modeled structure. In this regard, the differences between field measured data and FE results should have been minimized. However, some simplifications were made to minimize the complexity of the model.

The nominal depth of the concrete slab on the viaduct is 9”; however, it varies from a minimum of 6” on the edge to a maximum of almost 16” at some of the haunches. The slab is tapered such that the depth varies linearly between different points. To simplify the modeling of the deck, four different average thicknesses were used across the width, such that the deck was of constant thickness between the flanges, between the girders, and in the overhangs. The average thicknesses used for Span 10 were 9.75”, 11.25”, 8.875”, and 8.625.”

In the actual bridge, composite action is developed using shear studs welded to the top flange of the box girder. In the model the composite action was modeled by connecting the top flange nodes to the deck nodes via rigid link elements (MPC Beam in ABAQUS). For the top flanges that had a haunch, a node on the top flange was input as the independent node, and nodes on the haunch and deck were input as dependent nodes, shown in Figure 3.5. Using this approach, only one rigid link connected the top flange, haunch, and deck nodes.

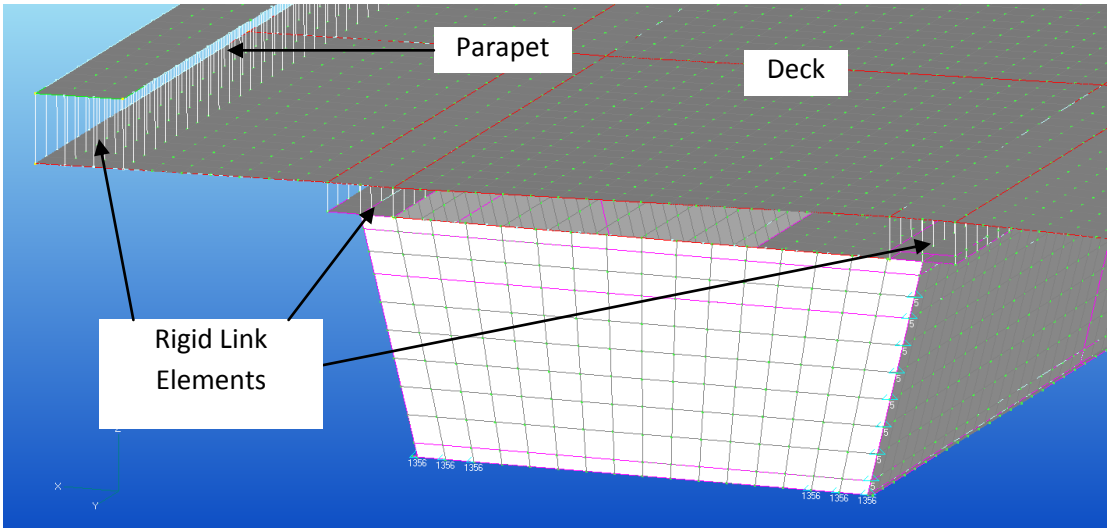

Figure 3.5 FE mesh showing rigid links used to connect top flange, haunch, and parapet to deck nodes.

In the actual bridge the parapet cross section is a complex shape. For the purpose of modeling, the parapet was simplified to a simple rectangular cross section. The width of the model parapet was taken to be the average width of the actual parapet; the parapet height was determined by dividing the cross sectional area by the width. Rigid links were used between the deck and parapet nodes.

In the actual bridge the Type E and Type F internal diaphragms are connected between girder webs with bolts. At all bolted connections, at least two bolts exist and the fixity of the diaphragm members depends on the tightness and location of the bolts. In the model, the internal diaphragms were modeled as fixed, moment resisting connections between the connection plate shell elements and the diaphragm beam elements.

The Modulus of Elasticity for steel was assumed to be 29,000 ksi. The Modulus of Elasticity for concrete was calculated using the equation

$$E = 57000\sqrt{f_c^{'}} \text{ (psi)} \qquad (0.1)$$

in which $f_c^{'}$ is the compressive strength of the concrete in psi. For the design specified compressive strength of 4500 psi, this yields a nominal modulus of the concrete of 3,825 ksi.

A very similar modeling approach was used to model spans 12 to 16 of the viaduct. The only major difference is that it is a five span structure instead of a three span structure. Figure 3.6 shows an interior view of one span of the S15 model.

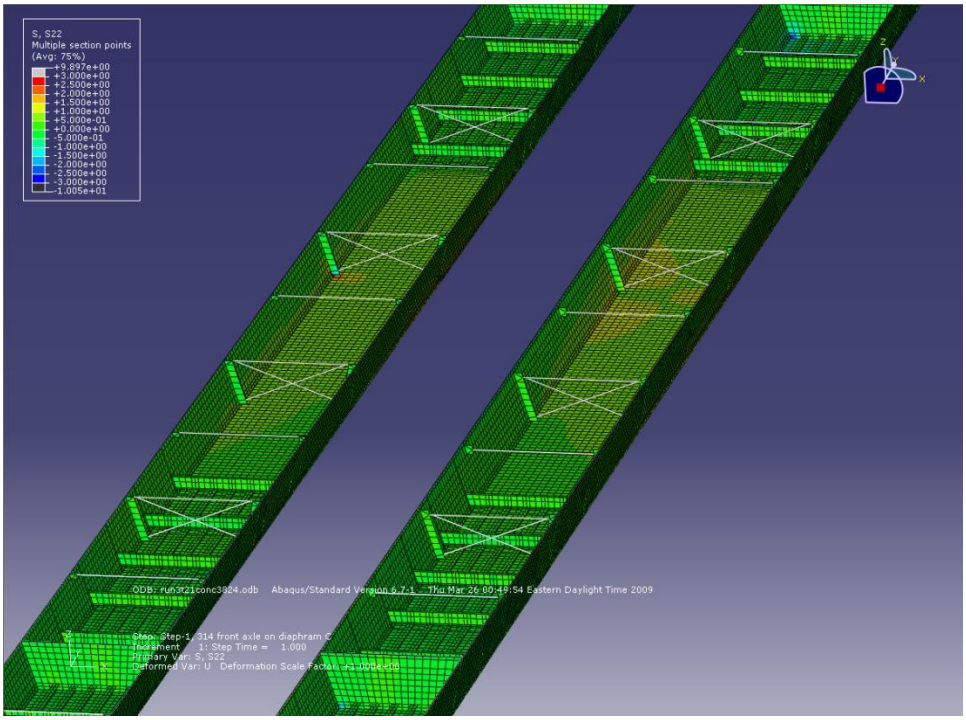

Figure 3.6 View of typical modeled girder interior – spans 12 to 16

The support conditions were again determined from the construction drawings, including bearing type and external diaphragms. The bearing at pier 15 is fixed, and all others are expansion. These were modeled as described earlier for the S10 model.

The thickness of the deck slab for the S15 model was slightly different. It was modeled using three different constant depths: 9”, 9.25” and 11.25”.

The loads applied to the models corresponded to the wheel loads of the trucks used in the field test. The first FE model analyses performed were simulations of the single lane truck passes using Truck #314, corresponding to Pass 1, Pass 3, and Pass 5 (Table 2.3). The wheel loads were applied to the FE mesh through nodal forces on deck elements. During the FE modeling, these wheel loads were the only loads applied to the structure. The dead loads of the structural materials were not considered in FE analyses since the test results captured only the live load effects.

Results of the analysis and comparison to the test results

Using the FE models, the field test runs using a single truck (Truck #314) in each of the travel lanes were simulated. These runs were previously referred to as Pass 1, Pass 3, and Pass 5 in Table 2.3. To simulate the truck passes, the individual wheel loads for Truck #314 were applied as static nodal forces on the deck nodes at the dimensions shown in Figure 2.5. The truck position was varied longitudinally in each travel lane by advancing the truck 2 ft. forward for each FE model trial. These runs were simulated in the FE models to establish the longitudinal location of the truck when the maximum stress was developed in the desired elements. Figures 3.7, 3.8, and 3.9 show the overall deformed shape (exaggerated) of spans 9 through 11 for truck passes 1, 3 and 5, respectively.

To ensure the maximum stresses were captured, the first trial for each travel lane had the front axle of the truck positioned slightly north of the sections of interest (Sections A and C). In the last trial, the rear-most axle of the truck was positioned slightly south of the sections of interest. With a longitudinal variation of 2 ft. for each trial, a total of 13 trials were run for each travel lane (right shoulder, right lane, and left lane for Run 1, Run 3, and Run 5, respectively). Figure 3.7 through Figure 3.9 show typical ABAQUS visualization outputs for Run 1, 3, and 5.

The objective of the FE model was to reproduce the maximum stresses measured during the field test that were presented in Table 2.4. Comparable maximum stresses would indicate agreement between the FE model and the field test results, thereby validating the FE model. The maximum FE model stresses from the longitudinal analysis are shown in Table 3.1 for model S10 and in Table 3.2 for model S15. Presented in the tables are the field test measured stresses, the model predicted maximum stress, and the percent errors – model relative to the field results. In some cases, the field stress was within the accuracy of the measurements (+/- 5 microstrain or 0.15 ksi): for measured stresses below this value, percent error comparisons have not been reported.

In Tables 3.1 and 3.2, the shaded rows represent cross frame members and the non-shaded rows represent bottom flange locations. The large error between field and FE model results for the cross frames (shaded rows) may be a result of a combination of factors. In the field, the strain transducers were placed on the unbolted leg of the angled cross frame members which may see a reduced stress since the strain distribution isn't equal over the cross section of the angle (Yip and Cheng, 2000) (because only one leg of the angle is bolted to the connection plate the strain/stress is not uniform through the entire angle for some distance away from the connection – that distance depends on the size of the member). This effect was not captured in the models because of the way in which the cross frames members were modeled. In addition, the actual transfer of forces between the diaphragm connection plate and the cross frame may be reduced if the connection bolts happen to be loose. Finally, the FE model was created with the cross frames modeled as fully fixed to the diaphragm connection plate. In the field, the cross frames are connected with two bolts on one leg, creating partial fixity. The fixed condition in the model was chosen because the cross frames are primarily axial members. The bending that exists in the members will not likely increase the axial forces because of their low moment of inertia.

Referring to Table 3.1 and focusing on the bottom flange locations (non-shaded rows), the S10 model stresses were generally within -7% to +36% of the field result, with an apparent outlier in Pass 1 (note the field measurement for that sensor is very low, almost within the resolution of the measurement noise for the test). Moreover, the S10 model tends to over-predict the stresses that were measured in the field, indicated by positive percent errors.

Referring to Table 3.2, the range of errors for the modeled prediction of the bottom flange maximum stresses for the S15 model are somewhat larger, ranging from a low of 1% to a high of 42%. Whereas most of the model predicted bottom flanges stresses for the S10 model are higher than the actual measured stresses, some of the stresses for the S15 model are less than the measured values and some of them are greater than the measured stress. The agreement between the model results and the field

test results are very reasonable for an initial model developed from design drawings of a complex structure that did not account for in any way the existing fatigue cracks.

A sensitivity analysis was conducted to determine the sensitivity of the results to changes in the transverse position of the vehicle, modulus of elasticity of the concrete, and the effect of the parapet on the computed stresses.

For the sensitivity to the transverse position of the vehicle, the truck was placed on the bridge in the location that produced the largest stress in the bottom flange. It was then moved transversely in 6" increments, to a location that was between 6" and 36" from the edge of the parapet. This produced only minor changes in the predicted flange stresses. Furthermore, while the results became more accurate in one flange with a move, they became less accurate in the other flange.

For the sensitivity to the modulus of elasticity of the concrete, the concrete strength in the S10 model was varied between 4.5 ksi and 9.0 ksi, which results in a modulus variation of 3825 ksi to 5400 ksi. The results were computed for Passes 7 and 8 (side-by-side truck passes). The bottom flange stresses decrease as the concrete strength (modulus) increases, but only very slightly for the range of concrete strengths considered. Thus the effect of concrete strength was found to be very minimal.

The final modeling effect considered was the effect of the concrete parapet. Analyses were conducted with the parapet included and with the parapet removed. Removing the parapet decreases the stiffness of the bridge, thereby increasing the stresses in the bottom flanges. This trend was observed in both models when the parapet was removed. This in general increased the differences between the model predictions and the measured results for the S10 model. It increased the differences between some of the model prediction and the measured results for the S15 model, but improved the accuracy of some of the other measurements. As there were no clear-cut improvements in the model predictions with these various changes, and the accuracy of the original models were deemed acceptable, the original models were used to conduct the global fatigue evaluation and the retrofit investigations.

Many of the global model results for span 10 can be found in Kucz (2009), and for span 15 in Quigley (2009).

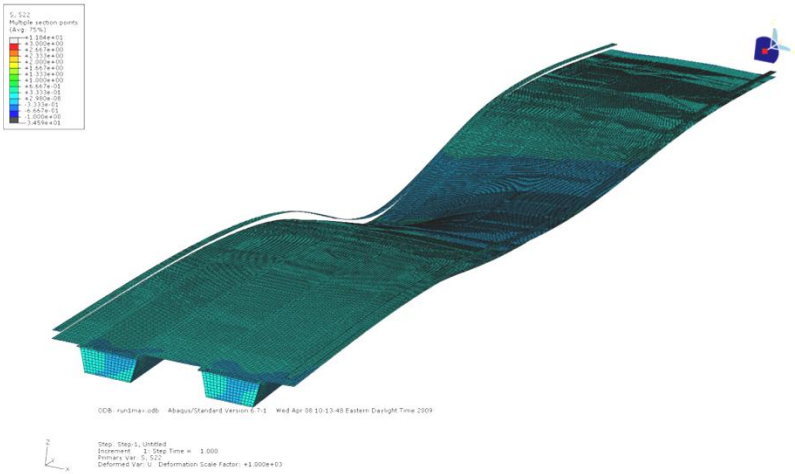

Figure 3.7 FE computed deformed shape span 9-11 for Pass 1 (truck in right shoulder near mid-span of span 10)

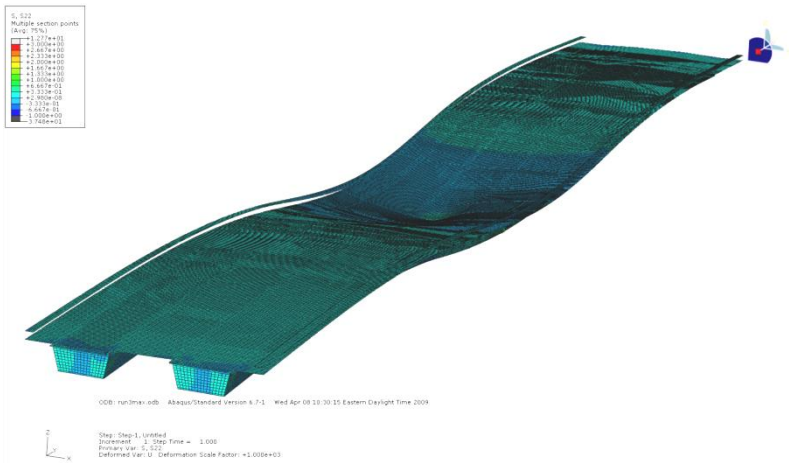

Figure 3.8 FE computed deformed shape span 9-11 for Pass 3 (truck in right lane near mid-span of span 10)

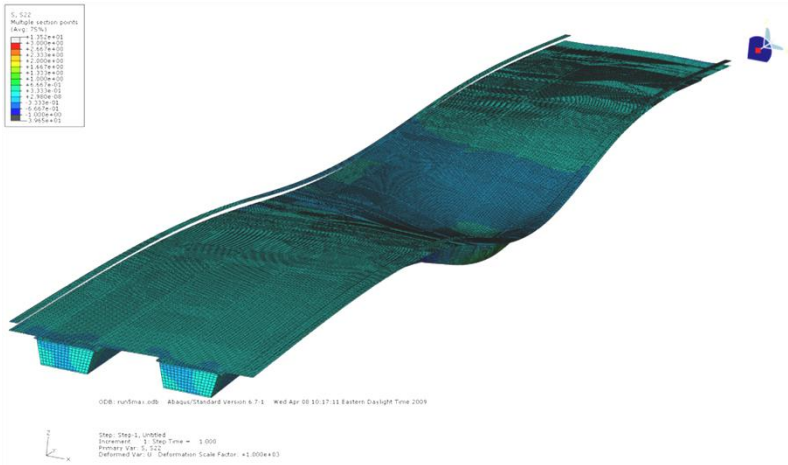

Figure 3.9 FE computed deformed shape span 9-11 for Pass 5 (truck in left lane near mid-span of span 10)

Table 3.1 Comparison of maximum bending stress from field test and S10 model for Pass 1, Pass 3, and Pass 5 (cross frame data shown shaded)

Sec.	Gage	Pass 1			Pass 3			Pass 5		
		Field Test	**Model**	**% Error**	**Field Test**	**Model**	**% Error**	**Field Test**	**Model**	**% Error**
A	292	0.37	0.34	-7%	0.84	0.79	-6%	1.0	1.3	23%
	356	0.18	0.33	78%	0.55	0.59	6%	1.2	1.2	-5%
	B1477	-0.13	-0.52	---	-0.22	-1.2	447%	0.11	0.15	---
	338	0.11	0.49	---	0.17	1.2	575%	-0.08	-0.19	149%
C	317	1.2	1.4	12%	0.57	0.77	36%	0.14	0.43	---
	303	0.86	1.1	22%	1.2	1.2	2%	0.45	0.48	7%
	318	-0.11	-1.4	---	0.11	1.2	994%	0.09	0.80	---
	294	0.37	1.4	275%	-0.38	-1.3	234%	-0.31	-0.88	182%

Table 3.2 Comparison of maximum bending stress from field test and S15 model for Pass 1, Pass 3, and Pass 5 (cross frame data shown shaded)

Sec.	Gage	Pass 1			Pass 3			Pass 5		
		Field Test	**Model**	**% Error**	**Field Test**	**Model**	**% Error**	**Field Test**	**Model**	**% Error**
A	293	0.28	0.40	42	0.51	0.69	35	1.70	1.49	-12
	314	0.52	0.33	-36	1.16	1.03	-11	0.97	1.35	40
	318	-0.25	-0.71	179	-0.39	-1.66	322	0.23	0.98	324
C	356	1.19	1.21	1	1.56	1.23	-21	0.59	0.41	-30

	355	2.11	1.43	-32	1.09	0.74	-32	0.44	0.38	-15
	346	-0.02	2.23	-13154	0.13	-1.71	-1415	0.14	-1.20	-985
	294	0.34	-2.18	-741	-0.13	1.53	-1245	-0.13	1.04	-877

3.3 Local Connection Model

To provide further details of the stress distribution in and around the connection, local 3D finite element models of the Type E diaphragm connection plates were created. Prior to the in-service monitoring, these models were used to gain an understanding of the stress distribution near the web gap and this information was used as the basis for the in-service instrumentation plan described in Chapter 2. Following the field monitoring, the finite element models were used to determine the stresses at the weld toe given that strain gauges could not be directly installed at this location.

The local finite element models were created using a similar process as was used for the global models. First, dimensions for the connection plate were obtained from the construction shop drawings. These dimensions were used to draw 2D surfaces in FEMAP (v.10.1) which were then extruded into their final solid 3D form. Given that we are only interested in the stress distribution near the web gap regions, the local finite element models created are centered about this area exclusively. Next, the models were meshed in FEMAP; varying boundary conditions were imposed and a 1.41 kip representative load was applied to the inside of the connection bolt holes (for a total connection load of 2.82 kips). Finally, the models were converted into an ABAQUS input file and solved.

The type of element used throughout the mesh was a 10-node 3D tetrahedral solid element belonging to the continuum/displacement family of elements known as C3D10 in ABAQUS. This element contains three displacement degrees of freedom, one in each of the X, Y, and Z directions and its output is the 3x3 stress tensor (ABAQUS, 2008). In order to improve the accuracy of the results, full Gaussian Quadrature integration was used throughout the analysis. Two different local models were created because the top and bottom connection plates differ in their bolt hole configuration. While both connections have two 11/16” bolt holes, their locations are not the same relative to the line of action of the cross frame member. It is believed that the bolt hole locations may have an effect on the stresses at the weld toe. Geometric dimensions and bolt holes locations were obtained from the shop drawings. Figure 3.10 illustrates the fabrication drawings used for the Type E diaphragms where geometric differences in the top and bottom connection plates can be seen.

The top connection model consists of 8,999 elements and 18,790 nodes. Given the slope of the web, the bolt hole locations are not the same distance from the web. This fact is significant because the resulting line of action from the cross frame loading does not pass through the centroid of the connection and may cause some additional localized bending. Figure 3.11 shows the top connection model. The bottom connection model consists of 9,092 elements and 18,999 nodes. Unlike the top connection, the line of action of the cross frame loading passes through the centroid of the connection. Figure 3.12 shows the bottom connection model.

The loads applied to the local models were created to replicate the out-of-plane field loading. It is assumed that the forces originate in the cross frames and are transferred to the connection plate via the bolt holes. To reproduce the load path, the local models were loaded on the inside surface of the bolt holes using a distributed load. At first, the resultant magnitude of the distributed load was selected as 1.41 kips, simply to gain an understanding of the stress distribution in the web gap region.

To accurately model the stress distribution in the web gap region the boundary conditions of the model must be chosen appropriately. The possible conditions range from free edges, to fully fixed edges. Since the true conditions are most likely somewhere in between, a study was carried out to determine the effect of varying the support fixity on the web gap stress distribution. In order to capture the full spectrum of possible boundary conditions, three cases were considered: (1) all edges of the models are fixed, (2) the side edges of the model are fixed as well as the top/bottom edge along the flange, and (3) only the top or bottom edge along the flange is fixed, depending on the model being analyzed. Figure 3.13 shows the three boundary condition cases for the top connection model.

The top connection model was also analyzed to more than one loading scenario. Since the line of action of the cross frame does not coincide with the centroid of the top connection it is worth understanding if this has any effect on the resulting web gap stress. Therefore, the top hole of the connection and the bottom hole of the connection were loaded individually, as well as combined. This yielded three loading scenarios and three boundary conditions scenarios for a total of nine cases for the top connection. Given that the line of action of the cross frame coincides with the centroid of the bottom connection, it was not necessary to analyze different loading scenarios for the bottom connection. Table 3.3 summarizes the different loading and boundary condition scenarios analyzed.

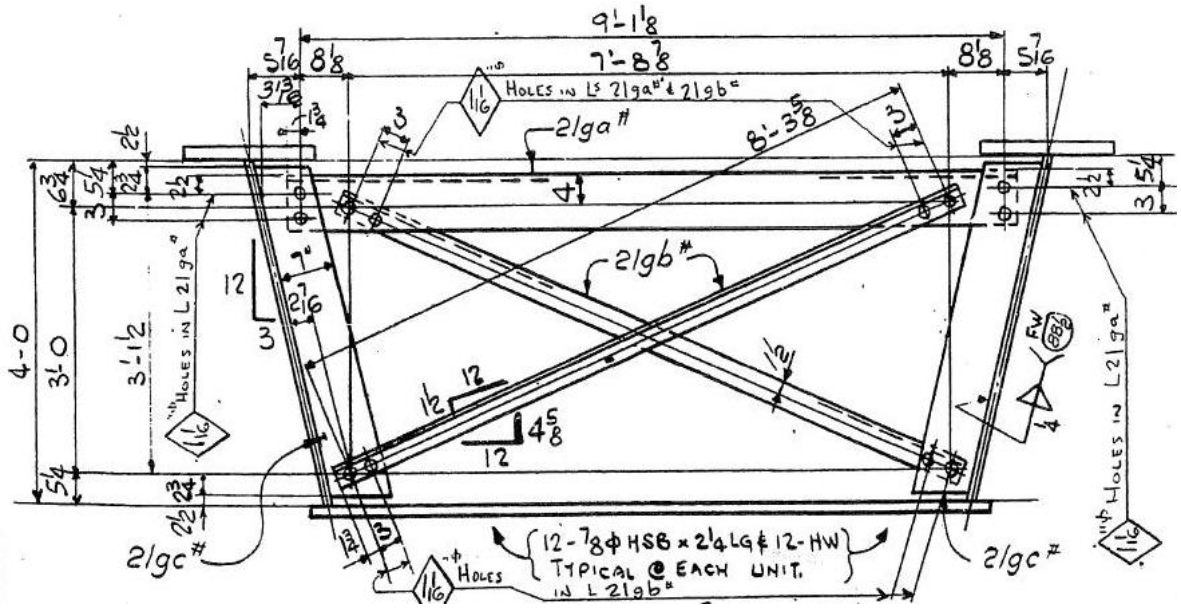

Figure 3.10 Bethlehem Steel fabrication drawings of Type E diaphragms. (Bethlehem Steel, 1974)

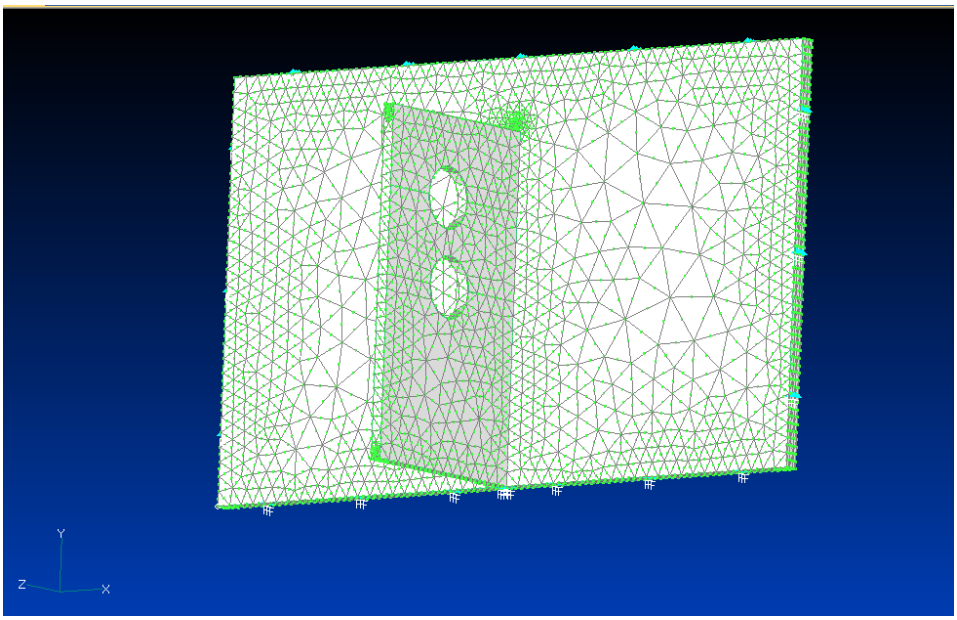

Figure 3.11 Top connection model. Note higher mesh density in web gap region and bolt holes not aligned with the cross frame member.

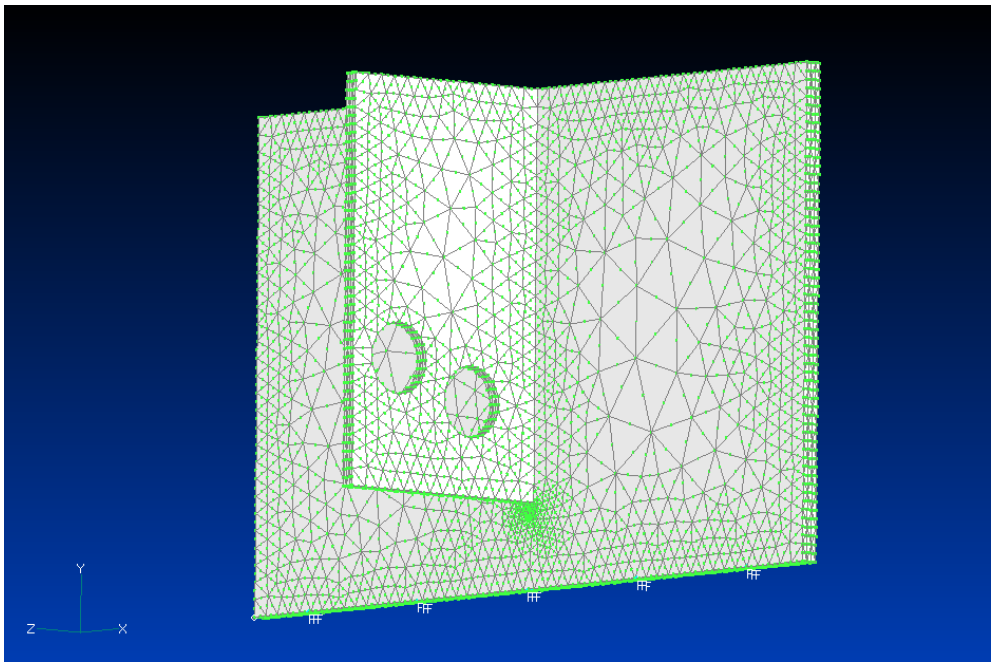

Figure 3.12 Bottom connection model. Note higher mesh density in web gap region and bolt holes aligned with the cross frame member.

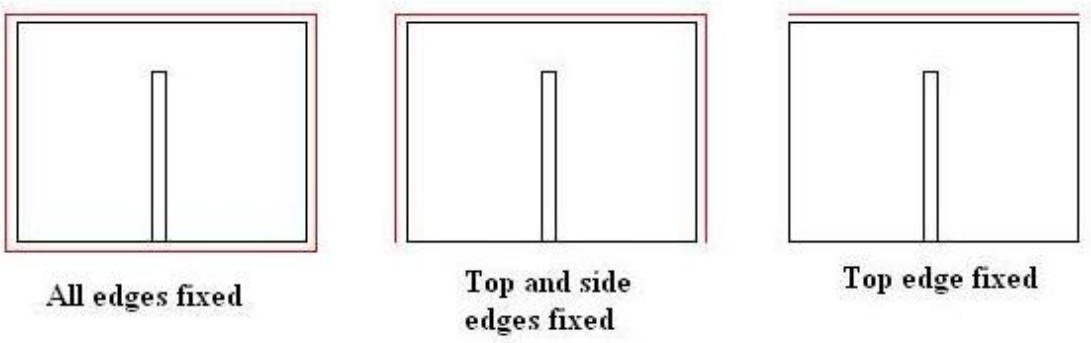

Figure 3.13 Boundary condition cases for the top connection model.

Table 3.3 Summary of loading and boundary condition cases

Model	Loading Conditions	Boundary Conditions
Bottom Connection	Both holes loaded	All edges fixed
		Bottom edge & sides fixed
		Bottom edge fixed
Top Connection	Top hole loaded	All edges fixed
		Top edge & sides fixed
		Top edge fixed
	Bottom hole loaded	All edges fixed
		Top edge & sides fixed
		Top edge fixed
	Both holes loaded	All edges fixed
		Top edge & sides fixed
		Top edge fixed

Local Model Results

The FE results show the presence of a large stress gradient in the web gap region caused by the cross frame forces. This stress gradient was present in all boundary condition cases and all loading scenarios for the top connection model. Moreover, the results show that the stress concentration due to the cross frame forces is highly localized to the web gap region and does not extend longitudinally far from the connection plate along the web of the girder. Sample stress contour plots can be seen in Figure 3.14 to Figure 3.16.

The results of the boundary condition analysis are summarized in Table 3.4. Results are presented for the total load of 2.82 kips on the connection, and then normalized to a 1 kip total load. The choice of boundary conditions significantly affects the stress distribution near the web gap for a given loading. For the bottom connection model, the maximum nodal principal stress at the weld toe decreases as the fixity around the edges increases. It ranges from a high of 13.7 ksi for just the bottom edge fixed, to a

low of 10.8 ksi for all edges fixed. For the top connection model with both holes loaded, the opposite is true, although the variation with different support conditions is not as significant. The maximum principal stress ranges from a low of 10.9 ksi for just the top edge fixed, to a high of 11.3 ksi for all edges fixed. Furthermore, for the same total load, the stresses are in general higher in the bottom connection plate than in the top connection plate.

One conclusion that can be drawn from the local model results is that for the same total load, the maximum stress in the bottom connection is higher than in the top connection. Higher stresses at the bottom connection would inevitably lead to more fatigue cracks at these locations. The 2007 AECOM inspection report crack list confirms this finding; 75% of the cracks detected occurred at the bottom connection detail. The full crack list from the 2007 inspection can be found in Kucz (2009). More of the local model results can be found in Soto Fuentes (2011).

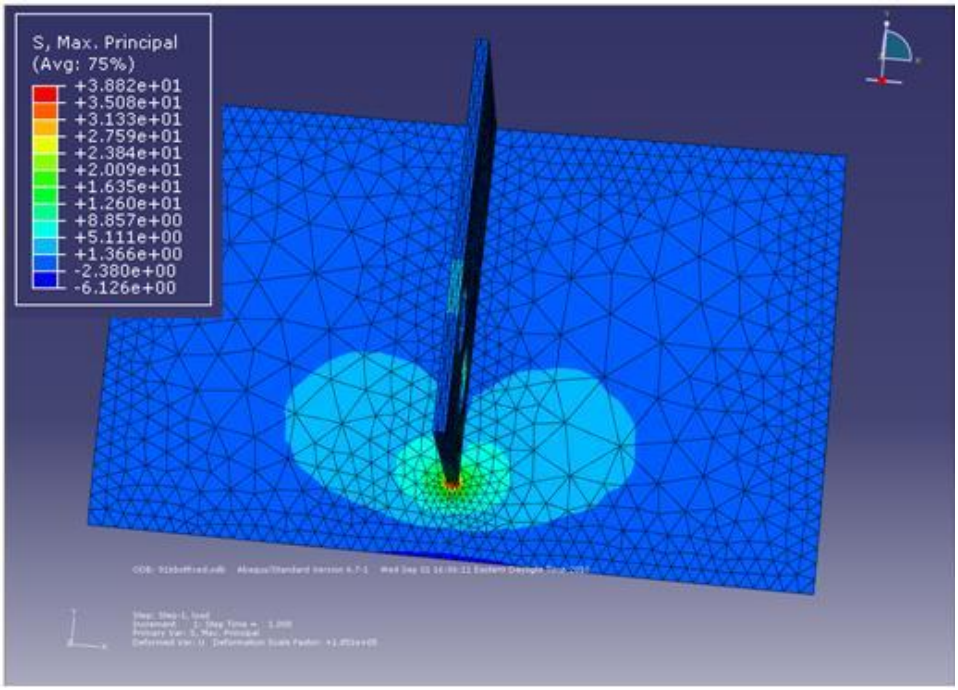

Figure 3.14 Bottom connection, bottom edge only fixed analysis results. Maximum principal stress concentrations are highly localized near web gap region.

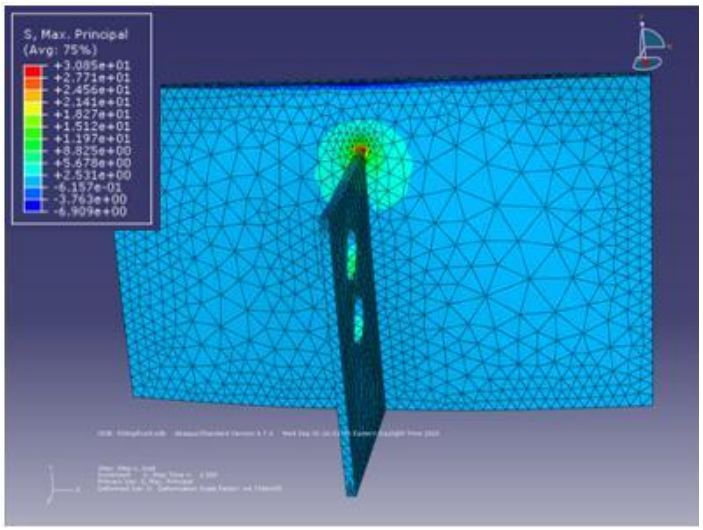

Figure 3.15 Top connection, top edge only fixed. Maximum principal stress concentrations are highly localized near web gap region.

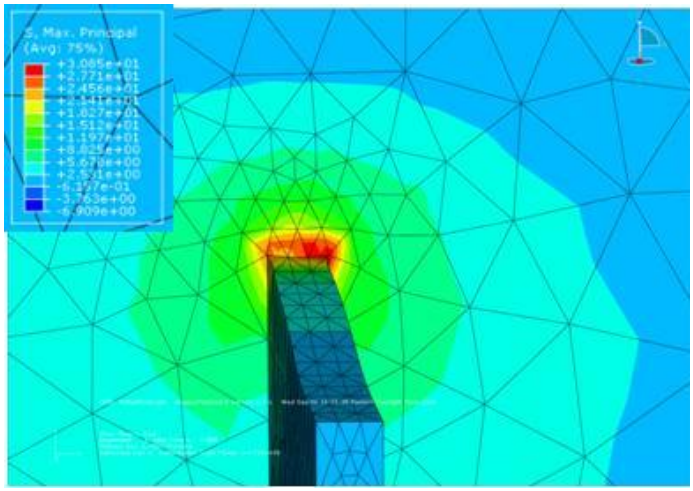

Figure 3.16 Top connection, top edge fixed zoomed in view. Maximum principal stress gradient becomes extreme near weld toe.

Table 3.4 Boundary condition study results (all stresses in ksi)

Bottom Connection Plate				
	2.82 kip load		**Normalized to 1 kip load**	
	Min Principal Stress	**Max Principal Stress**	**Min Principal Stress**	**Max Principal Stress**
Bottom Edge Fixed	-6.12	38.82	-2.16	13.73
Bottom and Sides Fixed	-6.79	34.44	-2.40	12.18
All Edges Fixed	-6.87	30.44	-2.43	10.76
Top Connection Plate (both holes loaded)				
	2.82 kip load		**Normalized to 1 kip load**	
	Min Principal Stress	**Max Principal Stress**	**Min Principal Stress**	**Max Principal Stress**
Top Edge Fixed	-6.91	30.80	-2.44	10.89
Top and Sides Fixed	-6.90	30.80	-2.44	10.89
All Edges Fixed	-6.23	31.90	-2.20	11.28

4 Fatigue Analysis

4.1 Introduction

In this chapter, the FE models and in-service test results are used to conduct a fatigue analysis of the viaduct. The goal of the analysis is to determine if the observed fatigue cracking is consistent with expected behavior given the stress range and traffic loads, to determine if additional fatigue cracking could be expected in the future, and to help guide the retrofit options, which are discussed in Chapter 5.

The analysis was carried in accordance with the AASHTO *Manual for Condition Evaluation and Load and Resistance Factor Rating (LRFR) of Highway Bridges* (referred to here as *Manual*).

4.2 Estimating Remaining Life

Distortion-induced fatigue cracking at unstiffened web gaps has been widely documented to be represented by a Category C Fatigue Detail. In this analysis, the Type E diaphragm web gaps were considered a Category C detail (this was also based on recommendations made by DelDOT and the consultant AECOM). Per *Manual*, the effective stress range at a fatigue prone detail is estimated as:

$$(\Delta f)_{eff} = R_s \Delta f \tag{4.1}$$

in which R_s is the stress range partial load factor, which for estimating mean fatigue life, whether based on analysis or measured stresses, is taken to be equal to 1.0; and Δf is the measured stress range or 0.75 times the calculated stress range (which represents the live load factor for the fatigue limit state and the design truck, as specified by AASHTO LRFD).

Details are only considered to be prone to fatigue if the net live load tensile stress exceeds the dead load compressive stress. Since cracks have been observed in numerous connection details it can be assumed that many of them do experience net tensile stresses due to the live loads.

A detail is said to have infinite fatigue life if

$$(\Delta f)_{\max} \le (\Delta F)_{TH} \tag{4.2}$$

in which $(\Delta f)_{\max}$ is the maximum expected stress range, which can be taken to be equal to 2 times $(\Delta f)_{eff}$, and $(\Delta F)_{TH}$ is the constant amplitude fatigue threshold for the detail, as given in the AASHTO LRFD specification. For a category C detail, $(\Delta F)_{TH} = 10\,ksi$.

If equation (4.2) is not satisfied, then the detail has a finite fatigue life. The total fatigue life of a detail, in years, is given by

$$Y_f = \frac{R_R A}{365 n \left(ADTT\right)_{SL} \left(\left(\Delta f\right)_{eff}\right)^3} \tag{4.3}$$

in which

Y_f = finite fatigue life in years

R_R = resistance factor that depends on the category detail and if the calculation is to be done for minimum, evaluation, or mean fatigue life

$ADTT_{SL}$ = lifetime average daily truck traffic in a single lane

n = number of stress cycles per truck

A = category detail constant

$\left(\Delta f\right)_{eff}$ = effective stress range

For a Category C detail and mean fatigue life, R_R =1.3; $A = 44 \times 10^8$ (AASHTO LRFD). The test results (Chapter 2) showed that the details experience one cycle for each passage of the truck; therefore, $n = 1$. Substituting these values into (4.3) and simplifying yields

$$Y_f = \frac{1.3 \times 44 \times 10^8}{365 \left(ADTT\right)_{SL} \left(\left(\Delta f\right)_{eff}\right)^3} = \frac{1.567 \times 10^7}{\left(ADTT\right)_{SL} \left(\left(\Delta f\right)_{eff}\right)^3} \tag{4.4}$$

To estimate the fatigue life it remains to determine the stress range and the $ADTT_{SL}$ (otherwise referred to as the lifetime average daily truck traffic). The effective stress range can be estimated using FE models, or from in-service measurements of the actual strains. The $ADTT_{SL}$ can be estimated from traffic count data provided by DelDOT, or also from the in-service measurements of the actual strains. Estimates of the fatigue life were first made based on the results of the S10 model and ADT data provided by DelDOT. Later, after the in-service monitoring was completed, estimates were made using the field data in conjunction with the local FE connection model. The results of the two processes are discussed below.

4.3 Global model estimate

Lifetime Average Daily Truck Traffic

The first step to determining the lifetime $ADTT_{SL}$ is to determine the present day average daily truck traffic ($ADTT_{PR}$) from data provided by the bridge owner. For the Newport Viaduct, DelDOT provided an ADT estimate of 69,412 (northbound and southbound directions) for 2007, with 9% truck traffic. The $ADTT$ for both directions was therefore 6,247 in 2007. Assuming an equal distribution of trucks in both directions (northbound and southbound), the $ADTT$ for each direction was 3,124.

The AASHTO *Manual* provides a graph for estimating the lifetime average daily truck traffic based on the $ADTT_{PR}$, age of the bridge, and an assumed exponential growth rate. It yields an estimate for $ADTT_{SL}$ based on its prior years in service, and a 30 year projection into the future. For this study, the goal was to determine if the models would predict that cracking would occur in the time from when the bridge first open until 2005 when the cracks were first discovered. Because the *Manual* graph projects growth 30 years into the future, the $ADTT_{SL}$ would be too conservative (i.e., provides a much higher $ADTT_{SL}$). For this analysis the average lifetime traffic was estimated for the time the bridge was placed in service (1978) to the time that the cracks were first discovered (2005), 28 years. Therefore, the 2007 $ADTT_{PR}$ was used to back project to 1978 what the $ADTT$ would have been every year assuming a 4% exponential growth. This yields, for example, an $ADTT$ of 1002 in 1978. Averaging the results over the 28 years yields an average $ADTT$ of 1788. For a single lane, per AASHTO LRFD,

$$ADTT_{SL} = p \times ADTT \tag{4.5}$$

in which p is the fraction of trucks in a single lane; for a 2 lane road $p = 0.85$, therefore the lifetime average daily truck traffic between 1978 and 2005, for a single lane is $ADTT_{SL} = 0.85 \times 1788 = 1519$.

Substituting into (4.4) and simplifying yields

$$Y_f = \frac{1.567 \times 10^7}{1519\left((\Delta f)_{eff}\right)^3} = \frac{10316}{\left((\Delta f)_{eff}\right)^3} \tag{4.6}$$

Equation (4.6), which is plotted in Figure 4.1, shows that the fatigue life decreases rapidly for stresses between about 4.0 and 6.0 ksi, and then decays much more slowly for stresses above 6.0 ksi. A line is drawn which shows the age of the viaduct when the cracks were first discovered in 2005; the corresponding stress for that fatigue life is 7.15 ksi.

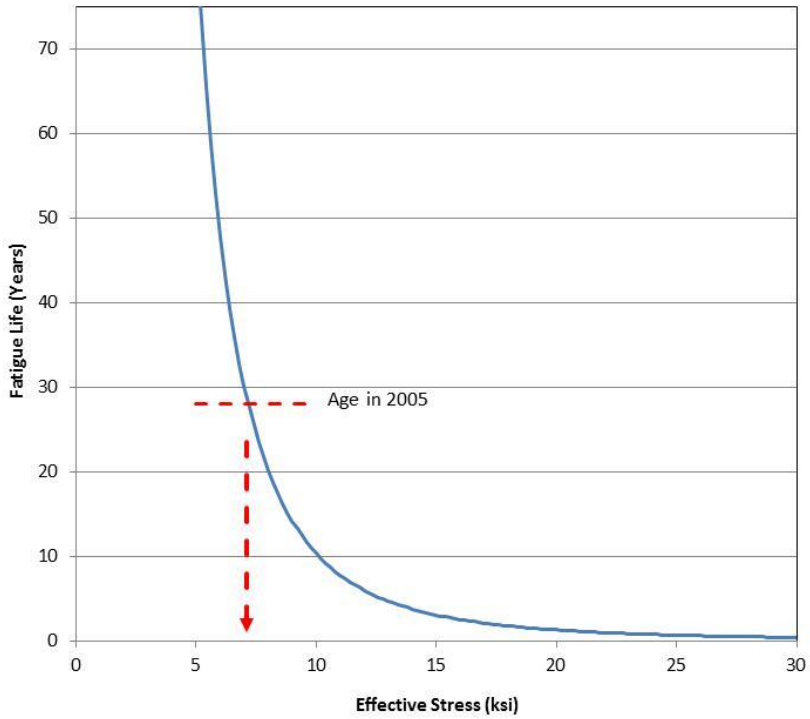

Figure 4.1 Equation (4.5): Mean Fatigue Life versus Effective Stress

Effective Stress Range

The effective stress range at the connections was estimated using both the global and local FE models. Assumptions have to be made when using the global model to estimate the stress range in the connection because the resolution of the mesh in the connection region is not small enough to capture it accurately.

When field testing has been used to capture the stress range for fatigue life calculations, a range of different instrumentation techniques have been used. A series of small strain gages have been employed within the web gap "hot spot" region to capture a range of stresses. Using the measured data, stresses were interpolated between gages and extrapolated linearly beyond the instrumented web gap region to the weld toe to determine a maximum stress range. Connor and Fisher (2006) suggested the installation of strip-type gages that produce a strain gradient within the gage length. That gradient is extrapolated linearly to determine a maximum stress range at the weld toe in the web gap. Regardless of the instrumentation, extrapolation beyond the instrumented region is required because the physical size of the strain gages and the weld toe geometry does not permit direct measurement at the weld toe. Connor and Fisher (2006) suggest that the measurements of stress range in the web gap be taken no closer than 0.12 in. (3mm) from the weld toe; Fisher et al. (1987) took measurements within the web gap at a distance of 0.5 in. from the weld toe. These upper and lower limits define the distance from the weld toe that the stress range should be measured within the web gap region.

In cases in which FE modeling was used to predict stress ranges for distortion-induced fatigue, a refined mesh at the detail of interest was required to produce an accurate FE model approximation of stress (Roddis and Zhao, 2003; Jajich and Schultz, 2003). In the past, the mesh refinement was limited due to computational resources. Advances in computing capacity and commercially available FE software has enabled the refined mesh to be comprised of element sizes much smaller relative to the past. Roddis and Zhao (2003) noted that as mesh density increases, infinitely large stresses are predicted by FE approximations. They chose to select a lower bound mesh size of 0.16 in. (4.25mm) within the web gap region. Jajich and Schultz (2003) confirmed that distortion-induced fatigue stresses in the web gap "hot spot" region were mesh-dependent and attenuated rapidly; however, they relied on correlation to field results to determine their stress range and thus avoided selecting an overly dense mesh.

Hobbacher (2009) described a method to quantify the "hot spot" stress that should be used in conjunction with fatigue life calculations. In the method, FE model stress approximations are plotted as a function of the distance from the weld toe. Typically the stresses become infinite as the distance from the weld to decreases, consistent with Roddis and Zhao (2003) and Jajich and Schultz (2003). To account for the asymptotic FE stresses, Hobbacher (2009) suggests a linear extrapolation to the weld toe using FE stress approximations at a distance of 0.4t and 1.0t from the weld toe, where t is the thickness of the welded attachment. The linear extrapolation avoids using an artificially high stress range with small mesh sizes and an artificially low stress range with elemental approximations far from the weld toe.

In summary, Connor and Fisher (2006) established a lower bound field instrumentation position of 0.12 in from the weld toe. In FE model studies, Roddis and Zhao employed a lower bound FE mesh size of 0.16 in. to capture the stress range. Hobbacher (2009) used a linear extrapolation of the FE approximations to capture a stress range at the "hot spot" location. In the fatigue analysis of the Newport Viaduct, a range of the aforementioned methods were used to capture the stress range at the Type E diaphragm web gap locations from the global span 10 model. The FE model was refined to element sizes of 0.1 in. that represented the lower bound distance established by Connor and Fisher (2006). The mesh size employed by Roddis and Zhao fell within this range. The stress ranges used for fatigue life calculations were determined using 3 locations/methods: the FE approximation at an element location represented by Connor and Fisher (2006) as a lower bound gage measurement position (0.16 in. from weld toe), the FE approximation at an element location represented by Fisher et al. (2006) as an upper bound gage measurement position (0.5 in. from weld toe), and the linear extrapolation of the FE approximations described by Hobbacher (2009).

Since shell elements were used in the S10 model, out of plane stresses from the web elements were not available. As an alternative, normal stresses in the connection plate perpendicular to the girder web (x-direction) were used, as shown in Figure 4.2.

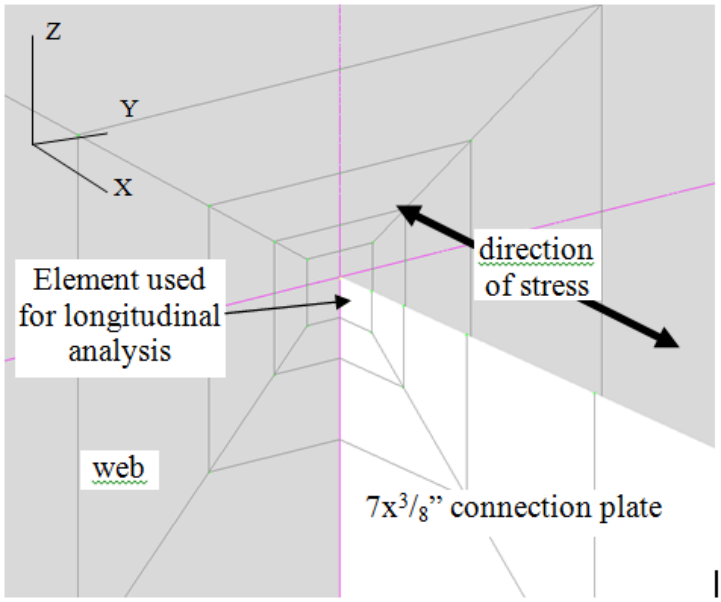

Figure 4.2 Direction of stress taken from global S10 model for fatigue evaluation

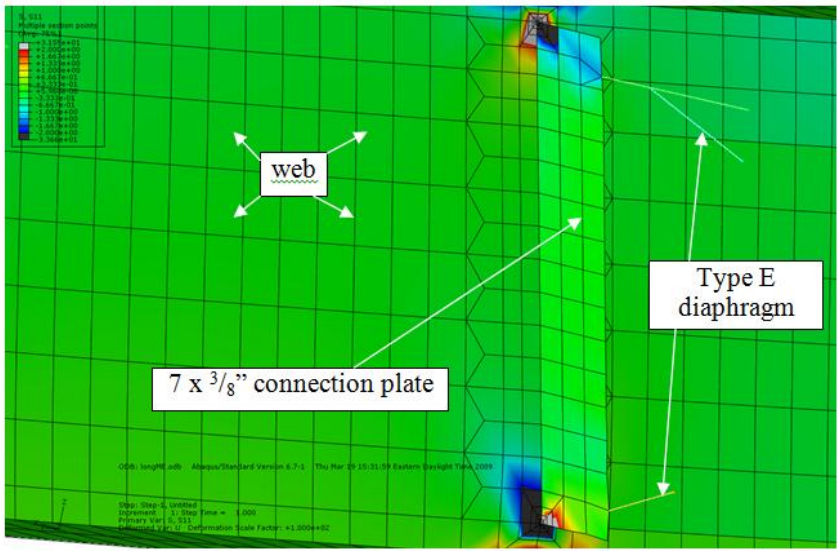

Figure 4.3 Typical contour plot of stresses in web and connection plate

A typical contour plot of the stresses in the web and connection plate for the S10 model is shown in Figure 4.3. Table 4.1 shows the stress ranges obtained from the S10 model for all eight connections for the three different methods. The stresses obtained a distance of 0.14 in. from the weld toe, and using the linear interpolation from a bit further away (the Hobbacher (2009) method) are very comparable. The stress range taken a distance of 0.56 in. from the weld toe is about half that of the other two methods. Note also that half of the connections report a compressive stress range and the other half a tensile stress range. Looking carefully at the deformed shape of the girder for the vehicle in different positions, when the connection is in compression the girder web is deformed in such a way that the

outside face of the web would be in tension. While this location is not near the weld toe, and the inspection did not reveal any initiation of cracks on the outside face of the web, the fatigue life was calculated anyway for these areas, assuming the stress was tensile and not compressive.

Table 4.1 Stress range from global S10 model at all eight connections

Method		Distance from weld toe (in)	Fatigue Detail Location							
			A	B	C	D	E	F	G	H
1	Connor and Fisher (2006)	0.14	12.1	-20.0	-14.5	18.8	-11.9	19.0	15.4	-20.2
2	Fisher *et al.* (1987)	0.56	6.0	-7.2	-7.3	6.9	-5.9	7.0	7.7	-7.2
3	Hobbacher (2009)	Linear extrapolation	11.8	-17.5	-14.2	16.5	-11.7	16.7	15.1	-17.6

Using the effective stresses in Table 4.1, the fatigue life of the connections was calculated and are listed in Table 4.2. As one would expect, since the stresses are comparable, the estimates based on the effective stress using the Connor and Fisher (2006) recommendation and the Hobbacher (2009) recommendation are very similar. They range from under 1 year to 3 years. The estimates based on the stresses obtained using the Fisher et al (1987) recommendation are much greater, and range from a low of 10 years to a high of just under 23 years.

Table 4.2 Estimated fatigue life of the eight connections

Method		Distance from weld toe (in)	Fatigue Detail Location							
			A	B	C	D	E	F	G	H
1	Connor and Fisher (2006)	0.14	6	1	3	2	6	1	3	1
2	Fisher *et al.* (1987)	0.56	47	28	27	32	49	30	22	27
3	Hobbacher (2009)	Linear extrapolation	6	2	4	2	6	2	3	2

The fatigue life predicted by Method 1 and 3 appear lower than expected given the condition of the fatigue cracks observed on the structure in interior box inspections. Specifically, the actual fatigue cracks within the structure have been observed as actively propagating. Furthermore, a low percentage of cracks (approximately 15% or less) have observable oxidation from being exposed to atmospheric conditions over a long period of time. If the cracks had formed when predicted by Method 1 and 3, the following situations would be expected: (1) all of the web gap regions would have been observed as cracked in interior box inspections, (2) noticeable rust would be expected on unprotected, cracked surfaces on a high percentage of cracked locations, and (3) cracked locations would have propagated to some equilibrium or irreversible damage state in the time since cracking was predicted to occur. The

observed state of the fatigue cracks on the structure does not coincide with these expectations, and in contrast some cracked locations have initiated since the first interior inspection in 2006.

The calculation of accumulated stress cycles and LADTT was based on fatigue cracking occurring in 2005 when the structure had an in-service life of 28 years. The expected fatigue life of the details calculated in Method 2 is consistent with the assumption that the fatigue cracking has occurred around 2005. Detail locations A and E have higher predicted fatigue lives, but detail locations B, C, D, F, G, and H have calculated fatigue lives within or around the range of 28 years. The pattern of predicted fatigue cracking loosely matches the actual pattern of fatigue cracking in the structure. In the structure, location B, C, E, and H are typically cracked. With the exception of detail location E, these locations are predicted to crack around 2005 by Method 2.

4.4 Local Model – Field Testing Estimate

Effective Stress Range

Ideally, the strain directly adjacent to the weld toe would have been measured in the field tests; however, the tight constraints prohibited mounting a gage that close to the weld toe. Instead, a strain gage was mounted a short distance from the weld toe. The local FE model was then used to determine the ratio of the stress at the weld toe and the stress at the gage location. By multiplying the measured stress by this ratio the stress at the weld toe was estimated.

To determine the scaling factor, the foil gage location from the in-service monitoring was superimposed on the bottom connection finite element model. The finite element model was loaded using a 1.4142 kip load perpendicular to the girder web which corresponded to an out of plane force transferred from the cross frames (the magnitude of the applied force used is immaterial since the result of the analysis is simply a ratio of stresses). Longitudinal stresses from the bending of the entire girder were not included in the analysis as it has been reported that their effects are “much smaller than the local out of plane bending stresses” (Connor and Fisher, 2006). Next, the model was analyzed with varying boundary conditions and the nodal output was recorded at the superimposed gage location and corresponding maximum at the weld toe. Once the stresses at the gage location and weld toe were known, a scaling factor was determined for each boundary condition case analyzed. This scaling factor allowed the extrapolation of the stresses from the gage location to the weld toe. Figure 4.1 below shows the location of the superimposed foil gage on the bottom connection model.

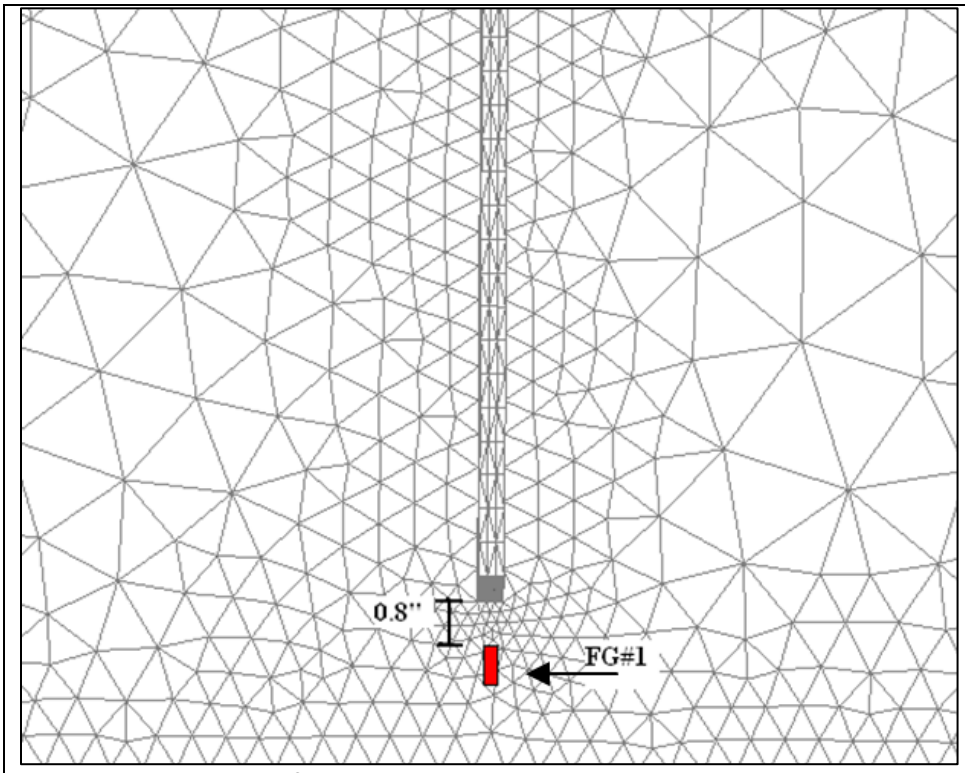

Figure 4.4 Foil gage #1 field location superimposed on localized bottom connection model web gap

The finite element analysis results show that a very high stress gradient exists in the web gap region. However, the foil gage installed in the web gap region only provides a single strain output obtained by integrating strains over its entire length. To obtain a single strain value corresponding to the foil gage, the output at three nodal points along the superimposed length of the foil gage were recorded and averaged. The three nodal locations used corresponded to the top, middle and bottom of the superimposed foil gage. Similarly to the boundary condition study carried out in Chapter 3 (see Table 3.4), scaling factors were determined for three sets of boundary conditions. The output of interest was the vertical or Y-component of the maximum principal stress. Table 4.3 on the next page, summarizes the σ_y stress output at the superimposed foil gage location and corresponding weld toe maximum stress.

Table 4.3 Stress at superimposed foil gage location and corresponding weld toe maximum stress, for varying boundary conditions

	All fixed	**Bottom & Sides Fixed**	**Bottom Fixed**
Superimposed FG#1 Location (ksi)	2.40	2.12	1.77
σ_y at weld toe (ksi)	25.11	28.57	32.45
Scaling Factor	10.46	13.48	18.33

Given a variable amplitude loading in histogram form, Miner's rule is used to calculate an "effective" stress, which is given by

$$S_r = \left(\sum_{i=1}^{k} f_i S_i^{\,3} \right)^{1/3} \tag{4.7}$$

in which S_i is the bin mid-width stress and f_i is the fraction of cycles in that range.

Vehicles weighing less than 20 kips have a very low probability of causing fatigue damage (Alampalli, 2006), thus, it becomes necessary to establish a minimum stress level for use in equation (4.7). The goal is to eliminate those cycles that are not causing fatigue damage. Connor and Fisher (Connor and Fisher, 2006) and Zhou (Zhou, 2006) proposed using cutoff values, or minimum stresses, of 0.25CAFT and 0.50CAFT respectively. Given a constant amplitude fatigue threshold of 10.0 ksi for a Category C detail, these proposed cutoff points would be 2.5 ksi and 5.0 ksi.

Difficulties arise when attempting to use a single factor of the CAFT as the cutoff value to calculate the effective stress. Given the different scaling factors that arise from the various boundary conditions analyzed, it is unclear which single value of stress at the weld toe is the most accurate. In other words, the choice of boundary conditions significantly affects the magnitude of the stress at the weld toe thus making it impossible to use a single CAFT factor as the cutoff point. For this reason, it became necessary to calculate the effective stress for all boundary condition cases and their corresponding scaling factors. Instead of using a single factor of the CAFT as the effective stress cutoff value, the mid-width value of bins 2-7 of the Rainflow histogram (Table 3.3) was used. Table 4.3 on the next page summarizes the effective stress calculation results.

Given the large variability in the calculated effective stresses at the weld toe, mean fatigue life was calculated for each effective stress corresponding to the various boundary conditions.

Table 4.4 Effective Stress at weld toe for different cut-off (minimum) stresses

Bin	Mε	Cut-off mid- bin stress σ_{MB} (ksi)	Total # of Cycles	Cut-off stress at weld toe (ksi)			Effective Stress at weld toe (ksi)			
				All fixed (10.46* σ_{MB})	Bottom & Sides Fixed (13.48* σ_{MB})	Bottom Fixed (18.33* σ_{MB})	All fixed	Bottom & Sides Fixed	Bottom Fixed	Average
2	5-10	0.22	1,546,673	2.28	2.93	3.99	3.54	4.56	6.21	4.77
3	10-15	0.36	304,556	3.79	4.88	6.64	5.62	7.24	9.85	7.57
4	15-20	0.51	102,143	5.31	6.84	9.30	7.50	9.66	13.14	10.10
5	20-25	0.65	42,758	6.83	8.79	11.96	9.28	11.95	16.30	12.51
6	25-30	0.80	20,309	8.34	10.74	14.62	11.00	14.17	19.28	14.82
7	30-35	0.94	10,608	9.86	12.70	17.28	12.65	16.28	22.16	17.03

Lifetime Average Daily Truck Traffic

Instead of using the present day $ADTT_{PR}$ estimate provided by DelDOT to determine the $ADTT_{SL}$ as before, this analysis is based on the actual number of cycles recorded during the in-service monitoring. These numbers are believed to be a better representation of the number of load cycles experienced by the web gap detail as opposed to the bridge structure as a whole. The number of cycles for bins 2-7 (Table 4.4) was divided by 23, the length in days of the in-service monitoring period, to obtain an average daily "truck" traffic count for 2011. As before, this present day $ADTT_{PR}$ was then used to back project what the $ADTT$ was for every year the bridge was in service assuming a 4% exponential growth rate. The $ADTT_{SL}$ was then calculated as the average of those results between the time the bridge was placed in service (1978), until the time the cracks were first discovered (2005). Table 4.4 shows a sample of the estimated yearly $ADTT$ and the $ADTT_{SL}$ from 1978 to 2005.

Table 4.5 $ADTT_{SL}$ estimates with 4% exponential growth rate.

Year	Average Daily Truck Traffic (ADTT)					
	Bin 2	**Bin 3**	**Bin 4**	**Bin 5**	**Bin 6**	**Bin 7**
2011	67,247	13,242	4,441	1,859	883	461
2010	64,661	12,733	4,270	1,788	849	443
2009	62,174	12,243	4,106	1,719	816	426
2008	59,782	11,772	3,948	1,653	785	410
2007	57,483	11,319	3,796	1,589	755	394
2006	55,272	10,884	3,650	1,528	726	379
2005	53,146	10,465	3,510	1,469	698	364
…	…	…	…	…	…	…
1979	19,169	3,775	1,266	530	252	131
1978	18,432	3,630	1,217	510	242	126
1978 to 2005 $ADTT_{SL}$	32,893	6477	2172	909	432	225

The $ADTT_{SL}$ estimates shown in Table 4.5 vary greatly. The values range from 32,893 for Bin 2 to 225 for Bin 7. These extreme values are not realistic representations of the actual $ADTT_{SL}$ of the structure, but are presented herein for completeness. Comparing the lifetime average estimates and the 2007 values, to the ADTT provided by DelDOT and the $ADTT_{SL}$ calculated earlier from that value, it appears that the results based on the bins 3, 4 and 5 seem to be the most realistic and reasonable. Note also that when calculating the fatigue life the lane reduction factor (0.85) is not included since the number of cycles is based on the actual measured strain at the connection, thus, any reduction it automatically captured by the measured data.

The fatigue life was calculated for all boundary condition cases and all cut-off stress values. The results are presented in Table 4.6. The predictions ranges from a low of 2 years to a high of 34 years. As mentioned previously, some of the results can be excluded simply based on the very low or very high $ADTT_{SL}$. This would be the case for bins 2, 6, and 7. The estimates for the "bottom fixed" boundary condition case are all very low and can be discounted for the following reasons: (1) the results imply the first cracks would have formed shortly after the bridge opened, i.e., in the 1980s. Had the fatigue cracks formed in the 1980s, the in-depth inspection in 2005 would have discovered extensive corrosion at the cracked locations and this was not the case. (2) the "bottom only fixed" boundary condition assumption was clearly a lower bound case for the model; the other three edges are not free, but are constrained in some manner. Fixing the bottom edge of the model and allowing all other edges to rotate/displace freely does not approximate the true field conditions and leads to fatigue life estimates that are too low. Eliminating these cases, and also those for bin 2, 6, and 7, yields the final results which are shown in Table 4.7.

Table 4.6 Fatigue life results

Bin	Total # of Cycles	2011 $ADTT$	1978 to 2005 $ADTT_{SL}$	Weld toe Effective Stress (ksi)			Mean Fatigue Life (years)			
				All fixed	Bottom & Sides fixed	Bottom fixed	All fixed	Bottom & Sides fixed	Bottom fixed	Average
2	1,546,673	67,247	32893	3.54	4.56	6.21	10.7	5.0	2.0	5.9
3	304,556	13,242	6477	5.62	7.24	9.85	13.6	6.4	2.5	7.5
4	102,143	4,441	2172	7.5	9.66	13.14	17.1	8.0	3.2	9.4
5	42,758	1,859	909	9.28	11.95	16.3	21.6	10.1	4.0	11.9
6	20,309	883	432	11	14.17	19.28	27.3	12.8	5.1	15.0
7	10,608	461	225	12.65	16.28	22.16	34.3	16.1	6.4	18.9

Table 4.7 Fatigue life results

Bin	Total # of Cycles	2011 $ADTT$	1978 to 2005 $ADTT_{SL}$	Weld toe Effective Stress (ksi)			Mean Fatigue Life (years)		
				All fixed	Bottom & Sides fixed	Bottom fixed	All fixed	Bottom & Sides fixed	Average
3	304,556	13,242	6477	5.62	7.24	9.85	13.6	6.4	10.0
4	102,143	4,441	2172	7.5	9.66	13.14	17.1	8.0	12.6
5	42,758	1,859	909	9.28	11.95	16.3	21.6	10.1	15.8

5 Retrofit Options

5.1 Introduction

After reviewing the various methods used to retrofit details prone to distortion induced fatigue cracking, three options were selected for analysis through refined finite element modeling. Span 15 exhibited only minimal cracking and span 10 had significant cracking; therefore, it was decided to perform the retrofit analysis using the model for span 10 (details and model information for span 10 were discussed in Chapter 3). To determine the effectiveness of each retrofit, the mesh was refined at the boundaries between the connection plates and the webs for each web gap. Each model was then loaded with a fatigue truck and local stresses from the model with the refined mesh were recorded. These local stresses were then used in fatigue life calculations.

5.2 Retrofit Options

Three different retrofit options were investigated for the project: (1) positive attachment between the connection plate and the girder flanges, (2) lengthening of the web gaps by creating a slot between the connection plate and web at both the top and bottom of the connection plates, and (3) removal of the diagonal members in diaphragm type E. Each is described in more detail below.

Positive Attachment

To create positive attachment, Fisher and Keating (1989) recommend using plates with a minimum thickness of 3/4 in and to avoid field welding if possible. The ideal positive attachment retrofit would therefore be bolted to both the connection plate and the flanges. To create such an attachment, either a WT section or angle is needed. For this study, a WT section was chosen so that it could be bolted to the flange on both sides of the connection plate.

In order to get a section with a stem deep enough to allow for the recommended 4 high strength bolts per shear plane, a minimum depth of 12 in. was selected. The lightest section to satisfy this criteria and also has a stem thickness of at least 3/4 in. is a WT 12 x 88. This has a flange width of 12-7/8 in. which should be sufficient to allow for 2 bolts on each side of the connection plate. It has a thickness of 1.34 in. which exceeds the minimum specified by Fisher, but is thin enough to fit in the gap between the plate and the flange. Although the sloped web of the girder would require a specially cut section, it was modeled as adjacent to the web and flanges as described later on. A sketch of the attachment is shown in Figure 5.1.

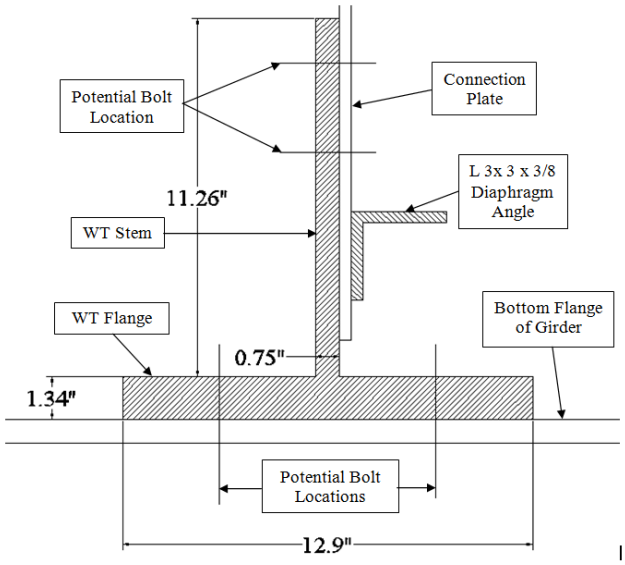

Figure 5.1 Sketch of WT to Bottom Flange Connection

Bolting a WT section to the top flange would be difficult and costly, due to concrete on top of the flange; however, it was still included in the options for analysis. A simpler more constructable option was explored for the top connection that consists of a 3/4 in. steel plate that is bolted to the connection plate and welded to the top flange. Although this is not the most desirable connection type, field conditions may make it the most feasible and therefore its effectiveness was investigated. Additional considerations for the fatigue life of the weld would need to be studied if this option were to be adopted.

Slot Retrofit

To effectively reduce stress concentrations in the web gap without using additional steel, gaps must be created of sufficient length. Fisher recommends a minimum slot increase of 300 mm (11.81 in). Since there is no recommended minimum slot thickness, a 1/4 in. cut was made to provide space between the connection plate and web without significantly reducing the amount of steel in the connection plate. For this study, potential problems with flame cutting the connection plates where diagonals exist were ignored in order to see if the retrofit method would lower the stresses enough to be considered a feasible option.

Removal of Diagonal Bracing

To properly model removal of the cross frame members from the type E diaphragms, this was done at all locations on the bridge. This should greatly reduce the amount of stresses applied to the connection plates, thereby reducing secondary bending stresses within the web gaps. Although other retrofit methods were applied only locally, this was applied at all type E diaphragms because it may have a large impact on the structural integrity of the bridge. An additional consideration that must be investigated for this retrofit is therefore the increase in bending stress that results from the cross frame removal. An

additional retrofit possibility would be loosening the bolts on the diagonal members, but to model this would be no different than removing the members completely, thus was not considered separately.

5.3 Modeling the retrofits

To accurately capture the stress in the web gap, the global model for span 10 was remeshed at the web gap of one representative cross frame in the region of the connection plate to web connections. The cross frame selected is the same cross frame location that was instrumented during the live load diagnostic test of span 10. The model was remeshed in a way to ensure that adjacent elements still shared coincident nodes. By using minimally distorted quadrilateral elements, results will not be adversely affected by the refined mesh. The refined mesh was first created for the case of existing field conditions with no retrofits. An example of the finer mesh is shown in Figure 5.2.

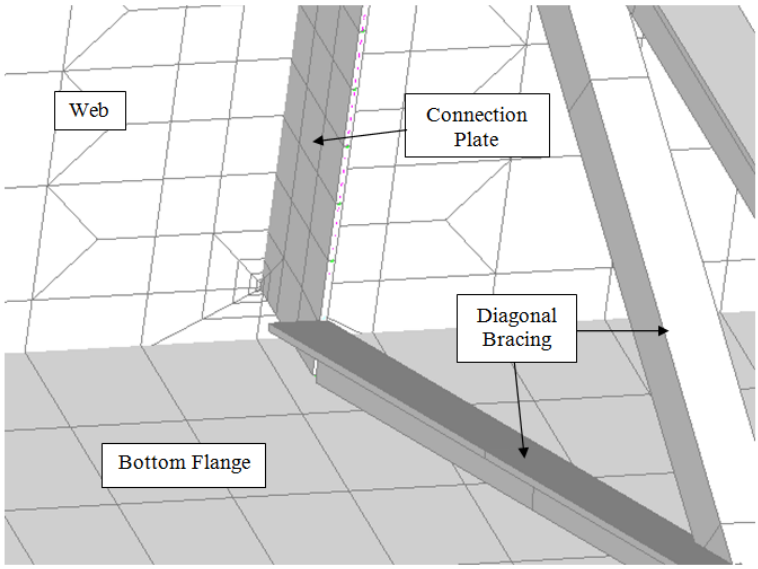

Figure 5.2 Remesh of Original Model on Web and Connection Plate

Modeling the Positive attachment

The refined mesh from the connection plates was also used to model the stem of the WT acting as the positive attachment between the connection plate and the flanges. This stem is offset from the connection plate and connected using rigid links. Since the meshes are the same size, it was possible to link the nodes of all the elements, thus creating a completely rigid connection. However, since the actual field connection would only be made using several bolts, the rigidity of which is questionable, several different methods were used to model the connection to replicate upper and lower bound stiffnesses of the connection. For the upper bound, links were placed at each node. To represent the use of 4 bolts, 4 links in each shear plane were used for the lower bound. Two intermediate models were also created, with varying number of nodal links. They will be described in detail in the results section.

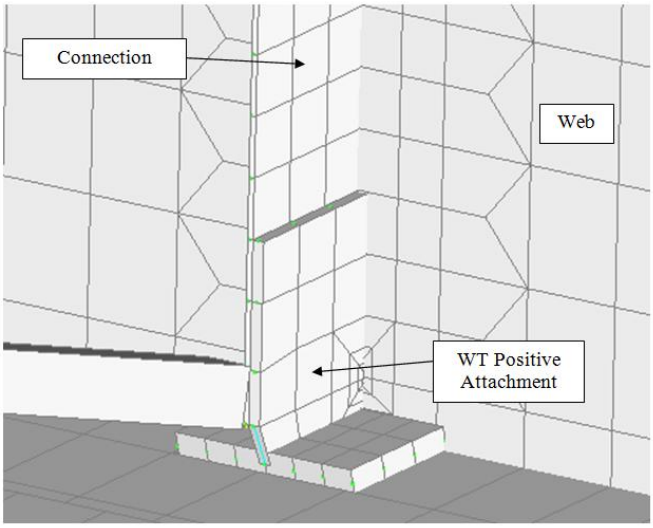

Figure 5.3 Model showing WT positive attachment at bottom flange

The WT flange was modeled in a similar manner, however because there was no remeshing of the girder flanges, the element size of the flanges was larger and constant. These were connected to the flanges using rigid links, again with an upper and lower bound for comparison. Figure 5.3 shows a model of the typical positive attachment of a WT to the bottom flange of a girder. The model for the top plate attachment is similar to that of the stem of the WT, except for the fact that it is connected directly to the top flange to represent the weld. Four rigid links were used in order to connect the plate to the top flange. The refined mesh was used to create plate elements where they are adjacent to the connection plate. An image of the typical modeled top flange tab connection is shown in Figure 5.4.

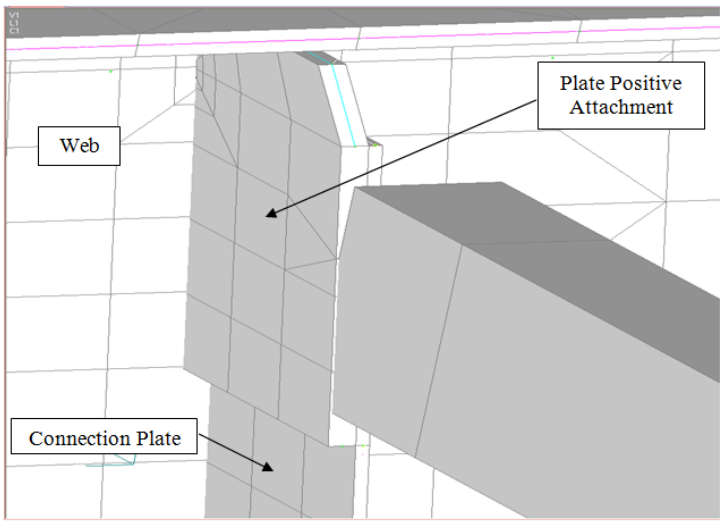

Figure 5.4 Model showing positive top flange connection

Modeling the Slot retrofit

To model the slot retrofit the elements at the location of the new connection plate to web weld terminus were remeshed. The same fine mesh used for the case of the existing conditions was again used for consistency in comparison later on. To model the cut, elements in the connection plate were decreased in size to be offset a distance of at least 1/4 in from the web. Because of the mesh used, the actual slot width of the model is .33 in. and the gap length is increased by 12.2 in. on the bottom of the connection plate and 11.7 in. on the top of the connection plate. The modeled slot retrofits are shown in Figure 5.5.

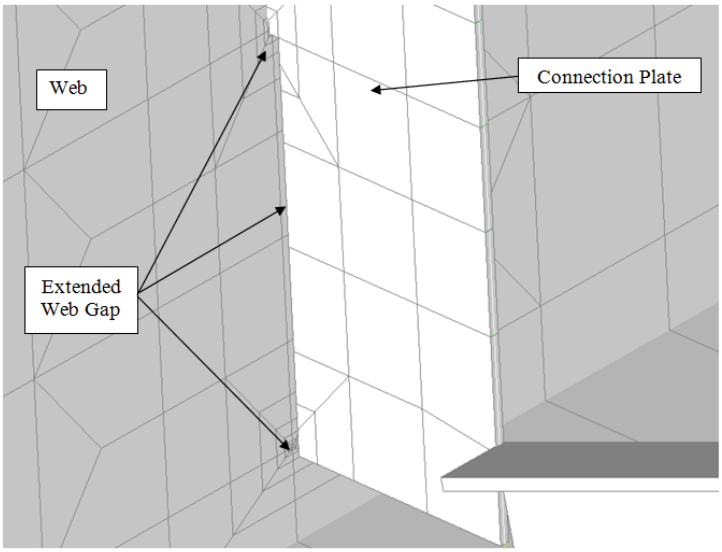

Figure 5.5 Model showing slot between web and connection plate

One item excluded from this model is the drilled hole at the web to connection plate weld, which serves as the initiation site for flame cutting of the connection plate. Burrs and other imperfections on the surface of the hole may lead to stress concentrations that would not be accounted for if the retrofit hole was modeled with a flawless cut. Leaving this out of the model is therefore conservative for determining stress concentrations at the web gap.

Modeling Removal of Diagonal Bracing

To model the removal of diagonal bracing, the diagonal elements of diaphragm type E were simply removed from the model. The mesh was again refined to allow for reading data close to the weld toe on the connection plate.

5.4 Results of the analysis

For each case modeled above, nodal loads representing the AASHTO fatigue truck were placed in the right lane of the bridge at the location that produced maximum stresses in the connection plates of interest. A rear axle spacing of 14 ft. was selected for the truck in order to create the largest stress possible in the connection plates.

In order to capture the stresses in the web gap near the weld tow, stresses in the connection plate were recorded. Stresses from the connection plate had to be used because the model was made using shell elements. Since the connection plates are oriented perpendicular to the web, the stresses transmitted through these elements should be the same as the stresses that are seen at the weld toe. The stress at the weld toe was determined using three different methods. Fisher measured gap stresses 0.12 in. from the weld toe in 2006 and Fisher's method from 1991 measured stresses 0.5 in from the weld toe. In addition to using stresses from existing elements, extrapolation methods have also been used to approximate stresses at the weld toe locations. To determine stresses in this manner, elements 3 and 4 were used to create a linear extrapolation and the stress where this intersected the vertical axis was used as the stress at the weld toe. The stress values extracted from these elements were used as the stress range in determining the remaining fatigue life of the bridge.

Original model (no retrofit)

Results of the remeshed model with no retrofits are presented in Table 5.1. The horizontal distance of the centroid of the element to the weld toe is shown in the left column, and stresses are reported at each web gap location. The sharp increases in stress as the elements get closer to the weld toe are apparent. The rows highlighted in gray are the elements used directly for fatigue life calculation. The 3rd and 4th rows are the elements used to extrapolate the stress at the weld toe for the third method of calculating fatigue life.

Table 5.1 Original Model Stresses for Refined Mesh

Distance to weld (in)	Stress (ksi) at Gap Location							
	A	B	C	D	E	F	G	H
0.046875	17.43	-33.45	-20.97	31.17	-17.28	31.52	22.18	-33.73
0.140625	12.08	-20.02	-14.52	18.80	-11.94	19.05	15.38	-20.16
0.28125	8.94	-12.33	-10.75	11.66	-8.83	11.84	11.40	-12.41
0.5625	6.04	-7.18	-7.26	6.86	-5.94	6.98	7.72	-7.22
1.125	3.72	-3.28	-4.47	3.18	-3.63	3.25	4.77	-3.29
2.25	2.22	-2.45	-2.66	2.39	-2.14	2.43	2.85	-2.48
4.5	1.37	-1.57	-1.64	1.53	-1.32	1.55	1.76	-1.59

Stresses for these elements and the extrapolated values that were used in fatigue calculations are shown in Table 5.2. Results for remaining fatigue life for the rest of the models will be saved for the end of the chapter, but are presented here to detail the method used in the procedure.

Table 5.2 Expected Fatigue Life for Original Model

	Label	Location/ Method	Distance from weld toe (in)	Fatigue Detail Location			
				A	B	C	D
Stress Range(ksi)	Method 1	Connor and Fisher (2006)	0.14	12.1	-20.0	-14.5	18.8

	Method 2	Fisher *et al.* (1987)	0.56	6.0	-7.2	-7.3	6.9
	Method 3	Hobbacher (2009)	Linear extrapolation	11.8	-17.5	-14.2	16.5
Fatigue Life (yrs)	Method 1	Connor and Fisher (2006)	0.14	6	1	3	2
	Method 2	Fisher *et al.* (1987)	0.56	47	28	27	32
	Method 3	Hobbacher (2009)	Linear extrapolation	6	2	4	2

Positive attachment

The first case to be reported is the use of WT sections at both the top and bottom ends of connection plates. To effectively connect the WT sections to both the connection plates and flanges, assumptions had to be made. The shell elements required using rigid links between nodes to make these connections. As mentioned before, both an upper and lower bound for the number of rigid links was modeled. The lower bound case (Case A) has 4 links in each shear plane, representing the 4 bolts per plane recommended by Fisher. The upper bound case (Case D) has links at each of the WT nodes, excluding the elements in the remeshed region. Two additional intermediate models used 6 links connecting the WT section to the flanges with a variable number of links on the top connection plate: Case B has 4 links and Case C has 6 links. For both of these cases, the bottom of the connection plate is connected to the WT with 4 links. Although each of these models differs slightly, they are all modeling the positive connection with WT's at both the top and bottom of each connection plate within cross frame 2. A summary of the resulting stresses at the elements of interest is presented in Table 5.3.

Table 5.3 Stress Results for Positive Attachment with WT's

Distance from weld toe (in)	**Fatigue Detail Location**							
	A	B	C	D	E	F	G	H
	Stress Range (ksi)							
Case A	**4 Links Per Plane**							
0.14	5.0	-6.2	-6.8	5.5	-4.6	5.5	7.4	-7.0
0.56	2.5	-2.3	-3.4	2.1	-2.3	2.2	3.7	-2.4
Extrapolation	4.9	-4.8	-6.7	4.3	-4.5	4.2	7.2	5.4
Case B	**4 Links on Connection Plate, 6 Links Per Flange**							
0.14	2.5	-4.3	-3.8	4.2	-2.4	4.2	4.3	-4.9
0.56	1.2	-1.8	-1.9	1.8	-1.2	1.8	2.2	-1.9
Extrapolation	2.4	-3.3	-3.7	3.3	-2.4	3.2	4.2	-3.8

Case C	6 Links on Connection Plate, 6 Links Per Flange							
0.14	1.3	-4.4	-2.4	4.3	-1.1	4.3	2.6	-5.0
0.56	0.6	-1.8	-1.1	1.8	-0.5	1.9	1.2	-2.0
Extrapolation	1.2	-3.3	-2.2	3.3	-1.1	3.3	2.5	-3.8
Case D	**Links at Every Node (Except Remesh)**							
0.14	1.0	-2.2	-1.8	2.1	-0.9	2.1	2.0	-2.6
0.56	0.4	-0.5	-0.7	0.5	-0.4	0.6	0.8	-0.6
Extrapolation	0.9	-1.8	-1.7	1.7	-0.8	1.7	1.8	-2.1

It can be seen that the better the connection the greater the reduction in stress at the web gap. Table 5.4 presents the percent reduction in stress for each of the cases of positive WT attachment relative to the original model. The reduction ranges from a low of 52% to a high of 94%; the actual reduction would most likely fall somewhere in between. The effectiveness of this connection will depend on the tightness of the WT to both the connection plate and flange members of the bridge. If this retrofit method is chosen, sufficient clamping force needs to be provided via the bolts to optimize its effectiveness.

Table 5.4 Percent Reduction in Stress Range for WT Positive Attachment

Distance from weld toe (in)	Fatigue Detail Location							
	A	B	C	D	E	F	G	H
	Reduction In Stress Range (%)							
Case A	**4 Links Per Plane**							
0.14	59	69	53	71	62	71	52	65
0.56	59	69	54	69	62	69	52	66
Extrapolation	59	73	53	74	62	75	52	69
Case B	**4 Links on Connection Plate, 6 Links Per Flange**							
0.14	79	78	73	77	80	78	72	76
0.56	80	75	74	74	80	74	72	73
Extrapolation	80	81	74	80	80	81	72	79
Case C	**6 Links on Connection Plate, 6 Links Per Flange**							
0.14	89	78	84	77	91	78	83	75
0.56	90	75	85	74	91	73	84	73
Extrapolation	90	81	84	80	91	80	84	78
Case D	**Links at Every Node (Except Remesh)**							
0.14	91	89	87	89	93	89	87	87
0.56	93	94	90	93	94	92	90	92
Extrapolation	92	90	88	90	93	90	88	88

These values confirm that the amount of connectivity between elements strongly influences the effectiveness of the retrofit. For the comparison of this type of retrofit to others, we will assume that the actual retrofit will act somewhere between the upper and lower bounds of connectivity. This assumption comes from the fact that although only the bolts will actually be connecting the members, the tightness will be sufficient to cause the members to interact in a near slip-critical manner.

Similar results are presented in Table 5.5 for the case where the WT section is on the bottom flange and a steel plate is used to provide positive attachment at the top. Upper and lower bond connectivity options were modeled once again.

Table 5.5 Stress Results for Positive Attachment with WT's at Bottom Flange and Plates at Top Flange

Distance from weld toe (in)	**Fatigue Detail Location**							
	A	B	C	D	E	F	G	H
	Stress Range (ksi)							
Case A	**4 Links Per Plane, Weld at Top**							
0.14	2.6	-6.5	-4.0	5.8	-2.6	5.7	4.7	-7.2
0.56	1.3	-2.3	-2.0	2.2	-1.3	2.2	2.4	-2.5
Extrapolation	2.6	-5.0	-3.9	4.6	-2.5	4.4	4.6	-5.6
Case B	**Links at Every Node (Except Remesh)**							
0.14	1.1	-2.1	2.0	2.0	-1.0	2.0	2.1	-2.5
0.56	0.5	-0.4	-0.9	0.5	-0.5	0.5	0.9	-0.5
Extrapolation	1.0	-1.7	-1.9	1.7	-1.0	1.7	1.9	-2.0

For the web gaps located near the bottom of connection plates, the stresses are very similar to those for the previous case. Web gap stresses at the top flange are actually lower than in the case of WT connections for the case with 4 links however. This is due to the modeling of the welded connection with 4 rigid links at the end of the plate. This allows for no rotation of the plate, and may therefore be under conservative for this case. This is not viewed as a significant view in the case of the WT connections because the flange is attached on either side of the plate and will likely be more resistant to such rotation. Table 5.6 shows the percentage of reduction in stress from the original model. The reduction ranges from a low of 66% to a high of 93%, very comparable to the previous case.

Table 5.6 Percent Reduction in Stress Range for WT's at Bottom Flange and Plates at Top Flange

Distance from weld toe (in)	**Fatigue Detail Location**							
	A	B	C	D	E	F	G	H
	Reduction In Stress Range (%)							
Case A	**4 Links Per Plane, Weld at Top**							
0.14	78	68	72	69	79	70	69	64
0.56	78	67	73	68	79	68	69	66
Extrapolation	78	71	73	72	79	74	70	68

Case B	Links at Every Node (Except Remesh)							
0.14	91	89	86	89	91	89	87	87
0.56	92	94	88	93	92	92	89	93
Extrapolation	91	90	87	90	92	90	87	88

Slot retrofit

The stresses for the slot retrofit were taken from elements on the remeshed connection plate in locations similar to where stress values were taken for the other methods. Horizontal distances from the weld toe are the same; however they are not located at the same height along the web. Table 5.7 provides a summary of the resulting stresses for this model and the relative stress decreases. The retrofit is shown to reduce the stress range in the connection by up to 79%.

Table 5.7 Slot Retrofit Stresses and Percent Reduction in Stress Range

Distance from weld toe (in)	Fatigue Detail Location							
	A	B	C	D	E	F	G	H
	Stress Range (ksi)							
0.14	4.0	-5.6	-3.8	5.4	-2.7	5.8	4.0	-6.2
0.56	2.3	-2.7	-2.4	2.7	-1.4	3.0	2.4	-2.9
Extrapolation	3.7	-4.5	-3.3	4.4	-2.5	4.7	3.7	-5.0
	Reduction In Stress Range (%)							
0.14	67	72	74	71	77	70	74	69
0.56	61	63	67	61	77	57	70	59
Extrapolation	69	74	77	73	79	72	76	72

Removal of cross frame members

The removal of diagonal elements from the cross frames resulted in the local stresses shown in Table 5.8. The percentages of reduction in stress from the original model are shown as well. It should be noted that the stresses in this case are opposite in sign when compared to those in the original model and the other retrofits. The retrofit is shown to decrease the stress range in the connection by up to 92%.

Table 5.8 Stress Results from Removal of Diagonal Element Retrofit

Distance from weld toe (in)	Fatigue Detail Location							
	A	B	C	D	E	F	G	H
	Stress Range (ksi)							
0.14	-5.0	2.4	3.4	-2.7	6.0	-2.3	-1.4	2.4
0.56	-2.3	0.8	1.5	-0.8	2.8	-0.6	-0.5	0.8

Extrapolation	-4.9	2.1	3.3	-2.3	5.9	-2.0	-1.3	2.2
	Reduction in Stress Range (%)							
0.14	59	88	77	86	50	88	91	88
0.56	62	89	79	89	52	92	94	89
Extrapolation	59	88	77	86	50	88	91	87

5.5 Estimated fatigue life of retrofitted designs

Each of the retrofit methods selected for analysis significantly reduced the stresses in the web gaps. The average decreases in stress for each modeled retrofit type are shown in Table 6 9. The upper bound for both of the positive attachment methods are the most effective retrofits for reducing the stress in the web gaps. As discussed before, these may be reducing the stress more than would actually occur in the field, particularly in the case of the plate connections to the top flange. However, we shall assume that the actual retrofit will act closer to the upper bound than the lower bound because tightness of the bolts will provide better member interaction than simply connecting 4 points.

The stresses found at each location were used for determining the fatigue life of the bridge. Several assumptions were made in adopting this procedure for the retrofits. The AASHTO category C detail was used in each case. This detail should remain the same for both the removal of diaphragm cross frames and the slot retrofits. However, the creation of positive attachment may result in a different fatigue category. The reason that the type C detail was also used in this case is that the stresses of importance are still within the web gap. Since the attachments are made to the connection plates and flanges, and not the web itself it is considered to act in a similar manner. The fatigue life for each retrofit type at all gap locations is presented in Table 6 10. The fatigue life is considered to be infinite if the stress range is below the limiting stress range for the detail, which for category C is 4.4 ksi. This is represented in the table by I.R.L., which stands for Infinite Remaining Life. The effectiveness of the retrofits is quite apparent for each case. The method proposed by Fisher et al. best models the bridge with its current cracking conditions. Using this method to measure stress 0.56 in. from the weld, all of the retrofits result in infinite life.

Table 5.9 Summary of Stress Range Reductions from retrofit designs

Retrofit Method		**Average % Stress Reduction**
Positive Attachment with WT	Case A	63
	Case B	77
	Case C	82
	Case D	90
Positive Attachment with WT at Bottom Flange and Plate at Top Flange	Case A	72
	Case B	90
Removal of Diagonals	-	79
12 in. Slot Retrofit	-	70

Table 5.10 Expected fatigue life for original model and retrofit

Distance from weld toe (in)	Fatigue Life (yrs) at Detail Location							
	A	B	C	D	E	F	G	H
Original Model								
0.14	6	1	3	2	6	1	3	1
0.56	47	28	27	32	49	30	22	27
Extrapolation	6	2	4	2	6	2	3	2
Positive Attachment with WT's, 4 Links Per Connection Plate and Flange								
0.14	83	44	33	62	106	63	26	30
0.56	I.R.L.	I.R.L.	I.R.L.	I.R.L.	I.R.L.	I.R.L.	I.R.L.	I.R.L.
Extrapolation	88	94	35	I.R.L.	113	I.R.L.	27	64
Positive Attachment with WT's, 4 Links on Connection Plate, 6 Per Flange								
0.14	I.R.L.	I.R.L.	I.R.L.	I.R.L.	I.R.L.	I.R.L.	I.R.L.	86
0.56	I.R.L.	I.R.L.	I.R.L.	I.R.L.	I.R.L.	I.R.L.	I.R.L.	I.R.L.
Extrapolation	I.R.L.	I.R.L.	I.R.L.	I.R.L.	I.R.L.	I.R.L.	I.R.L.	I.R.L.
Positive Attachment with WT's, 6 Links on Connection Plates and Flanges								
0.14	I.R.L.	I.R.L.	I.R.L.	I.R.L.	I.R.L.	I.R.L.	I.R.L.	83
0.56	I.R.L.	I.R.L.	I.R.L.	I.R.L.	I.R.L.	I.R.L.	I.R.L.	I.R.L.
Extrapolation	I.R.L.	I.R.L.	I.R.L.	I.R.L.	I.R.L.	I.R.L.	I.R.L.	I.R.L.
Positive Attachment with WT's, Links at every Node (Except Remesh)								
0.14	I.R.L.	I.R.L.	I.R.L.	I.R.L.	I.R.L.	I.R.L.	I.R.L.	I.R.L.
0.56	I.R.L.	I.R.L.	I.R.L.	I.R.L.	I.R.L.	I.R.L.	I.R.L.	I.R.L.
Extrapolation	I.R.L.	I.R.L.	I.R.L.	I.R.L.	I.R.L.	I.R.L.	I.R.L.	I.R.L.
4 Links Per Plane, Welded Tab at Top								
0.14	I.R.L.	38	I.R.L.	51	I.R.L.	56	98	27
0.56	I.R.L.	I.R.L.	I.R.L.	I.R.L.	I.R.L.	I.R.L.	I.R.L.	I.R.L.
Extrapolation	I.R.L.	81	I.R.L.	107	I.R.L.	120	107	57
WT Bottom, Tab Top - Links at Every Node (Except Remesh)								
0.14	I.R.L.	I.R.L.	I.R.L.	I.R.L.	I.R.L.	I.R.L.	I.R.L.	I.R.L.
0.56	I.R.L.	I.R.L.	I.R.L.	I.R.L.	I.R.L.	I.R.L.	I.R.L.	I.R.L.
Extrapolation	I.R.L.	I.R.L.	I.R.L.	I.R.L.	I.R.L.	I.R.L.	I.R.L.	I.R.L.
Diagonals Removed								
0.14	84	I.R.L.	I.R.L.	I.R.L.	48	I.R.L.	I.R.L.	I.R.L.
0.56	I.R.L.	I.R.L.	I.R.L.	I.R.L.	I.R.L.	I.R.L.	I.R.L.	I.R.L.
Extrapolation	89	I.R.L.	I.R.L.	I.R.L.	51	I.R.L.	I.R.L.	I.R.L.
12 in. Slot Retrofit								
0.14	I.R.L.	58	I.R.L.	66	I.R.L.	53	I.R.L.	43
0.56	I.R.L.	I.R.L.	I.R.L.	I.R.L.	I.R.L.	I.R.L.	I.R.L.	I.R.L.
Extrapolation	I.R.L.	110	I.R.L.	I.R.L.	I.R.L.	101	I.R.L.	82

6 Summary and Conclusions

A research project was undertaken to investigate the problem of fatigue cracking in the steel tub girders of the Rt. 141 Newport Viaduct, located in New Castle Co., Delaware. The 19 span viaduct was built in 1978 and carries a high level of traffic. The first internal inspection of the viaduct, conducted in 2005, discovered a large number of fatigue cracks in the web gap region where the diaphragm connection plate is welded to the girder web. The fatigue cracks were likely caused by distortion induced deformation of the region. The research project involved field testing (a controlled load test and in-service monitoring), numerical modeling (global finite element models of two sections, and local models of the connection region), fatigue evaluation, and the evaluation of several different retrofit options. The results of this multi-year investigation are summarized in detail in three master's thesis (Kusc, 2009; Quigley, 2009; Soto Fuentes 2011). The key conclusions from the investigation are the following:

1. Controlled load tests were conducted of spans 10 and 15. For each one, strain transducers were mounted to the flanges, web, and cross frame members at three different diaphragm locations. Strains were recorded as two 53 kip loaded trucks crossed the bridge. For span 10, the absolute maximum stress recorded was 1.87 ksi in the bottom flange; the absolute minimum stress recorded was -0.61 ksi in a cross frame member. For span 15, the absolute maximum stress recorded was 2.68 ksi in the bottom flange; the absolute minimum stress recorded was -0.75 ksi, also in the bottom flange.
2. In-service monitoring was conducted in span 10 to gather data due to the site-specific traffic for the fatigue evaluation. Eight strain gages/transducers were installed around the diaphragm and in the web gap region. The strains were recorded 24/7 for 23 days, and processed automatically using the Rainflow algorithm. The system ran continuously off of two large marine grade 12 volt batteries; the system was remotely accessible for 2 hours a day through a cellular modem. The largest number of cycles, and the cycles of highest magnitude, were experienced in the bottom web gap region and the web next to the connection plate at the bottom of the web.
3. Global, high-fidelity, finite element models were created of spans 9 to 11, and spans 12 to 16, of the viaduct. The global models represented the steel tub girders and the concrete composite deck in great detail, using primarily shell type elements. Beam elements were used to model the cross frame members, rigid links were used to connect the girder to the deck and the parapet to the deck, and appropriate boundary conditions were specified at the bearing locations. Results of the controlled load test were used to calibrate the models. A sensitivity study showed that moderate changes to the transverse position of the truck, concrete modulus, and connectivity of the parapet did not result in better agreement uniformly, therefore, no significant changes were made to the models. The agreement between the model and test results for the global member behavior were sufficiently accurate to use the models for the subsequent fatigue evaluation and retrofit study.

4. Local 3D finite element models of the connection were created, one for the top connection and for the bottom connection. The models were loaded through the bolt holes of the connection, as they would be in field. The results show a very localized, but high stress gradient in the web gap region where the fatigue cracks occurred, consistent with what was found in the field inspection. Analyses were conducted to study the effect of the boundary conditions on the connection stresses: the bottom connection region was found to be more sensitive to the choice of boundary conditions than the top connection. Furthermore, for the same loading, the bottom connection had higher stresses in the web gap than the top connection. This finding is also consistent with the inspection results that showed the majority of the cracks occurred in the bottom connection.
5. A fatigue evaluation was conducted using the global finite element models to see if the fatigue life was consistent with the observed cracking. The lifetime average daily truck traffic was calculated based on the ADT measured by DelDOT in 2007. The stress range at the weld toe was determined using three different methods as reported in the literature. Two of the methods predicted cracking would occur within a few years of the bridge opening, which does not seem plausible given other data obtained about the condition of the cracked regions. The third method predicted cracking would have occurred within a time frame that is consistent with the observed behavior. Regardless of the method, all resulted in life evaluations that predicted cracking would occur.
6. The fatigue evaluation was also conducted using the results of the in-service monitoring. This required calculating the effective stress at the weld toe. This was done by calculating the effective stress in the web gap region where the strain gage was located, and transferring this to the weld toe using the results of the local finite element model. The lifetime average daily truck traffic was determined using the histograms from the rainflow data. Based on this analysis the connections were found to have a mean fatigue life of between 10 and 16 years, which is quite consistent with the observed behavior.
7. The global finite element model of span 10 was used to investigate several different retrofit options for the repair of the connections. Three different options were considered: provide positive attachment of the connection plate to the flange; create a slot between the connection plate and the web; and remove the diagonal bracing. All of the methods resulted in a decrease in the stress at the connection, with the reduction ranging from 60 to 90% from the original design. In this case, all of the options would appear to be acceptable. A final decision would, however, also depend on the constructability of the repair and the impact on the other design criteria for the bridge.

7 References

AASHTO. (1990). Guide Specifications for Fatigue Evaluation of Existing Steel Bridges American Association of State Highway and Transportation Officials, Washington D.C.

ABAQUS. (2008). ABAQUS Analysis User's Manual, Pawtucket, R.I.

AECOM. (2007). "2006 Initial Interior Box Inspection Report." Horsham, Pa.

Alampalli, S. and Lund R. (2006). "Estimating Fatigue Life of Bridge Components Using Measured Strains." Journal of Bridge Engineering, 11(6), 725-736.

Berglund, Evan M., and Arturo E. Schultz. (2006). "Girder Differential Deflection and Distortion-Induced Fatigue in Skewed Steel Bridges." Journal of Bridge Engineering Mar. / Apr., 169-177.

Bridge Diagnostics Inc. (2006). Strain Transducer For Structural Testing. 15 Jan. 2009. < http://www.bridgetest.com/products/strain_transducers.html>

Connor, Robert, and John W. Fisher. (2006). "Identifying Effective and Ineffective Retrofits for Distortion Fatigue Cracking in Steel Bridges Using Field Instrumentation." Journal of Bridge Engineering Nov. / Dec., 745-752.

DelDOT. (2007). "DelDOT's Priority Bridges" 3 Feb. 2009.http://www.transportation1.org/BridgeReport/docs/DelDOT%20Priority%20Bridges.pdf

DelDOT. (1974). Structural Drawings for Newport Viaduct, Bridge 1-501. Prepared by Gannet Fleming Corddry & Carpenter Inc.

Fisher, John W. and Peter Keating. (1989) "Distortion-Induced Fatigue Cracking of Bridge Details with Web Gaps." Journal of Constructional Steel Research 12, 215-228.

Fisher, John W., Dennis R. Mertz., and Kuang-Chong Wu. (1982). "Displacement-Induced Fatigue Cracking of a Box Girder Bridge." IABSE Reports, 71-76.

Fisher, J. W., Yen, B. T., and Wagner, D. C. (1987). “Review of field measurements for distortion-induced fatigue cracking in steel bridges.” Transportation Research Record, 1118, 49-55.

Fisher, John W., et al. (1990). “Distortion-Induced Fatigue Cracking in Steel Bridges.” National Cooperative Highway Research Program Report 336 Transportation Research Board, Washington D.C. Dec

Google Maps. (2009). 3 Apr. < http://maps.google.com>

Hobbacher, A.F. (2009) “The New IIW Recommendations for Fatigue Assessment of Welded Joints and Components – A Comprehensive Code Recently Updated.” International Journal of Fatigue 31. 50-59.

Jajich, D., and A. E. Schultz. (2003). “Measurement and Analysis of Distortion- Induced Fatigue in Multigirder Steel Bridges.” Journal of Bridge Engineering Mar. /Apr., 84-91.

Kaufmann, E. J. (2008). “Newport Viaduct Core Sample Examination-Girder Web Connection Plate Cracking.” Center for Advanced Technology for Large Structural Systems, Lehigh Univ., Bethlehem, Pa. 2 June.

Khalil, Ayman, et al. (1998). “Retrofit Solution for Out-of-Plane Distortion of X-Type Diaphragm Bridges.” Transportation Conference Proceedings, 99-102.

Kim, Kyungsik, and Chai Yoo. (2006). “Interaction of Top Lateral and Internal Bracing Systems in Tub Girders.” Journal of Structural Engineering Oct., 1611-1620.

Kucz, Daniel. (2009). Analysis of Fatigue-Induced Distortion. Master Thesis, University of Delaware, Spring.

Manual for condition evaluation and Load and Resistance Factor Rating (LRFR) of Highway Bridges (2003), American Association of State Highway and Transportation Officials, Washington, D.C.

Naaman, Antoine E. (2004). Prestressed Concrete Analysis and Design: Fundamentals.2nd ed. Ann Arbor, Michigan: Techno Press 3000.

Quigley, James R. (2007) “Analysis of distortion-induced fatigue cracking of a trapezoidal steel box girder bridge including retrofit investigation,” Master Thesis, University of Delaware, Spring 2009

Roddis, W.M. Kim, and Yuan Zhao. (2003). “Finite-Element Analysis of Steel Bridge Distortion-Induced Fatigue.” Journal of Bridge Engineering Sept. /Oct., 259-266.

Soto Fuentes, Jose (2011) “Fatigue life analysis of a steel trapezoidal box girder bridge using measured strains,” Master Thesis, University of Delaware, Spring 2011

Stallings, J.M., et al. (1999). “Removal of Diaphragms from Three-Span Steel Girder Bridge.” Journal of Bridge Engineering Feb., 63-70.

Yip, A. S. M., and Cheng, J. J. R. (2000). “Shear lag in bolted cold-formed steel angles in tension.” Structural Engineering Report 233, Department of Civil and Environmental Engineering, University of Alberta.

Zhao, Yuan, and W.M. Kim Roddis. (2007). “Fatigue Behavior and Retrofit Investigation of Distortion-Induced Web Gap Cracking.” Journal of Bridge Engineering Nov. /Dec., 737-745.

Zhou, Y. Edward. (2006). “Assessment of Bridge Remaining Fatigue Life through Field Strain Measurement.” Journal of Bridge Engineering Nov. /Dec., 737- 744.

Zhu, H.T., et al. (2009). “The Shear Lag Effects on Welded Steel Single Angle Tension Members” Journal of Constructional Steel Research 65-1, 1171-1186.

Delaware Center for Transportation University of Delaware Newark, Delaware 19716

AN EQUAL OPPORTUNITY/AFFIRMATIVE ACTION EMPLOYER

To the extent permitted by applicable State and Federal laws, the University of Delaware is committed to assuring equal opportunity to all persons and does not discriminate on the basis of race, creed, color, sex, age, religion, national origin, veteran or handicapped status, or gender identity and expression, or sexual orientation in its educational programs, activities, admissions, or employment practices as required by Title IX of the Educational Amendments of 1972, Section 504 of the Rehabilitation Act of 1973, Title VII of the Civil Rights Act of 1964, and other applicable statutes. The University of Delaware has designated Karen Mancini, Director of the Office of Disabilities Support Services, as its ADA/Section 504 Coordinator under Federal law. Inquiries concerning Americans with Disabilities Act compliance, Section 504 compliance, campus accessibility, and related issues should be referred to Karen Mancini (302-831-4643) in the Office of Disabilities Support Services. Inquiries concerning Title VII and Title IX compliance and related issues should be referred to the Director of the Office of Equity and Inclusion, Becki Fogerty (302-831-8063).